



TECHNISCHE UNIVERSITÄT
CHEMNITZ

Magnetic Micromotors in Assisted Reproductive Technology

Von der Fakultät für Naturwissenschaften der
Technischen Universität Chemnitz

genehmigte

Dissertation

zur Erlangung des akademischen Grades

doctor rerum naturalium

(Dr. rer. nat.)

vorgelegt

von M.Sc. Lukas Schwarz

geboren am 08.06.1988 in Regensburg

Tag der Einreichung: 19.09.2019

Gutachter:

Prof. Dr. Oliver G. Schmidt

PD Dr. Benjamin Friedrich

Tag der Verteidigung: 22.06.2020

<https://nbn-resolving.org/urn:nbn:de:bsz:ch1-qucosa2-715579>

Bibliographic Information

Schwarz, Lukas

Magnetic Micromotors in Assisted Reproductive Technology

Dissertation at the Faculty of Natural Sciences at the Chemnitz University of Technology, Dissertation (English), 2020

116 pages, 25 figures and 11 tables, 203 references

Abstract

Micromotors – untethered, motile, microscopic devices – are implemented in this dissertation for two applications in the field of assisted reproductive technology. First, as synthetic motor units for individual sperm cells, representing a novel approach to counteract sperm immotility (asthenozoospermia), which is one of the most prevalent causes of male infertility. Second, as synthetic carriers of fertilized oocytes (zygotes) towards the realization of non-invasive intrafallopian transfer, representing a novel alternative to the current keyhole surgery (laparoscopy) approach to achieve early embryo transfer after in vitro fertilization. In both applications, magnetically actuated micromotors are utilized to capture, transport, and deliver individual cells in a reproducible, controllable manner. In comparison to established in vitro fertilization routines, the crucial advantage of using micromotors for the manipulation of gametes, i.e. sperm and (fertilized) oocytes, lies in the potential transfer of decisive steps of the fertilization process back to its natural environment – the fallopian tube of the female patient – taking advantage of the untethered, non-invasive motion and manipulation capabilities of magnetic micromotors. When sperm motility can be restored with magnetic micromotors, sperm can travel to the oocyte under external actuation and control, and an explantation of the oocyte for in vitro fertilization is not required. However, if in vitro fertilization was necessary, fertilized oocytes can be transferred back to the fallopian tube by micromotors in a non-invasive manner, to undergo early embryo development in the natural environment. These novel concepts of micromotor-assisted reproduction are presented and investigated in this thesis, and their potential is analyzed on the basis of proof-of-concept experiments.

Keywords: micromotor, microswimmer, microrobot, rotating magnetic field, in vitro fertilization, assisted reproductive technology, asthenozoospermia, zygote intrafallopian transfer, direct laser writing, 3D laser lithography

Table of Contents

1	Introduction.....	6
1.1	Background and Motivation.....	6
1.2	Objectives and Structure of this Dissertation	9
2	Fundamentals.....	11
2.1	Micromotors Definition and Concept.....	11
2.2	Micromotors for Biomedical Applications	13
2.3	Magnetic Micropropellers.....	15
2.3.1	Theory	15
2.3.2	Implementation.....	20
2.4	Microfabrication: Direct Laser Writing.....	21
2.5	Assisted Reproductive Technology	23
2.5.1	In vitro Fertilization and Intracytoplasmic Sperm Injection	24
2.5.2	Embryo Transfer and Zygote Intrafallopian Transfer.....	25
2.5.3	The Sperm Cell and the Oocyte	26
2.6	Towards Micromotor-Assisted Reproduction	28
3	Materials and Methods.....	30
3.1	Fabrication of Microfluidic Channel Platforms.....	30
3.1.1	Tailored Parafilm Channels	30
3.1.2	Polymer Channels Cast from Micromolds	31
3.1.3	Tubular Channels to Mimic In vivo Ducts.....	32
3.2	Fabrication of Magnetic Micropropellers.....	32
3.2.1	Direct Laser Writing of Polymeric Resin	33
3.2.1.1	Design and Programming	33
3.2.1.2	Exposure and Development	35
3.2.1.3	In Situ Direct Laser Writing.....	35
3.2.2	Critical Point Drying.....	35
3.2.3	Magnetic Metal Coatings	36
3.2.4	Surface Functionalization	37
3.3	Sample Characterization.....	38
3.3.1	Optical Microscopy.....	38
3.3.2	Scanning Electron Microscopy	38
3.4	Cell Culture and Analysis	39
3.4.1	Sperm Cells	39
3.4.2	Oocytes.....	39
3.4.3	In vitro Fertilization.....	41

3.4.4	Hypoosmotic Swelling Test.....	44
3.4.5	Cell Viability Assays.....	44
3.5	Magnetic Actuation	45
3.5.1	Modified Helmholtz Coil Setup	46
3.5.2	MiniMag Setup	47
3.5.3	Experimental Procedure.....	48
3.5.3.1	Micromotor Performance Evaluation.....	48
3.5.3.2	Cell Transport Experiments.....	49
3.5.3.3	Cell Transfer Experiments	50
4	Micromotor-assisted Sperm Delivery	51
4.1	Micromotor Design and Fabrication.....	51
4.2	Actuation and Propulsion Performance	53
4.3	Capture, Transport, and Release of Sperm.....	56
4.4	Delivery to the Oocyte.....	59
4.5	Sperm Viability and the Ability to Fertilize	61
5	Micromotor-assisted Zygote Transfer.....	68
5.1	Micromotor Design and Fabrication.....	68
5.2	Actuation and Propulsion Performance	70
5.3	Capture, Transport, and Release of Zygotes	76
5.4	Transfer between Separate Environments.....	80
5.5	Zygote Viability and Further Development	82
6	Conclusions and Prospects	85
	Appendix.....	87
	Bibliography.....	93
	List of Figures and Tables.....	108
	List of Abbreviations and Terms.....	109
	Theses.....	111
	Selbstständigkeitserklärung	112
	Acknowledgments.....	113
	List of Publications	115
	Curriculum Vitae.....	116

1 Introduction

Reproduction stands out as one of the essential qualities of life. For us as investigators, yet also in the role of participants, reproduction can turn from comfortably easy to devastatingly difficult, e.g. in the case of pathological infertility. The fusion of oocyte and sperm is a tangible example of how our lives are based on and governed by microscopic processes, and now that we transitioned from passive observers to active creators of materials and machinery on the microscale, we aim to take control or at least assist those microscopic processes in our bodies as well, if need be. Synthetic micromotors can serve as handles on cells for more direct approaches to biomedical engineering on the microscale. This concept is set forth and demonstrated in this thesis regarding assisted reproductive technology (ART), assisting the very first steps of new life.

1.1 Background and Motivation

The two fields that are brought together in this work, i.e. ART and micromotors, must be explained in detail to clarify their proposed synergy, which will be carried out in the Fundamentals section. First of all, the application of assisted reproduction, i.e. to remedy infertility, constitutes the main motivation of this work, and micromotors serve as the technological means to achieve this medicinal goal. Second, the implementation of micromotors as microscopic agents to carry out a medical task, manipulating cells outside and inside of the patient's body for therapeutic purposes, is a paradigm of modern medicine under constant development in the 21st century, and this dissertation aims to contribute to this scientific progress with experimental validations of technical designs and approaches – here tailored specifically for the treatment of infertility – addressing key challenges also relevant for other applications in the field of biomedical micromotors. The intended application of micromotors in ART follows an ever-increasing demand in modern societies, as can be concluded from in vitro fertilization (IVF) statistics of prominent industrial countries that report greater total numbers of infertility treatments every year [1]–[3]. In total, approximately 105,000 treatment cycles have been reported in Germany in 2017 [1], 70,000 in the United Kingdom in the same year [2], and 260,000 in the United States in 2016 [3], which is overall a more than tenfold increase in the last 25 years and still almost 50 % more compared to ten years ago in these countries. Whereas the reasons for this trend are supposedly numerous and complex, and therefore discussed vividly in the field [4]–[8],

the demand for improvement and further development of current infertility treatments is quite apparent, considering unsatisfactory success rates and limitations of current technologies such as IVF [1]–[3], which will be discussed. Considering IVF and related *in vitro* treatments in particular, statistics indicate that their weakness lies not in the process of fertilization itself, i.e. the fusion of sperm and oocyte, but in the necessity of explantation and reimplantation of the female gamete (germ cell) before and after IVF, respectively [1]–[3]. This is where micromotors can take action. Micromotors, in the context of biomedical engineering, are devices that can move and carry out tasks at the microscale, ideally in an untethered, externally controlled and supervised manner. They can be applied *in vivo* by injection into the patient's body and move there freely through body fluids to the site of interest to execute their task under external control. A prominent application of this concept in current research is the employment of micromotors as motile drug carriers that can deliver therapeutic substances to a specific target site in the body, i.e. targeted drug delivery, for example to treat tumors with much reduced side effects owing to the highly localized spreading of the drug, as compared with conventional chemotherapy [9]–[11]. In infertility treatment, another case of localized delivery is in the focus, namely the delivery of the sperm cell to the oocyte for cell fusion. Infertility in general can have various pathological causes, both male- and female-related. Concerning male factor infertility, i.e. irregularities of the semen and sperm, the remedy of choice are often *in vitro* treatments such as IVF, necessitating oocyte extraction and embryo reimplantation, both uncomfortable and compromising procedures [1]–[3]. Here, instead of taking the oocyte out of its natural environment for IVF, micromotors offer a means to only support the sperm in question, for example by guiding them to the oocyte in case of impaired sperm motility, while the entire process of fertilization can still happen inside the body under natural conditions. This concept of micromotor-assisted fertilization was pioneered in 2012/13 by co-workers at the Institute for Integrative Nanosciences in Dresden [12], [13] and further developed in the present work. Specifically, the transportation and delivery of completely immotile sperm cells, patented by O. G. Schmidt (the doctorate supervisor) in 2014 [14], was achieved in proof-of-concept experiments, published by Medina-Sánchez and Schwarz et al. in 2015/16 [15], laying the groundwork for the present dissertation. The micromanipulation and assistance of individual cells for applications in ART is the principal subject of this thesis and is motivated by the possibility to transfer such micromotor-based approaches to the *in vivo* environment, which is in turn expected to improve success rates and feasibility of assisted reproduction to remedy severe cases of infertility such as complete sperm immotility [1], [15], [16]. Analogous to sperm cells, also female gametes can be transported by micromotors with accordingly adjusted geometry. This is relevant at a later stage of the fertilization

process, when the oocyte was successfully fertilized by the sperm. When conventional IVF has been conducted, it is necessary to incubate the fertilized oocyte, termed zygote, allowing it to undergo further cell divisions and develop into an embryo which can be reimplanted into the uterus. As indicated above, this step of embryo transfer (ET) is one of the critical points of IVF, as currently only approximately one in three ETs turn out to be successful [1]–[3]. Zygote intrafallopian transfer (ZIFT) is an alternative transfer technology where the fertilized oocyte is reimplanted back into the fallopian tube instead of the uterus, when it is still at an earlier stage of embryo development. However, this technique requires an invasive surgical procedure, which will be discussed in the Fundamentals section. Whereas micromotor-assisted sperm delivery could obviate ET or ZIFT altogether in cases where it could be applied *in vivo* instead of conventional IVF to deal with sperm defects such as immotility, micromotor-assisted zygote delivery could be applied as alternative to conventional ZIFT to reimplant zygotes that were fertilized by IVF to the fallopian tube in a non-invasive manner (Fig. 1).

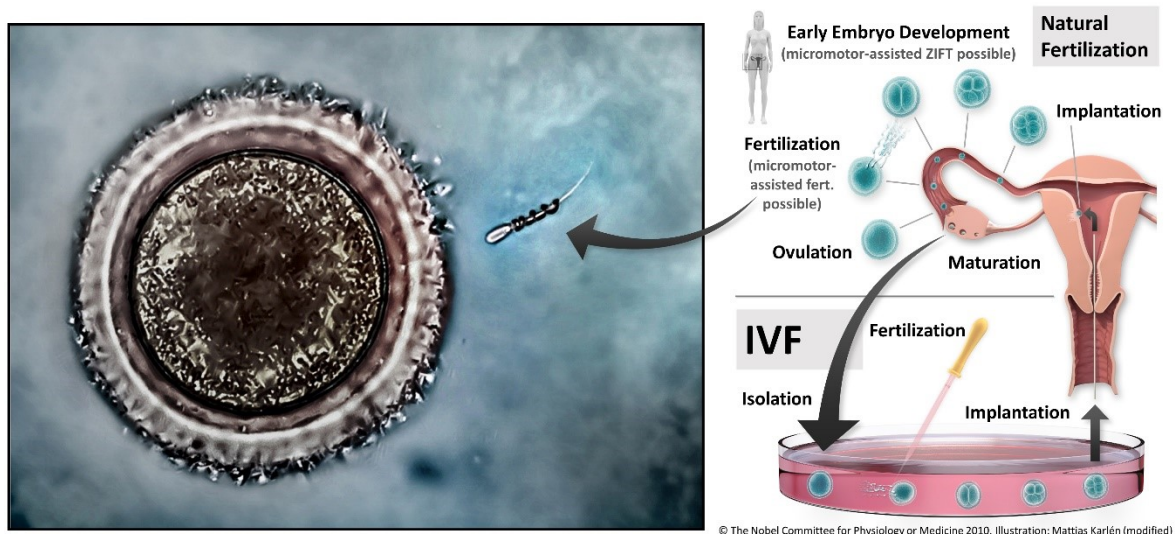


Figure 1: The concept of micromotor-assisted fertilization: Assistance of specific steps of the fertilization process to counteract infertility, for example the untethered delivery of an immotile sperm cell (left, reprinted with permission from [15]. Copyright © 2015 American Chemical Society), or non-invasive zygote intrafallopian transfer by micromotors – both with the aim to transfer current *in vitro* treatments back to the natural environment, i.e. the fallopian tube (right, modified from [17], used with permission).

In both cases, the capability of micromotors to operate *in vivo* in an untethered, externally controlled and supervised manner to carry out the task of respective cell transport and delivery is key to a significant advantage over conventional ART concepts: Keeping the natural environment of the respective cellular process (sperm-

oocyte fusion in the first case and zygote/embryo development in the second) as intact and untouched as possible while only punctually manipulating and assisting involved cells with a non-invasive, microsurgical intervention. First, however, it is necessary to conceive suitable micromotor designs and setups in both cases that can accomplish the described tasks in proof-of-concept experiments and fulfill critical requirements that allow the systems to be transferred to the *in vivo* environment to realize the full potential of this novel concept of micromotor-assisted reproduction. The concrete steps towards this goal that are described and addressed in this dissertation are outlined in the following section that will close the Introduction.

1.2 Objectives and Structure of this Dissertation

Building up on the new paradigm of micromotor-assisted fertilization that was outlined in the previous section, this dissertation aims to demonstrate potential applicability considering two specific problems of ART, namely assisted fertilization in the pathological case of complete immotility of sperm cells, and a non-invasive alternative to ZIFT. Both applications are based on the concept of using micromotors as transporters for individual cells, sperm and zygote respectively, to deliver them to the desired target site in the fallopian tube of the female patient. Within the scope of this work, clinical *in vivo* application of these concepts remained out of reach, although important steps towards this goal were taken with the experiments presented in this thesis. Beginning with the project of micromotor-assisted delivery of immotile sperm cells, the first objective was to design and fabricate a micromotor that can be externally actuated to capture and transport a sperm cell under the microscope in an untethered manner, based on its own motility. Second, the controlled movement and navigation of the proposed micromotor had to be verified and evaluated in physiological medium with sperm cells. The capture, transport, and delivery of an individual sperm cell to an oocyte in a microfluidic channel and the release of the captured sperm cell after successful delivery were the main objectives of this project. Moreover, the principal transferability of the *in vitro* experiment to a potential *in vivo* treatment had to be assessed, considering obstacles that the micromotor would have to face on its way to and through the fallopian tube, yet also considering the biocompatibility of the entire approach, i.e. precluding potentially harmful effects of the micromotor or external power supply on the function and viability of the sperm cells, the oocyte, and the entire *in vivo* environment. The same steps had to be undertaken for the second project, i.e. design, fabrication, evaluation and application of micromotors to transport and deliver fertilized oocytes in a microfluidic setup that served to simulate the challenge of having

to transfer the cells to a live fallopian tube in the perspective *in vivo* case of micromotor-assisted ZIFT. Consequently, the main part of this dissertation is comprised of two parts (sections 4 and 5) that are structured analogically to provide results and discussions of the formulated objectives considering the sperm and zygote transport projects, respectively. These sections are preceded by a Materials and Methods section where the setups and experiments for both projects are described in detail, and a Fundamentals section before that, which serves several purposes: At first, the reasons for the choice of design, fabrication, and actuation technique of the proposed micromotors are explained with reference to the general function and state-of-the-art of micromotors (section 2.1), especially considering biomedical applications (section 2.2). Subsequently, the function principle and characteristic physics of the chosen micromotor setup are explained and discussed (section 2.3), as well as those of the employed microfabrication technology (section 2.4). Then, the application field of ART is discussed in detail regarding current infertility treatments, their limitations, and the role and qualities of the involved gametes, i.e. sperm and oocyte (section 2.5). These different aspects are connected in a final part (section 2.6) to clarify the key challenges considering the application of micromotors in ART and how they are addressed in this work, i.e. how gametes can be supported by micromotors in the laboratory, and what is required to successfully transfer this approach to the *in vivo* environment. Ultimately, after the already mentioned two-part main body with results and discussions, conclusions are drawn considering the two projects and their future prospects in particular, and the application of micromotors in ART in general, with a focus on remaining challenges that also apply to micromotors for other biomedical applications. The closing sections of the dissertation – primarily of bibliographical nature – are listed in the Table of Contents above (not numbered). Most importantly, the "Theses" section comprises a list of theses, i.e. the essence and summary of this scientific work.

2 Fundamentals

This section serves to review the field of micromotors, from general concepts to biomedical applications, followed by a special focus on magnetic actuation and microfabrication. Ultimately, the field of ART is discussed and the proposed applications of micromotors in this field are placed in context.

2.1 Micromotors Definition and Concept

Micromotors are devices that can move and perform actions at the microscale. More specifically, the term is used for synthetic microstructures that operate in an untethered manner in a liquid medium, receiving energy either from their immediate surroundings, e.g. from chemicals, or from an externally applied source, e.g. electromagnetic fields, light or sound waves. Depending on the degree of autonomy or programmed external control, and integrated sensing capabilities, also the term "microrobot" is used. In that sense, motile microorganisms such as sperm cells or flagellated bacteria such as *Escherichia coli* (*E.coli*) can be considered as completely natural microrobots, as they are autonomous and even feature an on-board power source, unlike most synthetic micromotors. They can also probe their surroundings and move accordingly, pursuing their goal of finding food or purpose. Such microbes and flagellated cells also serve to illustrate the size scale of micromotors – larger than motor proteins and viruses at the sub-cellular level, and molecular machines such as the "Nanocar" [18], [19] as their synthetic counterparts, yet smaller than microscopic animals such as fleas and mites, or synthetic micro-electro-mechanical systems (MEMS) that can also have extremely small individual components but typically work as larger units, as tethered part of an on-chip network [20], as illustrated in Fig. 2.1. Free swimming at the microscale – just as natural microswimmers such as flagellated microbes and cells – was the first challenge that synthetic micromotors had to tackle to become useful untethered micromanipulation platforms. More than 40 years ago, E. M. Purcell explained in a now famous lecture the difficulties of moving at the microscale, the fundamental physics behind it and how this calls for new concepts of motion that differ from those we know from our everyday macroscale experience [21]. Accordingly, also the swimming strategy of sperm cells and bacteria is quite different from large marine animals and consequently has been serving as a valuable inspiration for the realization of synthetic microswimmers [22]–[24]. Moreover, these and other microorganisms have been employed themselves as biological motor units to propel

synthetic components in a so-called biohybrid micromotor approach [25]–[27]. Reviewing this and other, purely synthetic, concepts of microscale propulsion which are being realized in numerous forms since the beginning of the 21st century, micromotors can be generally classified as either biohybrid, chemical, or physical, according to their source of energy for propulsion [28]. This classification also implies different levels of external control and different requirements of the surrounding environment, i.e. the liquid medium: Biohybrid micromotors feature an on-board biological motor unit, i.e. a motile microorganism that has to stay alive in order to function [25]–[27]. Chemical micromotors are driven by catalytic reactions and are therefore depending on a suitable fuel that must be present in the surroundings [29]–[31]. Physical micromotors are typically passive and can only move when actuated by an externally applied stimulus, e.g. a magnetic field [32], [33], electric field [34], [35], temperature [36], [37], light [38], [39], or ultrasound [40], [41]. Combinations of chemical and physical stimuli, e.g. employing photocatalytic reactions [42], or deploying two different actuation modes [43], [44], are also possible.

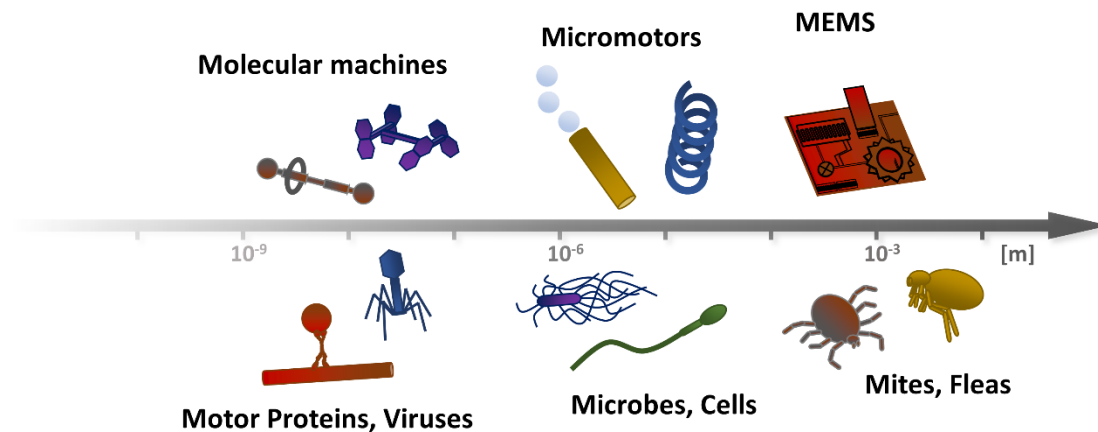


Figure 2.1: The size of micromotors: At eye level with microbes and cells, larger than molecular machines and proteins, smaller than most MEMS and the smallest insects.

Considering these differences, the choice of micromotor for a desired application depends primarily on the properties of the environment where the task is supposed to be performed, its accessibility and controllability. For example, many chemical micromotors are not suited for biomedical applications as they rely on fuels such as hydrogen peroxide that are not biocompatible. However, they can be applied in environmental applications as microscavengers, for example in water remediation [45]–[47]. For on-chip sorting, assembly, and microfabrication techniques, physical stimuli such as externally applied magnetic [48], [49] or electric [50] fields that actuate micromotors are suitable because of their reliable, predictable, and programmable

behavior [51], as these stimuli are also commonly applied in macroscale robotics [52]. For biomedical applications inside the human body, biohybrid micromotors that employ motile microbes as motor units can be a reasonable choice, as many microorganisms are naturally adapted to swim in the complex surroundings of body fluids [53], [54]. Nonetheless, microbes such as *E.coli* cannot be considered harmless for the body as many of them are actual pathogens (although it is possible to attenuate this by genetic engineering) [55], and their behavior and lifetime is hard to control in the *in vivo* case. In general, for the *in vivo* operation of micromotors for biomedical applications, several requirements must be met that will be discussed in the following section.

2.2 Micromotors for Biomedical Applications

The most prominent and best-researched potential application of micromotors in medicine is as microcarriers for drug delivery, also called drug targeting or targeted therapy [9]–[11]. Here, the advantage of microscopic agents that can operate in an extremely localized but complex environment under external control is apparent, as doses of delivered therapeutics can be controlled and potential side-effects can be limited, for example by targeting an individual spheroid of cancer cells instead of injecting an unspecific chemotherapeutic into the entire blood circulation. In principle, the same motivation applies to other proposed biomedical applications of micromotors such as biosensing for diagnosis and monitoring [56], [57], microsurgery [58], [59], or gene transfection [60], [61] and stem cell delivery [62], [63]. However, there are also major challenges that prevented the establishment of micromotors in clinical practice as of yet. The principal requirements for the successful *in vivo* operation of a micromotor are untethered, controllable motion and function in complex, three-dimensional (3D) microscale environments, biocompatibility, and supervision, i.e. feedback from the micromotor inside the body to the human operator outside. Promising demonstrations of the feasibility and controllability of tasks at the microscale, for example the untethered transport and delivery of microscopic cargo in microfluidic environments, can be found in the literature, presenting various micromotor systems [50], [53], [64]. However, these studies remain primarily limited to very specific *in vitro* environments, and only few studies on the actual *in vivo* applicability of certain concepts have been reported with animal testing [62], [65]–[67]. Frequently, the transfer of *in vitro* experiments to *in vivo* applications is challenged by the increased complexity of body fluids and vessels as compared with microfluidic laboratory setups. For example, many body fluids are highly viscous, exhibit non-

Newtonian behavior, and flow through complex, narrow and branched vessels with sticky walls [68], [69]. Moreover, the body usually takes measures to defend against microscopic intruders to avoid harm, which should be avoided – the provocation of immune responses as well as actual cell toxicity and tissue damage, of course. This is usually considered by using biocompatible, i.e. non-toxic, materials or coatings whenever possible. Another strategy is to cloak micro- or nanodevices with actual cell membranes or cell-mimicking coatings to hide them from the immune system [70]–[72]. However, the results of *in vitro* biocompatibility tests, e.g. co-incubation with relevant cells, are not always conclusive and sufficient to rule out negative effects. As mentioned in the previous section, the proper choice of microrobotic systems that rely on biocompatible actuation mechanisms is also crucial. In the present work, a magnetic field is used as an external actuator for the proposed micromotors because of its good controllability and established biocompatibility [73]–[75]. Specifically, a rotating magnetic field (RMF) is preferred over gradient fields because of the comparatively long-range effect at relatively low field strengths/magnetic flux densities [76]. Thereby the micromotor geometry is crucial for an adequate and effective operation with this actuation mechanism, apart from the magnetic susceptibility of the material, of course. The actuation of magnetic micromotors that convert rotation to forward propulsion, so-called micropropellers, will be discussed in the following section. Another important aspect considering biocompatibility is the necessity to retrieve the micromotors from the body after they have completed their task. This is arguably easier for physically actuated micromotors than for chemical or biohybrid ones which can only be controlled by chemical gradients, which are hard to control *in vivo*. Works have been published on the possibility to retrieve magnetic microagents from the bloodstream after they have completed their task [77], [78]. Moreover, magnetic micropropellers can in principle backtrack their journey through the body as the external actuation can be reversed accordingly. A more elegant approach, analogous to the disposal of intruding bacteria by the immune system, could be to compose micromotors of biodegradable materials so that they can be resorbed by the body (fluids) within an adequate timeframe. Recent studies have demonstrated the feasibility of this approach with magnetic micromotors [79]–[81] and others [82], [83], which have to be tailored to the biochemical environment at the desired application site (and are often limited in that sense). Ultimately, real-time feedback and supervision of micromotors for deep-tissue *in vivo* operations, i.e. deep inside the body, remain the biggest hurdle in the field. Few works have been published that report *in vivo* imaging of flocks of micromotors in mice [66], [84]. Considering the currently prevalent technologies, fluorescence imaging lacks deep-tissue penetration, while magnetic resonance imaging (MRI) and ultrasound imaging lack resolution [85]–[87].

However, this field is on the move owing to its ever-increasing relevance for a variety of biomedical applications, as can be concluded from promising technologies that recently came into focus, e.g. magnetic particle imaging [88], [89] and photoacoustic imaging [90], [91], also combined with endoscope-based approaches [92]. For example, real-time imaging of individual micromotors of 100 μm length below 1 cm thick tissue samples has been reported recently [93]. As outlined in the Introduction, the present work addresses the application of micromotors in ART, i.e. the operation of microscale cell carriers in the female reproductive tract, especially the fallopian tubes. In this case, deep-tissue imaging below ca. 10 cm of sensitive tissue is necessary to supervise and control untethered micromotors inside the fallopian tube. Within the scope of this dissertation, this challenge must remain for the future, as *in vivo* experiments have not been conducted as of yet. Considering the other discussed requirements for the *in vivo* operation of micromotors for the proposed applications, achieved progress will be presented and discussed in the main part of the dissertation (sections 4 and 5).

2.3 Magnetic Micropropellers

As outlined in the preceding sections, magnetic actuation is especially suited for micromotors for biomedical *in vivo* applications because of the biocompatibility, long-range pervasion, and excellent controllability of magnetic fields, especially RMFs. The most commonly applied and studied type of magnetic micromotor which is actuated by an external RMF has a rigid helical shape and was popularized under the name "artificial bacterial flagella" [94]–[96], owing to its resemblance with real bacterial flagella, whose shape and function had been already characterized and studied for years [97]. In principle, also other shapes different from the helix can move and propel in a liquid medium at the microscale when actuated by an RMF, provided they are chiral, according to E. M. Purcell's much-cited "scallop theorem" [21], [98]. The physics of such magnetically actuated, rotating micropropellers are reviewed in the following section.

2.3.1 Theory

In short, the aforementioned scallop theorem is a consequence of the dominance of viscous drag forces over time-dependent inertia at the microscale in a liquid medium, and states that in order to move forward in the medium, a described object must perform a non-reciprocal motion or deformation, unlike a scallop whose open-and-close-mechanism is completely symmetric when the acceleration and duration of

opening and closing, i.e. time-dependency, is completely damped by viscous drag [21]. The conditions under which such a scallop swimmer cannot move forward, i.e. where its attempt to generate thrust by closing its shell much faster than it opened it will be damped out by the surrounding medium's viscosity, can be described by the Reynolds number (Re), a dimensionless index that expresses the ratio of inertial to viscous forces [21]:

$$Re = \frac{\rho \cdot u \cdot l}{\eta} \quad (I)$$

The inertial forces are described by a product of the constant fluid density ρ and a characteristic velocity u and length l of a swimming body. The viscous forces are sufficiently described by the constant fluid viscosity η in that case. Consequently, if a swimming body is extremely small (small l), the fluid's viscosity will dominate the force balance and Re as an indicator will be much smaller than 1. Re itself is obtained from the Navier-Stokes equation that describes fluid motion in general, when it is non-dimensionalized in time and space with u and l [76]:

$$-\nabla p + \eta \nabla^2 v = \rho \frac{\partial v}{\partial t} + \rho(v \cdot \nabla)v \quad (II.a)$$

$$-\nabla \tilde{p} + \eta \nabla^2 \tilde{v} = \left(\frac{\rho \cdot u \cdot l}{\eta} \right) \frac{d\tilde{v}}{dt} = Re \cdot \frac{d\tilde{v}}{dt} \quad (II.b)$$

Here, equation (II.a) is the Navier-Stokes equation for an incompressible Newtonian fluid of a flow velocity field v and pressure field p , with fluid density ρ and viscosity η . Equation (II.b) is its transformation with non-dimensionalized velocity vector and pressure scalar fields, both marked with a tilde, revealing Re as in equation (I). At the microscale, when $Re \ll 1$, (II) approximates to the Stokes equation, which is linear and independent of time (t) and therefore much easier to handle [98]:

$$-\nabla p + \eta \nabla^2 \vec{v} = 0 \quad (III)$$

The time-independence of (III) illustrates the completely symmetric reversibility of the acts of displacing fluid by opening and closing a scallop at the microscale and thus the futility of trying to move forward with such a reciprocal movement. Analogous to how such a scallop would only go back and forth indefinitely, a simple rudder similar to a stiff tailfin would only go left and right. This is presumably the main reason for the natural evolution of flagellar motors of motile microorganisms, as these can translate simple back-and-forth or rotating actuation of motor proteins into non-reciprocal,

undulating or helical beating patterns owing to their structural flexibility. Trying to synthetically reproduce such a swimming strategy, there is one major difficulty: Unlike motor proteins, synthetic molecular motors are not sufficiently developed yet to be integrated into a micromotor as an on-board actuator. Therefore, an RMF is the method of choice to actuate an artificial flagellum externally, as mentioned above. Following this actuation principle, it is straightforward to fabricate rigid helical or otherwise chiral, ferromagnetic (metal) structures with current microfabrication technologies to achieve non-reciprocal propulsion based on magnetically induced rotation in a defined and reproducible manner, rather than fabricating elastic, flexible filaments (which has been, however, also done, as in [32]). The forward motion of rigid chiral filaments such as helices in a viscous liquid at low Reynolds number conditions was investigated in several studies by many different groups, both theoretically [99]–[102] and experimentally [96], [103]–[106]. The basics of the magnetic actuation of such micromotors are reviewed as follows. First, because of the linearity of (III), any external force F and torque T on a solid body in a fluid at low Re will translate linearly to a velocity v and rotation rate ω of the body, and a simple propulsion matrix can be deduced [98]:

$$\begin{pmatrix} F \\ T \end{pmatrix} = \begin{pmatrix} a & b \\ b^T & c \end{pmatrix} \cdot \begin{pmatrix} v \\ \omega \end{pmatrix} \quad (\text{IV})$$

In this equation that only considers force and velocity components along the long axis of the swimmer, a , b , b^T , and c denote geometric parameters, i.e. the swimmer's shape. In order to fulfill the requirement of non-reciprocal motion, the solid body swimmer has to be chiral, i.e. a , b , b^T , and c have to be anisotropic in terms of geometrical anisotropy which means that there is a preferred direction of translation in the fluid when F or T act on the body owing to the anisotropic drag distribution along its shape [98]. For example, when a rigid helix rotates around its long axis in a fluid, actuated by a torque T , it will not only have a rotational velocity ω , but also a resulting translational velocity v as a consequence of drag anisotropy, i.e. it will propel forward along its long axis similar to a corkscrew through a cork. With such a defined shape, a , b ($= b^T$ in that case) and c can be calculated. This has been done and reviewed extensively in the literature [76] as the slender microhelix is one of the best-researched microswimmer shapes since its first implementation at the microscale in 2009 [94]–[96], as already mentioned above.

$$a = 2\pi nR \cdot \left(\frac{C_p \cos^2 \theta + C_n \sin^2 \theta}{\sin \theta} \right) \quad (\text{V.a})$$

$$b = 2\pi n R^2 \cdot (C_p - C_n) \cdot \cos\theta \quad (\text{V.b})$$

$$c = 2\pi n R^3 \cdot \left(\frac{C_p \sin^2\theta + C_n \cos^2\theta}{\sin\theta} \right) \quad (\text{V.c})$$

The dimensions of a helix are given by its radius R , its helical pitch angle θ , and the number of windings n . The viscous drag coefficients C_p and C_n are also dependent on R and n , as well as on the filament width of the helix and the viscosity of the surrounding fluid [76]. C_p and C_n directly describe the relation of shape anisotropy and viscous drag, as they account for different drag parallel (C_p) and normal (C_n) to the swimming direction, respectively [76]. Such a helix and other chiral bodies are suitable microswimmer geometries as they can be easily actuated and controlled by an external RMF. Especially for biomedical *in vivo* applications, an RMF is a potent energy supply, as discussed already. The efficiency of this magnetic actuation, as well as of the corkscrew propeller swimming principle in general, has been subject of considerations that started already with E. M. Purcell's famous lecture [21], [107]. Compared with simply pulling a magnetic body with a strong gradient magnetic field, the strategy of rotating and corkscrewing could appear to be overcomplicated, nonetheless it is well justified at the microscale. As the maximum magnetization of a body scales down unfavorably with its size while drag forces increase drastically in relation, extremely large field gradients are necessary to pull a small body, especially regarding the necessary long-range interaction when externally controlling a micromotor that operates *in vivo* [76]. On the contrary, a relatively weak field and magnetization is sufficient to deflect a small microswimmer (similar to a compass needle) and make it rotate, imposed by a largely homogeneous RMF that is externally applied, similar to an MRI scanner. Moreover, as the swimming direction of a helix is defined by its axis of rotation, it can be easily controlled and steered by altering the orientation axis of the externally applied RMF. Returning to the propulsion matrix (IV), the external force F_{ext} and torque T_{ext} on a magnetic micromotor are given as [76]:

$$F_{ext} = \mu_0 V (M \nabla) H = V (M \nabla) B \quad (\text{VI.a})$$

$$T_{ext} = \mu_0 V M \times H = V M \times B \quad (\text{VI.b})$$

Here, μ_0 is the permeability of free space and V is the volume of a micropropeller with magnetization M in a magnetic field of strength H or flux density B , respectively. Generally, the sums of external (magnetic) and internal (drag) forces and torques are

both zero when the micropropeller rotates stably in the RMF. As mentioned above, the applied RMF is usually homogeneous, i.e. with no field gradient, so that $F_{ext} = 0$. With that, the micropropeller's propulsion velocity can be derived easily from the applied torque when the geometric parameters of the propeller are known, following (V):

$$F = av + b\omega \rightarrow F_{ext} = 0 \quad (\text{VII.a})$$

$$T = bv + c\omega \rightarrow v_{max} = \frac{b}{b^2 - ac} \cdot T_{ext} \quad (\text{VII.b})$$

The propulsion velocity is at the maximum v_{max} when the propeller exactly follows the rotation frequency f_{ext} (or ω_{ext}) of the external RMF. The capability to do so depends on B and M , i.e. the magnetic properties of the field and propeller, respectively. In that (ideal) case, one has:

$$v_{max} = -\frac{b}{a} \cdot \omega_{ext} = -2\pi \cdot \frac{b}{a} \cdot f_{ext} \quad (\text{VIII.a})$$

$$v_{max} = \pi R \cdot \frac{(C_n - C_p) \cdot \sin\theta \cos\theta}{C_n \sin^2\theta + C_p \cos^2\theta} \cdot f_{ext} \quad (\text{VIII.b})$$

So, with the viscous drag coefficients of a slender helix as in (V), it becomes apparent that the main geometrical parameters that define the velocity of a helical micropropeller actuated by an RMF with f_{ext} are R and θ , but not n , i.e. the number of windings is not important [76]. This is valid when the helix is rotating about its long axis – which is not given for all f_{ext} , depending on M , as was experimentally observed and has been discussed in several works [96], [100], [105]. Helical micropropellers are made susceptible to an RMF usually by attaching a hard- or soft-magnetic head to the helix [94], by coating the entire helix with a soft-magnetic coating [95], [108]–[110], or by dispersing superparamagnetic nanoparticles in the composite matrix of the helix material [111]. Typically, a soft-magnetic microhelix with several micrometers in diameter and several tens of micrometers in length that is magnetized perpendicular to its long axis rotates and propels stably in a range of approximately 1 – 100 Hz. At the lowest frequencies, such a helix is at first rotating, or tumbling, about its short axis and then, at low frequencies, aligning to rotate about its long axis, albeit "wobbling" around that axis while propelling forward. With increasing frequency, the helix rotates more stably and smoothly, and the propulsion velocity increases linearly with f_{ext} . At a certain frequency, the helix can no longer follow the externally imposed rotation because of the time lag of the magnetic realignment of the structure –

dependent on B and M – and the propulsion efficiency decreases abruptly. Accordingly, this frequency was termed "step-out frequency" [96], [100], [112]. Tumbling, wobbling, and step-out frequency regimes are extremely sensitive to slight alterations of the micropropeller geometry and magnetization [110]–[112], and are harder to predict than the linear corkscrew propulsion described in (VIII.b). Therefore, the fabrication of uniform and reproducible micropropellers is particularly important for achieving optimal and reliable swimming performance.

2.3.2 Implementation

Generally, magnetic micropropellers are actuated by a set of electromagnetic coils that are arranged to generate an RMF that is homogeneous in a working space that is suited to observe the swimming microstructures in a Petri dish or microfluidic channel platform under a microscope. Helmholtz coil setups with three orthogonally placed pairs of coils have been implemented [113]–[115], modifications of these [109], and also a planar array of eight tilted coils that point towards a focal volume that is more easily accessible with a microscope objective on the other side of the array has been reported (and commercialized) [116]. These systems generate a magnetic flux density of up to 20 mT, which is at least 50 times weaker than clinically applied MRI fields, which are usually in the range of 1 – 4 T [73]–[75]. Microhelices that exhibited the described corkscrew propulsion with velocities of approximately 2 bodylengths per second (blps) have been reported [108], [109], [117], [118], which is generally less than what chemical micromotors, especially bubble-ejecting catalytic microtube jets can achieve [29], [119], but still compares well to natural microswimmers such as mammalian sperm [13], [120], [121]. Other magnetically actuated micropropellers which rely more on tumbling or rolling motion instead of corkscrew propulsion can reach greater velocities, yet are often harder to control and less flexible in terms of 3D swimming capability [62], [110], [114], [122], [123]. It is possible to estimate the pushing force that a propelling microhelix generates when it hits an obstacle, by setting $v = 0$ and calculating F from the externally applied ω with (VII.a). This has been done in the literature by calculating the geometric parameter b of a microhelix with a length of 38 μm , and with that estimating the maximum pushing force to be 1.5 pN per mT (applied field) [96]. Compared with that, a mammalian sperm cell appears to be much stronger, with an estimated force in the range of tens of pN which can exceed even 1 nN when hyperactivated, depending on medium rheology and interface adhesion [124]. Nonetheless, the pushing and transport of cargo of various sizes is possible with helices and other magnetic micropropellers, as has been demonstrated in the literature [49], [64], [108] and will also be demonstrated later in this work.

2.4 Microfabrication: Direct Laser Writing

The fabrication of synthetic structures on the microscale (and nanoscale) is one of the essential progresses of the last century, primarily driven by the mass production of integrated circuits on microchips in the semiconductor industry, following the famous Moore's Law [125], [126], and motivated by R. P. Feynman's talk "There's Plenty of Room at the Bottom" in 1959 [127]. Micromotors benefitted from – and also contributed to – this development since the early 21st century. For example, microhelices that can be actuated as magnetic micropropellers as described in the previous section have been fabricated by various technologies. At first by conventional lithography of semiconductor materials [94] modified with strain engineering – a concept of rolling structured layers to helices or tubes during an etching process [128], [129]. Later, glancing angle deposition, a shadow-growth evaporation method [130], [131], was used [95], as well as template-based electrodeposition [132] and the coating of biotemplates, i.e. naturally occurring helical structures such as plant fibers [109], [115] or *Spirulina* cyanobacteria [133]. Recently, 3D printing technologies are becoming increasingly important owing to gradually improving resolution and feasibility, for example microfluidic printing to fabricate helices [134], [135] and – more importantly – 3D laser lithography [62], [81], [108], [117], also termed direct laser writing (DLW). DLW is a lithography process, i.e. based on the principle of structuring photosensitive materials with light. Conventional, two-dimensional (2D) lithography has enabled the aforementioned triumph of the semiconductor industry owing to its microscale resolution and excellent reproducibility. Compared with conventional lithography where flat samples are exposed to ultraviolet (UV) light through a mask, i.e. a screen with hole patterns to selectively expose the desired (microscale) positions on the target material, DLW uses a focused laser beam that can be deflected to selectively expose computer-programmed positions on the sample freely in 3D. Crucial to this strategy is the non-linear optical phenomenon of two-photon absorption (2PA) in a photosensitive polymer material, ensuing two-photon polymerization (2PP) [136], [137]. In conventional lithography, a polymer photoresist is patterned by UV light that is absorbed in the material and changes its chemical structure in the desired areas which in turn alters its solubility. After exposure, the polymer can be "developed", i.e. put into a suitable solvent bath to remove the exposed or unexposed parts of so-called positive or negative tone resist, respectively. The absorption of UV photons by the resist is a linear effect and depends on the wavelength of the used light that has to suit the absorption properties of the resist. Accordingly, a UV laser that would penetrate a 3D sample of negative tone photoresist would polymerize the material all along the secant that the light beam would write into the sample, which would limit its use for free 3D

writing of arbitrary structures. Instead, 2PA is exploited in DLW, i.e. an infrared (IR) laser beam with a wavelength that is conventionally not suited to polymerize the resist is deployed with short pulses (femtosecond range) of extremely high intensity (i.e. many photons) so that the resist can locally be polymerized in the focal point of the laser where the probability is sufficiently high for 2PA to occur, which means that two (low energy) photons are absorbed by the polymer at the same time and thus provide the energy that is necessary to locally initialize the polymerization reaction (Fig. 2.2 A) [136], [137]. The polymerization is limited to a small volume around the focal point, termed voxel (in analogy to a pixel in 2D) where the absorption probability for 2PA is sufficiently high to overcome quenching effects, scaling (and decaying) with the squared intensity of the laser, while conventional absorption scales proportionally with the intensity (Fig. 2.2 B and C) [136], [137].

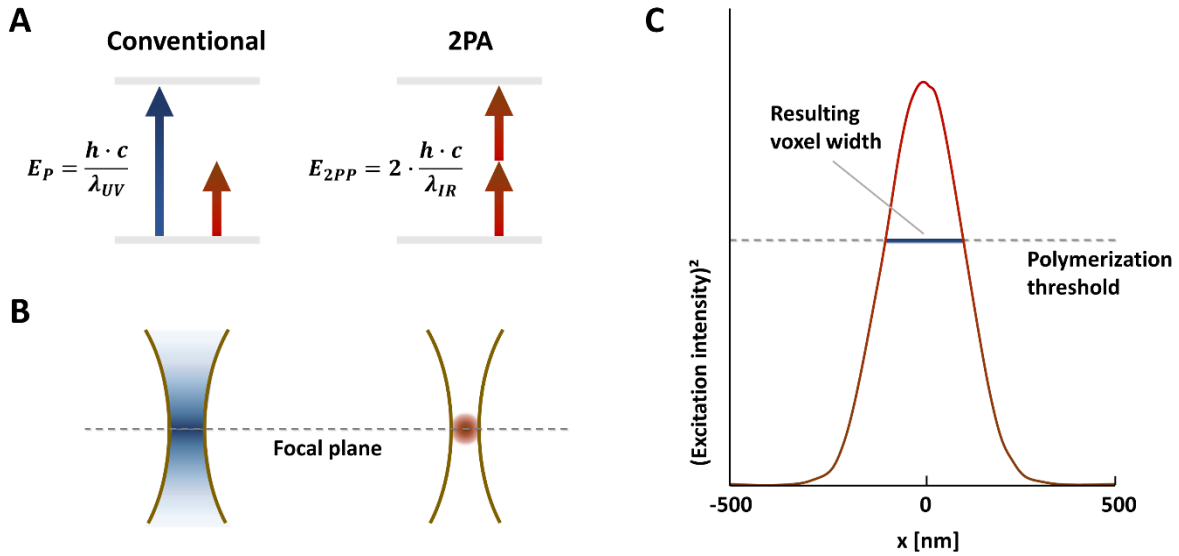


Figure 2.2: Principles of 2PA and 2PP; A) energy transfer schemes of conventional photon absorption and 2PA for polymerization (energy E_P) and 2PP (energy E_{2PP}) with UV (wavelength λ_{UV}) and IR (wavelength λ_{IR}) light, respectively, with the Planck constant h and the speed of light c in vacuum; B) intensity distribution of focused light regarding the two cases of A) and the resulting occurrence of polymerization; C) qualitative relation between (squared) excitation intensity and voxel dimensions in the case of 2PP; all schematics inspired by the "NanoGuide" website of Nanoscribe GmbH, Germany (<https://support.nanoscribe.com/hc/en-gb>).

Consequently, the width of the exposed voxel, i.e. the resolution of DLW in the focal plane, is directly linked to the (squared) intensity of the pulsed laser, while a threshold intensity must be reached to ensure a critical absorption probability for 2PA (and thus 2PP) to occur (polymerization threshold, Fig. 2.2 C). Owing to the shape of the intensity distribution in 3D, the polymerized voxel is elongated along the beam axis normal to the focal plane [136], [137]. The addressed voxel can be controlled (and programmed)

by deflecting the laser beam to scan freely over the desired volume to be exposed and polymerized. Owing to the non-linear nature of 2PA and 2PP, the diffraction limit of conventional lithography can be overcome and structures can be exposed with a (planar) resolution in the range of 200 nm [138] and better [139]. Free, maskless 3D exposure and nanoscale resolution are the main advantages of DLW over conventional lithography, whereas the serial exposure and writing approach naturally bears the disadvantage of much increased writing times as compared with the simultaneous exposure of an entire sample through a mask. For example, although DLW can be controlled precisely and fast with galvanometer scanners and piezo actuators up to scan speeds of 100.000 $\mu\text{m/s}$ and individual microstructures such as helices can be written in a matter of seconds, still the fabrication of arrays of helices with several thousands of structures on one sample will easily require the machine to run continuously overnight or even for several days, depending on the structure. Nevertheless, considering the advantages of high-yield reproducibility of arbitrarily shaped and easily tunable geometries, the technology of DLW was the method of choice to fabricate the micromotors presented in this dissertation, considering the aforementioned fabrication methods. The previously cited publication of helical micromotors fabricated by DLW [108] served as an important orientation for the design and implementation of helical micromotors to manipulate and transport immotile sperm cells, as will be presented in section 4, whereas the flexibility of the DLW technology allowed to realize structural alterations regarding dimensional scaling and functional improvements [140], as well as entirely novel micropropellers for different applications, which will be presented in section 5.

2.5 Assisted Reproductive Technology

The first detailed clinical description of a medical treatment of infertility which evoked broad scientific discussion was published in 1866 in the United States of America [141], [142]. Despite the indignation and disgust that can be found in contemporary comments, there was also genuine scientific interest in the topic, given the undeniable relevance of the infertility problem and the study of the biological mechanisms of reproduction in general [142], [143]. These remain relevant to this day, albeit the public opinion on infertility treatment has changed much in its favor, not least because of an ever growing demand [1]–[3], considering the fact that about 8 – 12 % of the reproductive age population world-wide are affected by infertility nowadays [144] and the success of treatments such as intrauterine insemination and in vitro fertilization (IVF), especially intracytoplasmic sperm injection (ICSI), which are widely available at

least in industrial countries. These techniques, as well as the biological mechanisms of reproduction in general, will be discussed in the following sections to expose in which aspects the application of magnetic micromotors can benefit ART to treat infertility in the 21st century.

2.5.1 In vitro Fertilization and Intracytoplasmic Sperm Injection

IVF is an approach that is fundamentally different from conventional therapies that are based on medication or surgery. Medication means the ingestion of substances into the body that work therapeutically, unseen by the outside observer. Surgery means the invasive opening of the body to access and restore functions in the body manually. IVF is based on the concept of explanting cells (gametes, i.e. germ cells in this case) from the body to a laboratory (i.e. *in vitro*) setup to manually perform the desired function (fertilization in this case), and then reimplanting the treated cells (the fertilized oocyte, i.e. embryo) to the body, ideally without any perceivable physiological difference between natural and *in vitro*-effected result (natural and IVF-assisted pregnancy). As such, IVF offers many more options to remedy different causes of infertility than for example intrauterine insemination, i.e. placing sperm into the uterus with a catheter [145], given that the two gametes, oocyte and sperm, can be freely manipulated with suitable medical devices under the microscope. The first report on a successful childbirth conceived by IVF has been reported in 1978 by Steptoe and Edwards [146], awarded with the Nobel Prize in Physiology or Medicine to Edwards in 2010 [17]. Presenting an important extension of the IVF procedure, pregnancies by ICSI have been reported and published in 1992 [147]. In the conventional IVF routine an oocyte is simply co-incubated with motile sperm in a Petri dish, whereas in ICSI a single sperm cell is aspirated and injected manually into the oocyte with a microinjection needle. This procedure allows to remedy severe cases of oligozoospermia and asthenozoospermia, i.e. when there are only few sperm cells in the semen or when the sperm cells are immotile, respectively. These two conditions are two main causes of male infertility and are in the focus of the micromotor-assisted reproduction concepts which have been introduced and will be discussed further in this thesis – the former published by Magdanz et al. [13] and the latter published by Medina-Sánchez and Schwarz et al. [15], representing parts of the author's work which will be discussed in detail in section 4.

2.5.2 Embryo Transfer and Zygote Intrafallopian Transfer

IVF can be divided into two major steps, fertilization and embryo development. ICSI, as a purely mechanical act of bringing sperm and oocyte together, is apparently sufficient to yield high fertilization success rates of over 90 % per IVF cycle [1]–[3] (assuming proper means of selection for qualified gametes). Conversely, the process of subsequent *in vitro* development of the fertilized oocyte, the zygote, to a multicellular embryo that can be implanted into the mother's uterus and "hatch" there, is presumably more complicated and challenging, as comparatively low success rates of approximately 30 % for successful embryo transfer (ET) and resulting clinical pregnancy [1]–[3] suggest. Generally, embryos are cultured *in vitro* for 5 days after IVF before ET to the uterus is performed [1]–[3]. Earlier ET could be advantageous, as the embryo then can undergo its development in its natural *in vivo* environment [148], i.e. inside the mother's body, whereas longer *in vitro* culture makes it easier to select the most promising among several cultured embryos [149], which is especially important in the case of elective single embryo transfer (eSET) – when only one embryo is transferred – a practice that is becoming increasingly relevant to avoid unwanted multiple pregnancies [1]–[3]. However, the main hindrance for early embryo transfer is the fact that, in the natural case, the oocyte is usually fertilized shortly after ovulation, at the beginning of its journey through the fallopian tube (also termed oviduct), and travels through the oviduct for several days while it undergoes its development from a zygote to an embryo that is ready to hatch and lodge itself in the uterine wall [150], [151]. That means that it is necessary to transfer an IVF-conceived zygote into the fallopian tube to undergo fully natural embryo development, which is much more complicated than implantation into the uterus. A surgical procedure, so-called laparoscopy, where incisions have to be made to access the pelvic cavity with a laparoscope and catheter, is necessary to perform zygote intrafallopian transfer (ZIFT), i.e. to inject a zygote directly into the oviduct [152]. This surgery, entailing risks and stress on the body as most other invasive therapies, is presumably the main reason why studies on the overall success rate of ZIFT indicated no clear advantages over later ET or eSET, although different infertility cases can make one or the other more favorable [153]–[155]. Apparently, the advantage of *in vivo* embryo development is compromised by the disadvantages of the invasive surgery procedure. This is the crucial point where a magnetic micromotor could provide a remedy as it could load a freshly IVF-conceived zygote, be transferred to the uterus, and transport the zygote into the fallopian tube non-invasively, under external actuation and supervision. This concept of micromotor-assisted ZIFT has been conceived by Medina-Sánchez (the

group leader) and published by Schwarz et al. [156], [157], representing parts of the author's work which will be discussed in detail in section 5.

2.5.3 The Sperm Cell and the Oocyte

The subject of this thesis is the manipulation and transport of sperm cells and fertilized oocytes by micromotors for micromotor-assisted fertilization and ZIFT, respectively. Therefore, the characteristics of the male and female gamete and their natural roles in fertilization shall be discussed in this section. Fig. 2.3 A displays the general anatomy of a human sperm cell that can be divided into three principal parts – head, midpiece, and tail – which is true for all mammalian sperm species, despite varying sizes [158], [159]. The most important part, the nucleus with the haploid set of chromosomes, is contained in the sperm head. The sperm tail is responsible for the cell's motility, comprising a fibrous sheath that contains the so-called axoneme, a set of microtubules with dynein motor proteins that actuate the whiplash beating of the tail [159]. The midpiece is connecting head and tail, and contains a large density of mitochondria to supply chemical energy for the cell [159].

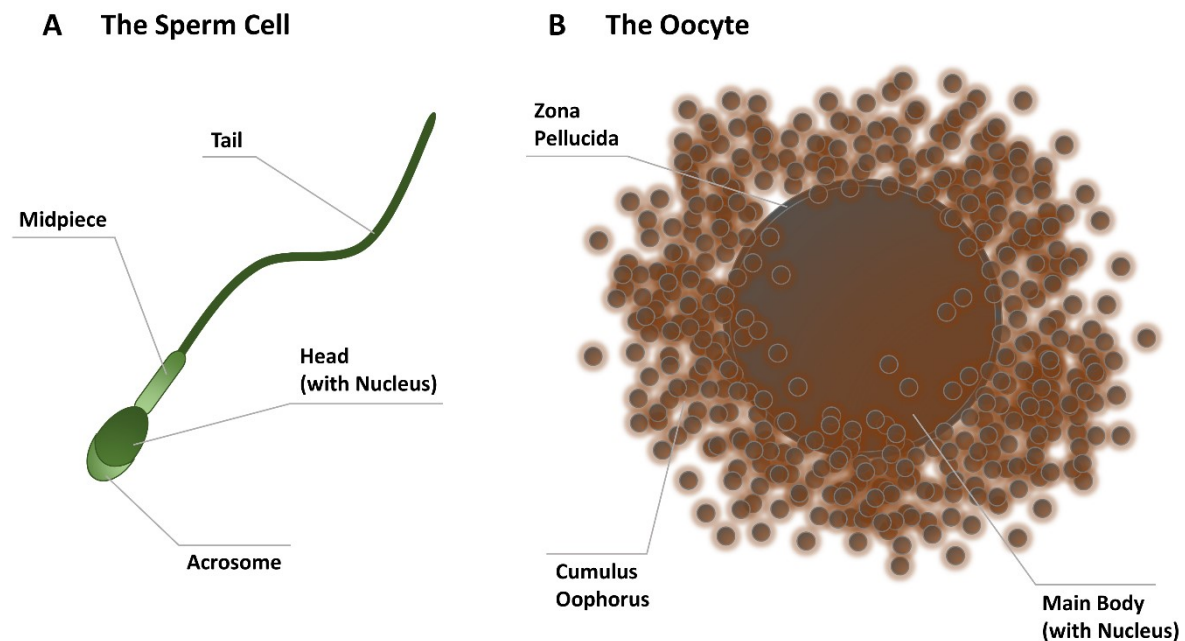


Figure 2.3: Principal anatomy of the male and female gamete; A) the sperm cell; B) the oocyte (not to scale).

The acrosome is a special compartment of the cell in the front part of the sperm head and is important for binding to and fusing with the oocyte [159], [160]. The sperm head will open its cell membrane and release biochemical substances during the acrosome reaction, which plays an essential role in the fertilization process, along with

hyperactivation, a dramatic increase in beating amplitude and frequency of the sperm tail [160]. Acrosome reaction and hyperactivation are the two major symptoms of sperm capacitation, which describes a series of biochemical reactions that naturally proceed when sperm cells are inside the fallopian tube (and can also be induced *in vitro*) to render them ready and able to fertilize [160], [161]. Fig. 2.3 B displays the principal architecture of a mammalian oocyte, which right after ovulation is surrounded by a cluster of follicle cells, forming the so-called cumulus-oocyte complex (COC) [148], [162]. The main body, the actual oocyte, is embedded in the hyaluronan-mediated network of follicle cells, the so-called cumulus oophorus (or simply cumulus) which will loosen up during oocyte maturation and ultimately disintegrate after fertilization [148], [162]. The zona pellucida, a glycoprotein shell that surrounds the oocyte, remains until the embryo hatches and serves to bind sperm cells selectively and protect the oocyte from polyspermy, i.e. fertilization by more than one sperm [163]. The qualities of both cumulus and zona pellucida impose requirements on the sperm cells that have to work both competitively and cooperatively to achieve fertilization. It is commonly pictured that the fastest sperm cell reaches the oocyte first and outdoes the others, although in reality swimming speed is only one of many abilities that sperm rely on. They benefit from traveling as a large group, overcoming obstacles such as the cervix and the complex, folded structure of the inner fallopian tube [164], [165]. They attach to the ciliated epithelial cells that line the oviduct lumen, a process which presumably serves to store sperm and can also play a role in triggering sperm capacitation [151], [161]. Ultimately, they reach the oocyte and become stuck in the cumulus, which could be helpful to prevent polyspermy, yet also promotes the gathering of many sperm cells in close vicinity to the oocyte [166], [167]. Individually and collectively, the hyperactivated sperm tail beating serves to disaggregate the cumulus cells and burrow through. At this point, premature acrosome reaction of several sperm cells can release hyaluronidase, an enzyme that can sever the hyaluronan network of the cumulus chemically [151], [168]. Sperm cells with intact acrosomes can in turn bind to the zona pellucida when they reach it, and one sperm will be accepted to penetrate the zona pellucida, fuse with the oocyte, and fertilize [163]. Regarding fertilization and the described concomitant phenomena, there are differences between the various secreted chemicals and sperm receptors on the zona pellucida regarding different mammal species, and many of the mechanisms are not clearly understood yet [161], [169]. As described in the previous section, it is possible to circumvent the majority of these processes with ICSI and still achieve fertilization *in vitro*. It has been reported that this can lead to pregnancy and childbirth even with completely immotile sperm [170]–[173]. The motility of a sperm cell can often be an indicator, yet is not a precondition for a healthy and fertile sperm head that contains

the essential information – the chromosomes, comprising deoxyribonucleic acid (DNA). Fertilization naturally occurs shortly after ovulation, when the oocyte is still at the beginning of its journey through the oviduct. After fertilization, the zygote continues to travel by muscle contractions along the oviduct, oviduct fluid flow and the beating of ciliated oviduct epithelial cells, and undergoes multiple cell divisions during these early stages of embryo development until it reaches the uterus, usually at day 5 after fertilization, where it hatches, i.e. breaks out from the zona pellucida, and implants into the uterine wall to continue its development to a fetus [150], [151]. These early stages of embryo development were illustrated in Fig. 1 in the Introduction and are usually all part of the IVF cell culture routine before an embryo is reimplanted into the uterus.

2.6 Towards Micromotor-Assisted Reproduction

As discussed in section 2.2, the key challenges that micromotors for biomedical applications in general must face lie in the transfer of *in vitro* experiments to *in vivo* (animal) testing, most importantly considering possible risks to the health of the patient and necessary *in vivo* imaging of the microscopic agents. Although at this stage animal testing was beyond the scope of the work presented in this dissertation and for instance the challenge of *in vivo* imaging must be addressed in future work, other important steps towards *in vivo* application were achieved and will be presented in the two main parts of this thesis (sections 4 and 5). In section 4, the following questions will be addressed regarding micromotor-assisted fertilization: Can a micromotor couple to a single immotile sperm cell and move it via magnetic actuation? Does the resulting spermbot's performance compare well with motile sperm, i.e. is it able to emulate the swimming behavior of motile sperm and reach the oocyte? How do we select and pick up a sperm cell that is immotile, yet still alive and intact, i.e. in principle able to fertilize? Can the captured sperm be delivered to the oocyte, i.e. be released from the micromotor and bind to the zona pellucida? How do we monitor (and preserve) the sperm's viability during and after delivery? Is it possible to emulate the behavior of motile sperm during the steps of natural fertilization solely by mechanical (magnetic) actuation of immotile sperm or is it necessary to also emulate certain biochemical reactions? In section 5, slightly different questions will be addressed considering micromotor-assisted ZIFT: Can a micromotor couple to a single oocyte/zygote and move it via magnetic actuation? What is a suitable micromotor architecture to capture this large, spherical cell safely and in a reversible manner, solely by magnetic actuation? What are the differences between the novel architecture and the established

helical propellers regarding swimming performance, especially considering the navigation in high-viscosity media and narrow channels? Is the cell-micromotor-coupling sufficiently resilient to withstand macroscale handling procedures such as pipetting between different environments, considering the necessity of intrauterine injection for *in vivo* application? Is it possible to analyze and confirm the proposed benefits of *in vivo* embryo development after successful micromotor-assisted delivery also in an *in vitro* setup? How could such a system be implemented in the laboratory? The materials and methods that were used in the experiments that were conducted to answer these questions in the course of the presented work are summarized in the next section.

3 Materials and Methods

All chemicals were ordered from Sigma-Aldrich® (Merck KGaA, Germany), if not stated otherwise (in brackets). Laboratory supplies and disposables were ordered from VWR™ (VWR International GmbH, Germany).

3.1 Fabrication of Microfluidic Channel Platforms

Different types of microfluidic channels were prepared to investigate micromotors with and without cells under the microscope. These channel platforms were used to avoid the evaporation of liquid medium during experiments while simulating *in vivo* conditions by providing a confined environment for the demonstration of micromotor navigation and cargo transport capabilities.

3.1.1 Tailored Parafilm Channels

Parafilm (Parafilm® M polyolefin film, Merck KGaA, Germany) was folded to three layers and cut with the Silhouette electronic desktop cutting system (Silhouette CAMEO®, Silhouette America Inc., USA). The cut stacks of parafilm were pressed between a 25 x 76 mm² glass slide and a 24 x 60 mm² glass cover slip, or between a 24 x 60 mm² and a 22 x 22 mm² glass cover slip, and partially melted on a heating plate at 120°C for 1 – 2 min to bond the pieces together and form an open channel platform of parafilm walls between glass. Channel layouts were designed with the Silhouette software (Silhouette Studio, Silhouette America Inc., USA), examples are displayed in Fig. 3.1 A and B. Before adding liquid medium with cells and/or micromotors to the channels, the parafilm platforms were flushed with isopropanol and deionized (DI) water, filled with pluronic solution (10 µg/ml Pluronic® F-127 in DI water) and incubated at 37°C for at least 1 h (typically overnight). Pluronic® F-127 is a biocompatible, non-ionic detergent that has been applied as a cell-repellent surface functionalization to avoid unspecific adhesion and sticking of cells, e.g. *bovine* sperm, on the microchannel substrate [174], [175]. Alternatively, a poly(L-lysine)-grafted-poly(ethylene glycol) (PLL-g-PEG) functionalization was applied for the same reasons, as the increased hydrophobicity of poly(ethylene glycol) (PEG) is well-known [176] and was verified with PLL-g-PEG-coated glass cover slips by in-house contact angle measurements (CAM 101, KSV Instruments Ltd., Finland). PLL-g-PEG solution (100 µg/ml in DI water) was also simply pipetted into the parafilm channels, left for 1 h at room temperature (RT),

and then rinsed with DI water to remove excess molecules that did not adsorb to the microchannel surface.

3.1.2 Polymer Channels Cast from Micromolds

Polydimethylsiloxane (PDMS) microchannels were cast from two different kinds of molds. A poly(methyl methacrylate) (PMMA) mold was micromachined in the in-house mechanical workshop according to a customized layout to obtain defined, multifunctional and easily reproducible microchannel platforms with channel width and height of 1 mm (Fig. 3.1 C). For more specific architectures, different molds were fabricated from epoxy-based photoresist (SU-8 10, MicroChem Corp., USA) on silicon wafers. Different template layouts were created with a computer-aided design program (A9CAD, A9Tech Inc., USA) and patterned into SU-8 in a maskless lithography system (μ PG 501 micro pattern generator, Heidelberg Instruments Mikrotechnik GmbH, Germany). For that, an adhesion promotor (TI Prime, MicroChemicals GmbH, Germany) was spin-coated onto a silicon wafer (for 30 s at 3500 rpm) which was then baked at 120°C on a heating plate for 2 min, before spin coating of SU-8 onto the wafer (for 60 s at 3500 rpm) and subsequent prebaking at 65°C for 4 min and 95°C for 10 min, with heat ramps of 40 min before each temperature step, respectively. After exposure of the photoresist in the aforementioned lithography system (exposure time 1500 ms, laser wavelength 390 nm), the patterned wafer was postbaked at 65°C for 2 min and 95°C for 4 min, with heat ramps of 40 min before each temperature step, respectively, and developed in a suitable solvent (mr-Dev 600, Micro Resist Technology GmbH, Germany) for 1 min. Ultimately, the wafer was hardbaked at 120°C for 2 min. The obtained height of the SU-8 microchannel template was measured with a tactile profilometer (DektakXT[®] Stylus Profiler, Bruker Corp., USA). Liquid PDMS, mixed from a silicone elastomer kit of base and curing agent in the ratio 10 to 1 (Sylgard[™] 184, The Dow Chemical Company, USA), was filled into the two different molds and cured on a heating plate for 4 – 12 h at 65°C. The PMMA mold was designed to hold PDMS for four microfluidic chips of a total height of 2 mm and an area of 20 x 20 mm² each, whereas the edges of a silicon wafer with patterned SU-8 had to be walled with aluminum foil and adhesive strips to form a proper mold that could be filled. Bubbles that formed in the silicone elastomer mixture during mixing of base and curing agent with a spatula in a separate beaker were removed in a desiccator before curing. After curing, the solidified PDMS was cut with a scalpel to obtain multiple microfluidic chips, according to the respective mold design, which were then pierced with a 2 mm punch to obtain channel inlets and outlets. The PDMS channels were manually fixed onto 22 x 22 mm² or 24 x 60 mm² glass cover slips after activation with oxygen plasma (Femto

low-pressure plasma system, Diener Electronic GmbH & Co. KG, Germany) of the corresponding surfaces of both parts for 30 s and bonded together on a heating plate at 65°C for 1 – 2 h. Before injecting liquid medium that contained cells and/or micromotors, the channels were functionalized with pluronic solution analogous to parafilm channels as described in the previous section.

3.1.3 Tubular Channels to Mimic *In vivo* Ducts

Tubular channels with reduced diameters in comparison to the previously described parafilm and PDMS channels were used to mimic confined *in vivo* environments such as the oviduct. Commercially available polytetrafluorethylene (PTFE) tubings with an inner diameter of 500 μm (Fig. 3.1 D), as well as standard polypropylene 10 μl pipette tips (Fig. 3.1 E), both from VWR™, were utilized for this purpose. Both were trimmed to pieces of ca. 2 cm length and fixed individually on 24 x 60 mm² glass cover slips with adhesive tape after adding liquid medium by pipetting, containing the cells and/or micromotors that were to be investigated. The intake of medium by pipetting was achieved after trimming the channels, by attaching them to larger (100 μl) pipette tips and sucking through them with the pipette. Leakage of medium was not observed after fixation, owing to capillary forces. Note that tubular channels were not functionalized, as no adhesion of cells or micromotors to the walls had been observed.

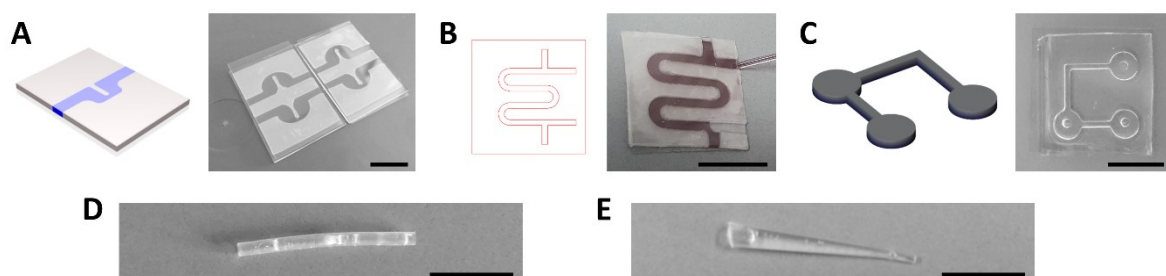


Figure 3.1: Examples of fabricated microfluidic channel platforms; A) illustration and photograph of parafilm chips with separated chambers with a channel height of ca. 300 μm ; B) Silhouette layout and photograph of a parafilm chip with a branched channel of ca. 300 μm height; C) computer-aided design layout of a micromold with channel width and height of 1 mm and three basins of 5 mm diameter, photograph of a respective PDMS channel platform; D) trimmed PTFE tubing; E) trimmed 10 μl pipette tip (all scale bars 1 cm).

3.2 Fabrication of Magnetic Micropropellers

The fabrication of magnetic micropropellers was divided into three steps. First, the structure of a micropropeller was formed from polymer material by means of

lithography. Second, the structure was coated with ferromagnetic metal. Third, the micromotor was chemically functionalized to tune its surface properties to fit the experimental requirements.

3.2.1 Direct Laser Writing of Polymeric Resin

The functional principle of direct laser writing, or 3D laser lithography, was described in the Fundamentals (section 2.4). Analogous to conventional lithography, the process consisted of microstructure design, tool programming, exposure to (laser) light, and chemical development of the photoresist.

3.2.1.1 Design and Programming

All fabricated micromotors were designed and programmed in the Nanoscribe DLW preparation software (DeScribe, Nanoscribe GmbH, Germany), a general writing language (GWL) editor. In this program, all spots and lines that were to be addressed by the Nanoscribe laser for 2PP patterning were assigned to x-, y-, and z-coordinates, following mathematical functions that, for example, described a helix in cylindrical coordinates to pattern the desired microstructure. Moreover, necessary stage movements and loops to write multiple identical structures were programmed, as well as exposure parameters such as line number, line distance, laser power and scan speed. Annotated scripts for arrays of the three principal structures of micromotors applied in this work are attached in the Appendix. Fig. 3.2 depicts the structures that were designed and applied in this work. The structures are generally classified as microhelices, large helices, and spirals. Microhelices were programmed with a fixed diameter of 4 μm and variable length, depending on the pitch length and the number of windings. Most experiments presented in this thesis were conducted with microhelices with a pitch of 6.5 μm and 4 windings, although also helices with 3 windings (with the same pitch length) are discussed at one point. Moreover, helices were designed with a ring at the head end to efficiently couple to immotile sperm cells, although also helices with no ring, or rings at both ends, were fabricated. Further design modifications are not elaborated on in the present work. Large helices in principle are up-scaled versions of the microhelix design (with one head ring), and were programmed with a fixed diameter of 100 μm , a pitch length of 50 μm , and 5 windings. Further design modifications are not presented in this work, although it should be noted that the writing strategy (based on 2PP patterning along programmed lines by DLW) was different from the microhelices, as the large helices required a block-by-block writing of 2D slices with multiple lines instead of writing a bundle of helical lines

freely in 3D into the photoresist. This was necessary to ensure the structural stability of the large structures in the process of 2PP patterning. The same line programming strategy was applied in the design of spiral-type micromotors. The spiral dimensions were determined by one single parameter, the tubular diameter of the open end of the spiral, which was set to 170, 150, 130, or 110 μm . The different sizes were designed to capture spherical cargo particles and cells of different dimensions which will be discussed in section 5.

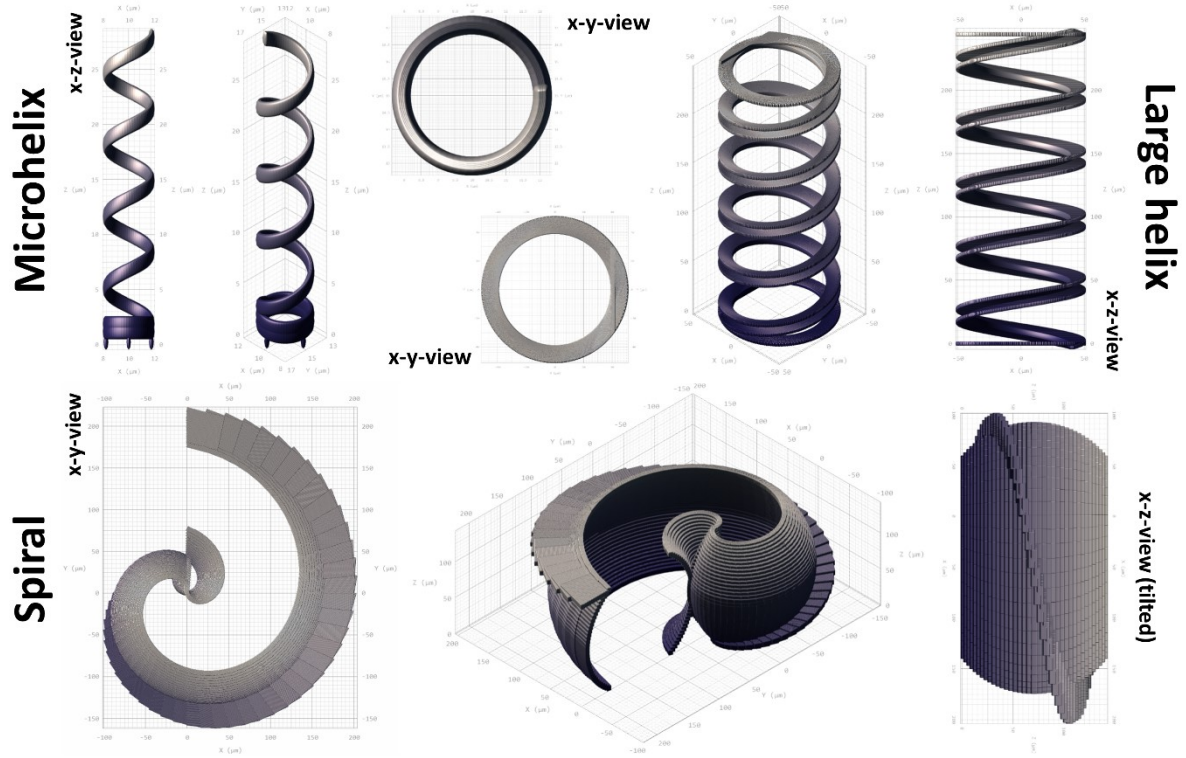


Figure 3.2: DeScribe-screenshots of programmed micromotor structures (not to scale): Microhelix length 28 μm and diameter 4 μm ; large helix length 250 μm and diameter 100 μm ; spiral footprint (length in x-y-view) 390 μm and (tubular opening) diameter 170 μm .

Considering the necessary detachment of DLW-patterned microstructures from their respective substrate (which will be described later), note that microhelices were designed with four small posts at the head ring that connect the structure to the substrate at first, yet will be cut off later during detachment, whereas large helices were designed with a support ring that will be completely cut off later while the (second) head ring at the top of the helix will remain (Fig 3.2). Spirals did not require such "sacrificial" structures as they proved to be sufficiently robust not to be damaged during detachment.

3.2.1.2 Exposure and Development

Two different photoresists were applied to fabricate micromotors by 3D laser lithography via 2PP in a 3D printer termed Nanoscribe (Photonic Professional GT 3D, Nanoscribe GmbH, Germany): a specialized photoresist from the Nanoscribe manufacturer (IP-Dip, Nanoscribe GmbH, Germany) and the alternativeOrmocomp (Ormocomp®, Micro Resist Technology GmbH, Germany) which was chosen for its reportedly better biocompatibility [177]. Both photoresists were simply drop-cast onto a 25 x 25 mm² fused silica substrate that could be mounted into the Nanoscribe. The Nanoscribe graphical user interface (NanoWrite, Nanoscribe GmbH, Germany) was utilized to load the GWL-files that were programmed in DeScribe to guide the automatic exposure in dip-in laser lithography configuration (where the objective lens that focuses the laser directly contacts the resist). After exposure, the respective sample was unmounted and put into a developer bath (mr-Dev 600, Micro Resist Technology GmbH, Germany). IP-Dip samples were developed for 20 min, Ormocomp samples for 10 min in mr-Dev 600. Afterwards, developed samples were put into isopropanol until critical point drying.

3.2.1.3 In Situ Direct Laser Writing

Alternative to patterning photoresist on fused silica substrates, microstructures could also be fabricated directly inside of PDMS microchips that were fabricated on 22 x 22 mm² glass cover slips as described in section 3.1.2. This *in situ* DLW was achieved by filling photoresist into the respective microfluidic channel with a syringe and exposing through the glass substrate upon applying immersion oil on the opposite side of the channel. Therefore, another photoresist from the Nanoscribe manufacturer (IP-L 780, Nanoscribe GmbH, Germany), specialized for this oil immersion configuration, was applied. After exposure, the unpatterned photoresist was washed out by putting the entire microfluidic channel into a bath of mr-Dev 600 developer solution for 20 min and then into isopropanol for at least 12 h.

3.2.2 Critical Point Drying

Developed samples were transferred from their respective isopropanol baths to one of two critical point drying machines (Autosamdri®-931, Tousimis Research Corp., USA and EM CPD300, Leica Microsystems GmbH, Germany) where isopropanol was replaced by (liquid) carbon dioxide (CO₂) which was then evaporated supercritically.

3.2.3 Magnetic Metal Coatings

All micromotor samples were coated with metal multilayers after critical point drying to render them ferromagnetic and biocompatible. Microhelices were coated with a nickel (Ni) layer of 100 nm thickness for magnetic properties and a titanium (Ti) layer of 5 nm for corrosion protection and biocompatibility at first. Later, an additional layer of 10 nm Ti was applied as inner layer before the Ni layer, and the outer Ti layer was also increased to 10 nm thickness. These modifications were implemented to avoid delamination of the entire metal multilayer which otherwise occasionally happened when DI water or other liquid media were added onto the micromotor arrays on the samples. As a mediator for certain surface functionalizations which will be described in the following section, an outermost gold (Au) layer of 5 nm thickness was also added on corresponding samples. All these metal layers were deposited by electron beam evaporation (PLASSYS Bestek Ltd., France) with a deposition rate of 1.5 Å/s. Moreover, the samples were tilted by 15° and rotated at 5 revolutions per minute (rpm) during deposition to ensure homogeneous coatings along the helix axes. Large helices were coated by the same means, albeit with iron (Fe) instead of Ni. A multilayer of 10 nm Ti, 100 nm Fe, and 15 nm Ti (as outer protective layer) was applied with the previously described sample tilt and rotation parameters, albeit with a deposition rate of 2.0 Å/s. Spiral-type micromotor samples were coated by sputtering deposition (DCA Instruments Oy, Finland) with tantalum (Ta) as adhesive and protective layers for Fe, i.e. 10 nm Ta, 100 nm Fe, and 10 nm Ta. Although several minor modifications of the described coatings were carried out, only the multilayer coatings that are relevant in the present work are summarized in table 1.

Table 1: Metal multilayer coatings of applied micromotors

Micromotor type	Coating (from inner to outer layer)
Microhelix (as control)	Ni (100 nm)
Microhelix (early)	Ni (100 nm), Ti (5 nm)
Microhelix (standard)	Ti (10 nm), Ni (100 nm), Ti (10 nm)
Microhelix (to be functionalized)	Ti (10 nm), Ni (100 nm), Ti (10 nm), Au (10 nm)
Microhelix (to be functionalized)	Ti (10 nm), Ni (100 nm), Ti (10 nm), SiO ₂ (10 nm)
All large helices	Ti (10 nm), Fe (100 nm), Ti (15 nm)
All spirals	Ta (10 nm), Fe (100 nm), Ta (10 nm)

Note that the listed silicon dioxide (SiO₂) coatings on certain microhelices were applied by an additional step of electron beam evaporation in a different tool (VTD

Vakuumtechnik Dresden GmbH, Germany) with a deposition rate of 0.5 Å/s and no sample tilt or rotation, to obtain anisotropic SiO₂ coatings with decreasing coating thickness (initially 10 nm) from top to bottom along the helix axes.

3.2.4 Surface Functionalization

Analogous to parafilm and PDMS channels described in section 3.1, micromotor samples were also treated with pluronic solution to avoid adhesion and sticking of cells to the microstructures. For that, the respective fused silica substrates with the patterned and metal-coated microstructures were placed individually into Petri dishes, covered completely with pluronic solution and incubated at 37°C, although only for 30 min at most, and then rinsed with DI water. Spiral-type micromotor samples were subjected to oxygen plasma (Femto low-pressure plasma system, Diener Electronic GmbH & Co. KG, Germany) for 30 s before immersion in pluronic solution to improve the wetting behavior of the microstructures' surfaces, to avoid the formation of gas bubbles inside the tubular micromotor geometries. Moreover, alternative surface functionalizations were applied to several microhelix samples. Helices with an outer Au layer were functionalized with poly(ethylene glycol) methyl ether thiol (PEG-thiol) by immersing the samples in PEG-thiol solution (1 mg/ml in absolute ethanol) overnight at RT on an orbital shaker with 200 rpm. Before immersion, the respective samples were subjected to oxygen plasma as described above to improve the adsorption of PEG-thiol. Similarly, SiO₂-coated helix samples were plasma-treated and immersed in (3-aminopropyl)triethoxysilane (APTES) solution (2 vol% in 93 vol% absolute ethanol and 5 vol% DI water) for 1 h at RT. This silanization treatment was applied to bind the mediator molecules 1-ethyl-3-(3-dimethylaminopropyl) carbodiimide (EDC) and N-hydroxysuccinimide (NHS), to covalently functionalize helices with fluorescent antibodies (Alexa Fluor® 647 secondary antibody, Thermo Fisher Scientific Inc., USA). For that, 1 ml of a 0.1 M solution of EDC in phosphate-buffered saline solution (PBS) was pipetted onto an APTES-treated helix sample (after rinsing the sample with absolute ethanol and PBS). After 1 min, 1 ml of a 0.05 M NHS solution in PBS was added and mixed by pipetting. This NHS solution contained the fluorescent antibody which was added beforehand to a concentration of 0.8 vol%. The functionalized helix sample was incubated for 1 h at RT in darkness and rinsed afterwards with PBS and DI water. The fluorescent antibody Alexa Fluor® 647 was chosen for its emission of purple red light (647 nm wavelength), which differentiates well from the photoresist autofluorescence of the microstructures that could be observed in the green range.

3.3 Sample Characterization

Samples were checked, imaged, and recorded at various stages of the fabrication process and live during experiments, either on glass substrates, Petri dishes, or inside of microfluidic channels that were described in section 3.1.

3.3.1 Optical Microscopy

During and after DLW-fabrication with the Nanoscribe, samples could be observed with an optical microscope that was integrated into the machine (Axio Observer.Z1, Carl Zeiss AG, Germany) with a digital camera (AxioCam ICc 1, Carl Zeiss AG, Germany). After development, after critical point drying, and after metal coating, samples were observed with a separate reflected light microscope (Axio Scope.A1, Carl Zeiss AG, Germany) and camera (AxioCam 105 color, Carl Zeiss AG, Germany). Functionalized, fluorescence-stained micromotor samples, as well as stained cells, were imaged with a "Cell Observer" microscope setup (Axio Observer.Z1 and AxioCam MRm with AxioVision software, Carl Zeiss AG, Germany). During various steps of cell culture experiments that will be discussed in section 3.4, and other experiments where cells were together with micromotors in a Petri dish or microfluidic channel, an inverted microscope (Axio Observer.A1, Carl Zeiss AG, Germany) and high-speed camera (Phantom Miro eX2 with camera control software PCC, Vision Research Inc., USA) were used to observe the samples. For sperm counting and motility analysis of *bovine* sperm samples (which will be discussed in section 3.4.1), a reflected light microscope (Axio Scope.A1, Carl Zeiss AG, Germany) with an area scan camera (avA1000-100gc, Basler AG, Germany) was utilized together with a specialized computer assisted sperm analysis (CASA) software (AndroVision®, Minitüb GmbH, Germany). Magnetic actuation of micromotors was observed and recorded with two different setups which will be discussed in detail in section 3.5. A reflected light Zeiss setup (Axio Scope.A1 and AxioCam HSm with AxioVision software, Carl Zeiss AG, Germany) and an inverted Nikon setup (Eclipse Ti2 microscope and DS-Qi2 camera with NIS-Elements software, Nikon Corp., Japan) were used.

3.3.2 Scanning Electron Microscopy

Scanning electron microscopy (SEM) images were taken after fabrication (without surface functionalization) of various samples with two microscopes (DSM 982 Gemini®, Carl Zeiss AG, Germany and CrossBeam NVision 40®, Carl Zeiss AG, Germany).

3.4 Cell Culture and Analysis

Bovine (cattle) and *murine* (mouse) gametes were cultured in accordance with established IVF routines. Assistance and training were provided by collaboration partners at the Institute of Farm Animal Genetics (Mariensee), the Leibniz Institute for Zoo and Wildlife Research (Berlin), and the Max Planck Institute of Molecular Cell Biology and Genetics (Dresden).

3.4.1 Sperm Cells

Bovine sperm samples were obtained in plastic straws frozen in liquid nitrogen from the local subsidiary of a cattle breeding company (Masterrind GmbH, Germany) in Meissen. Out of the Dewar vessel, a sample straw was thawed in a beaker with warm tap water (37°C) for 2 min, cut open and emptied into a centrifuge tube with 2 ml of modified Tyrode's solution, a specialized sperm cell medium (SpTALP) that was prepared beforehand from a base solution (SP-TL, Caisson Laboratories Inc., USA), supplemented with bovine serum albumin (BSA), sodium pyruvate, and gentamicin (gentamicin solution, Caisson Laboratories Inc., USA) to form Sperm-Tyrode's albumin lactate pyruvate solution (Sperm-TALP, i.e. SpTALP). The exact ratio of contents of 50 ml SpTALP are given in table 2.

Table 2: Sperm cell medium (SpTALP)

SP-TL	47.5 ml	Sodium pyruvate solution ¹	2.50 ml
BSA	300 mg	Gentamicin solution ²	100 µl

¹100 mM in sterile, double-distilled water

²500 mg gentamicin in 10.0 ml sterile, double-distilled water

Thawed sperm samples were cleaned by centrifugation for 8 min at 400x g and resuspended in 2 ml of SpTALP. For most experiments, including IVF, a more elaborate cleaning protocol based on a commercial kit (BoviPure™, Nidacon International AB, Sweden) was used. Therefore, thawed sperm straws were directly emptied into gradient mixtures of the cleaning solutions and centrifuged according to the kit instructions, before being resuspended in 2 ml of SpTALP.

3.4.2 Oocytes

Bovine ovaries were obtained from a local slaughterhouse in Altenburg (Südost Fleisch GmbH, Germany) and oocytes were isolated from them according to established

protocols [178]–[180] which will be described as follows. The ovaries were transported to the laboratory in a Dewar flask at 30°C in saline solution that is described in table 3.

Table 3: Transport saline solution

Sterile, double-distilled water	1.0 l	Penicillin G	0.66 g
Sodium chloride	9.0 g	Streptomycin sulfate	0.13 g

In the laboratory, the ovaries were sliced with a razor blade to extract cumulus-oocyte complexes (COCs) from the ovaries' follicles and collect them in a PBS-based solution (slicing solution) that is described in table 4, and warmed to 30°C as well. The slicing solution with COCs was distributed to several 15 ml centrifuge tubes and left to allow the cells to precipitate for 10 min at RT.

Table 4: Slicing solution

PBS ¹	1.00 l	D-glucose, hydrated	1.10 g
Sterile, double-distilled water	10.0 ml	Calcium chloride dihydrate	133 mg
Sodium pyruvate	36.0 mg	Penicillin G	60.0 mg
Streptomycin sulfate	47.4 mg		

¹5.0 PBS powder tablets dissolved in 1.0 l sterile, double-distilled water first, other components dissolved separately in 10 ml sterile, double-distilled water and added to PBS

Then, supernatants were removed and precipitates were collected and transferred to large Petri dishes where the COCs were collected individually with a glass pipette under the microscope and transferred to a Petri dish with buffered tissue culture medium (TCMair, based on commercial TCM199 from Sigma-Aldrich®, Merck KGaA, Germany) that is described in table 5 and was generally used when oocytes were handled in ambient conditions. However, COCs and oocytes in TCMair in Petri dishes (or microfluidic channel platforms) were preferably kept on a hot plate at 39°C when they were not in use under the microscope.

Table 5: TCMair, adjusted to pH 7.2 with 1 M sodium hydroxide solution

Sterile, double-distilled water	100 ml	Sodium pyruvate solution ²	2.20 ml
TCM199	1.47 g	Sodium bicarbonate	35.0 mg
Gentamicin sulfate solution ¹	100 µl	BSA (after pH adjustment)	100 mg

¹5.0 mg in 0.10 ml sterile, double-distilled water

²1.0 mg in 1.0 ml sterile, double-distilled water

Usually, 50 – 100 COCs were obtained from 15 – 30 *bovine* ovaries, which marked the start of one IVF cycle. The acquisition of *murine* oocytes will be described at the end of the following section.

3.4.3 In vitro Fertilization

Before *bovine* oocytes could be fertilized, their maturation was required. For *in vitro* maturation (IVM), a special IVM culture medium was prepared that is described in table 6. COCs were transferred from TCMair in groups of 20 to 100 µl drops of IVM medium which were placed onto a Petri dish, covered with silicone oil (to avoid evaporation), and incubated for 1 h at 39°C and 5 % CO₂ beforehand. Each group of COCs was passed through a series of three wash drops with a glass pipette before the transfer to the final IVM culture drops was completed. These wash drops also consisted of 100 µl IVM medium and were also incubated beforehand with silicone oil on top, although it should be noted that the final IVM culture drops were prepared from a modified version of the medium where 25 µl of Suigonan® solution (Intervet GmbH, Germany) were added to 975 µl of the IVM medium that is described in table 6.

Table 6: IVM culture medium, adjusted automatically to pH 7.4

Sterile, double-distilled water	100 ml	Sodium pyruvate solution ²	2.20 ml
TCM199	1.47 g	Sodium bicarbonate	220 mg
Gentamicin sulfate solution ¹	100 µl	BSA (after pH adjustment)	100 mg

¹5.0 mg in 0.10 ml sterile, double-distilled water

²1.0 mg in 1.0 ml sterile, double-distilled water

Ultimately, the COCs were incubated for 20 h at 39°C and 5 % CO₂ to complete maturation. Proper maturation of good quality COCs could be confirmed on the next day when the cumulus around the oocytes expanded noticeably while the dark main cell remained evenly colored and shaped. The initialization of IVM is termed "day -1", whereas the addition of sperm cells, i.e. the initialization of fertilization, marks "day 0" of the IVF cycle. Again, a special IVF culture medium was prepared that is described in table 7 – a modified Tyrode's solution similar to SpTALP, albeit with a different base solution that was buffered with (4-(2-hydroxyethyl)-1-piperazineethanesulfonic acid), i.e. HEPES (HEPES-TL, Caisson Laboratories Inc., USA). For the preparation of wash drops, 1 ml of albumin-pyruvate-gentamicin supplement were added to 9 ml of the described IVF medium, and 2 ml of the resulting medium were further mixed with 1 ml of hypotaurine-heparin-epinephrine supplement for the preparation of the final IVF

culture drops, again pre-incubated on Petri dishes as previously described. These supplements are described in table 8 and 9, respectively.

Table 7: IVF culture medium

HEPES-TL	50.0 ml	Penicillamine	0.14 mg
Sodium bicarbonate	96.6 mg	Sodium lactate solution ¹	22.2 ml
Phenol red	0.50 mg		

¹60 wt% in sterile, double-distilled water

Table 8: Albumin-pyruvate-gentamicin supplement

IVF culture medium (table 7)	20 ml	Gentamicin solution ¹	0.20 ml
BSA	1.2 g	Sodium pyruvate solution ²	0.14 ml

¹10 mg in 0.20 ml sterile, double-distilled water

²20 mg in 1.0 ml IVF culture medium (table 7)

Table 9: Hypotaurine-heparin-epinephrine supplement

Sterile, double-distilled water	26 ml	Epinephrine solution ²	4.0 ml
Hypotaurine solution ¹	10 ml	Heparin solution ³	4.0 ml ⁴

¹1.09 mg in 10.0 ml sterile, double-distilled water

²2.30 mg epinephrine in 50.0 ml sterile, double-distilled water supplemented with 165 mg sodium lactate and 50.0 mg sodium metabisulfite, adjusted to pH 4

³2.06 mg in 10.0 ml sterile, double-distilled water

⁴added after solution of previous components was filtered down to 8 ml

The matured COCs were washed and transferred to the final IVF culture drops again in groups of 20 per 100 μ l drop. For fertilization (conventional, i.e. without micromotors), healthy sperm cells were added in drops of ca. 10 μ l by pipetting (depending on the sperm count, checked under the microscope to obtain ca. 10^5 sperm cells per drop), collected directly after the last centrifugation step (without resuspension in SpTALP), following the sperm preparation protocol described in section 3.4.1. For IVF experiments with reduced numbers of sperm cells, the sperm precipitation was resuspended and further diluted in IVF culture medium (with all described supplements) and the IVF culture drop volume was decreased to 30 μ l to obtain sperm-to-COC-ratios of ca. 1000, 100, and 10 in the drops. After the addition of sperm cells, the IVF culture dishes were incubated for 19 h at 39°C and 5 % CO₂ again. Ultimately, on "day 1" COCs were denuded, i.e. the cumulus was removed and the fertilized oocytes (zygotes) were transferred to *in vitro* culture (IVC) medium, initializing the first stages of embryo development, i.e. cell division(s). IVC medium for wash drops (80 μ l each) and culture drops (30 μ l each) was prepared as described in

table 10, and 5 to 8 fertilized oocytes were placed into the IVC drops, respectively, after denuding and washing procedures. Denuding was achieved by collecting up to 60 COCs from the IVF drops in 0.5 ml TCMair in a centrifuge tube and shaking them with a vortexer at 1200 rpm for 5 min. Afterwards, the tube was emptied in a Petri dish, rinsed with more TCMair, and the denuded zygotes were recollected under the microscope and pipetted to the wash drops for the previously described washing and transfer procedure. In the IVC drops, zygotes were cultured up to day 5 after fertilization, incubated at 39°C and 5 % CO₂. Successful 2-cell, 4-cell, and 8-cell cleavage stages could be observed under the microscope starting from day 2, although more frequently on day 3.

Table 10: IVC medium for embryo development

Sterile, double-distilled water	49.9 ml	Sodium lactate solution ²	30.0 µl
Myo-inositol	25.0 mg	Sodium bicarbonate	105 mg
Gentamicin	2.50 mg	Phenol red	500 µg
Glutamine solution ¹	50.0 µl	Sodium pyruvate	4.00 mg
Sodium chloride	315 mg	Calcium chloride dihydrate	13.1 mg
Potassium chloride	26.7 mg	BME ³ amino acids solution	1.50 ml
Monopotassium phosphate	8.10 mg	MEM ⁴ amino acids solution	500 µl
Magnesium sulfate	9.10 mg	BSA	200 mg

¹0.2 mM in sterile, double-distilled water

²60 wt% in sterile, double-distilled water

^{3,4}Basal medium Eagle (BME) and Eagle's minimum essential medium (MEM) from Sigma-Aldrich® (Merck KGaA, Germany)

Murine oocytes were obtained from sacrificed mice from the Transgenic Core Facility (Max Planck Institute of Molecular Cell Biology and Genetics, Germany) in Dresden with help from Service Leader Ronald Naumann and fertilized with fresh *murine* sperm from the same facility. IVF and subsequent cell culture was conducted by Ronald Naumann and Franziska Hebenstreit (the in-house laboratory technician) according to established protocols [181], [182], and fertilized oocytes were incubated at 37°C and 5 % CO₂ in culture drops with KSOM mouse embryo medium (EmbryoMax® KSOM, Merck KGaA, Germany) until further experiments. The Transgenic Core Facility holds active permissions for the work with mouse embryos and works under the principles of the 3Rs [183] with animals living under specific pathogen free conditions. Cell culture and IVF experiments at the in-house laboratories did not require any further ethical approval, as the work with *bovine* and *murine* gametes did not provoke any legal issues in this framework. Fertilized embryos were not cultured for longer than five days in any case.

3.4.4 Hypoosmotic Swelling Test

Hypoosmotic swelling (HOS) was applied to immobilize sperm cells while monitoring their viability during sperm transport by micromotors, according to a test protocol that is well-established in ART [170], [184]–[186]. For that, 100 μ l of thawed, cleaned, and diluted sperm in SpTALP (as described in section 3.4.1.) were transferred to 1 ml of trisodium citrate dihydrate solution (prepared stock solution: 73.5 mg in 10 ml DI water, i.e. 100 mosmol/l) which was warmed to 37°C beforehand. The obtained HOS test sperm suspension was incubated for 1 h at 37°C and 5 % CO₂ before further use.

3.4.5 Cell Viability Assays

Viability of *bovine* sperm in three different conditions was investigated: thawed sperm in SpTALP, prepared as described in section 3.4.1, sperm in HOS test medium, as described in section 3.4.4, and sperm co-incubated with microhelices with different surface coatings and functionalizations, fabricated as described in sections 3.2.3 and 3.2.4. In all cases, 50 μ l of the respective sperm suspension were pipetted on a glass cover slip, and two fluorescent dyes from a commercial kit (LIVE/DEAD™ Sperm Viability Kit L-7011, Thermo Fisher Scientific Inc., USA) were added consecutively. The "live" staining – green fluorescent SYBR14 cyanine dye (SYBR® 14, Thermo Fisher Scientific Inc., USA) – was diluted 50 times before use, whereas the "dead" staining – red fluorescent propidium iodide (PI) – was collected directly from the kit. In the first case, 1 μ l of diluted SYBR14 was added to freshly prepared sperm in SpTALP and incubated for 10 min at 37°C in darkness, then 1 μ l of PI was added and the sample was again incubated for 10 min at 37°C in darkness. In the second case, the same was conducted with sperm in HOS test medium which had been treated as described in section 3.4.4. In the third case, sperm in HOS test medium were first co-incubated with different materials for 1 h at 37°C and 5 % CO₂, before they were transferred to the glass cover slip where the fluorescence stainings were added as described above. The different materials and conditions are listed in table 11. In order to co-incubate sperm and microhelices, the helices had to be removed from their respective fused silica substrate first by gentle scratching with a trimmed glass fiber, and suspended in a drop of HOS test medium which was pipetted on top of the respective helix array on the substrate beforehand. This helix suspension was then added to the 50 μ l sperm sample for co-incubation, with a final helix-to-sperm ratio of ca. 1 : 100. Moreover, an alternative staining to visualize the integrity of the sperm cells' acrosomes was applied to sperm after HOS treatment (prepared as in section 3.4.4). For that, fluorescein isothiocyanate-labeled peanut agglutinin (FITC-PNA) was added to sperm in HOS test

medium to a concentration of 25 $\mu\text{g/ml}$ to stain damaged acrosomes green, and LysoTracker blue fluorescent dye (LysoTracker[®] Blue DND-22, Thermo Fisher Scientific Inc., USA) was added to a concentration of 2.5 $\mu\text{g/ml}$ to stain intact acrosomes blue. Moreover, PI was applied to stain dead sperm red, as described above. The stained sperm sample was then incubated for 1 h at 37°C and 5 % CO₂ before evaluation.

Table 11: Co-incubation of sperm in 50 μl HOS test medium with different materials

Co-incubation materials	Comment
On a glass cover slip	Control sample
On a Ti-coated glass cover slip	Ti layer of 10 nm thickness
On a glass cover slip with Ni-coated helices	Helices as in section 3.2.3
With NiTi-coated helices	Helices as in section 3.2.3
With functionalized NiTi-coated helices	With pluronic funct. (section 3.2.4)
With NiTiAu-coated helices	Helices as in section 3.2.3
With functionalized NiTiAu-coated helices	With PEG-thiol funct. (section 3.2.4)

Ultimately, the cell viability of oocytes and zygotes was investigated after conventional IVF and micromotor-assisted IVF and ZIFT experiments. For that, 15 μl of fluorescein diacetate (FDA) solution (5 mg/ml in acetone) and 25 μl of PI were added to 5 ml of IVC medium (prepared as in table 10), and 50 μl drops of the obtained solution were placed on a plastic Petri dish. Oocytes and zygotes were pipetted individually or in small groups to the described drops and incubated for 3 min at RT in darkness. These stainings were applied typically on day 2 or 3 of the IVF cycle, and always at the same time in one cycle, i.e. conventionally fertilized oocytes and oocytes from micromotor-assisted sperm delivery experiments together, and conventionally cultured zygotes and zygotes from micromotor-assisted ZIFT experiments together at the same time, to obtain suitable control samples. All described fluorescence stainings of sperm, oocytes and zygotes were observed and recorded with the "Cell Observer" microscope setup (Axio Observer.Z1 and AxioCam MRm, Carl Zeiss AG, Germany).

3.5 Magnetic Actuation

Two different electromagnetic coil systems were used to actuate and control magnetic micropropellers with rotating magnetic fields (RMFs) which were homogeneously distributed within a sufficiently large focal volume to operate micromotors inside

microfluidic channel platforms under the microscope without any magnetic field gradients.

3.5.1 Modified Helmholtz Coil Setup

Magnetic microhelices were actuated with a modified Helmholtz coil setup that was custom-made in the in-house mechanical workshop to be mounted to an optical microscope (Axio Scope.A1, Carl Zeiss AG, Germany), allowing the microscope's objective to plunge into the magnetic field workspace from above and a custom-made micromanipulator sample holder from the side, as depicted in Fig. 3.3.

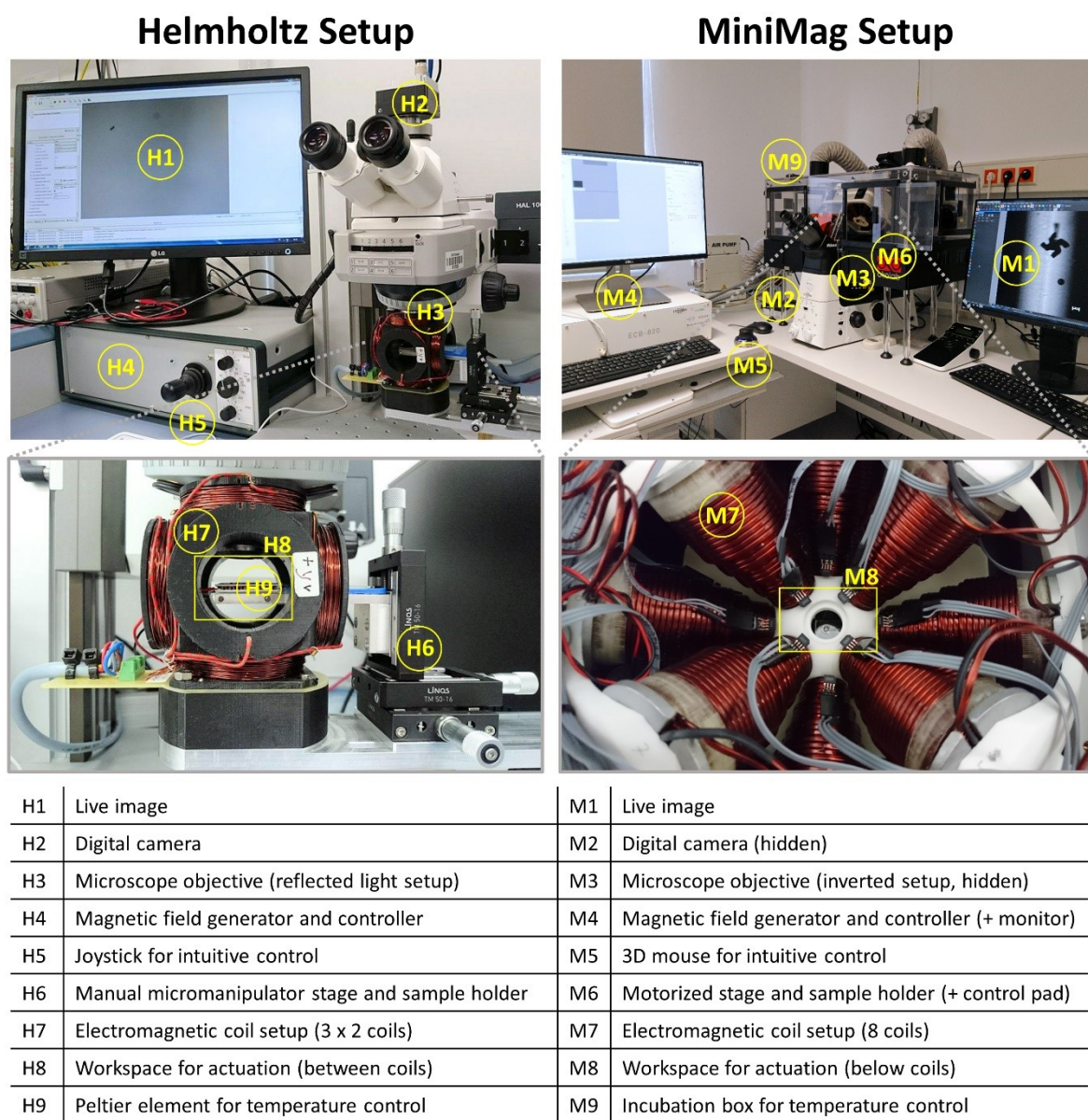


Figure 3.3: Two different setups for micromotor actuation with rotating magnetic fields and live observation and recording by optical microscopy.

These spatial restrictions required an alteration of the theoretical Helmholtz configuration of three parallel pairs of electromagnetic coils arranged orthogonal to each other – according to the definition that two identical coils of one of these pairs should have a distance from each other equal to their own radius (for optimal magnetic field homogeneity) – to a distance of twice their radius instead. In this way, micromotors in a microfluidic channel platform could be placed on the custom-made sample holder, moved and focused under the microscope, and actuated by the RMF generated by the electromagnetic coils, while being observed and recorded in real time with a digital camera (AxioCam HSm, Carl Zeiss AG, Germany). Microscopy videos were recorded with a framerate of 20 frames per second (fps) with appropriate microscopy software (AxioVision, Carl Zeiss AG, Germany) and analyzed with the open source image processing software package Fiji [187], containing the MTrackJ plugin (<https://imagescience.org/meijering/software/mtrackj/>) that was created by Erik Meijering. The electromagnetic coils were connected to a custom-made magnetic field generator that was programmed to generate an RMF with a magnetic flux density (B) of up to 3 mT in the focal volume (ca. 1 cm^3) between the coils. Rotation frequency (f) and B could be altered by analog control in the range of 0 – 100 Hz and 0 – 3 mT with two turning knobs. The spatial orientation of the RMF could be controlled with a joystick in x-y-plane and a turning knob to switch the orientation in z-plane progressively between -180° and 180° to steer rotating magnetic micropropellers such as helices. The designs of Helmholtz coil scaffold and sample holder were done by Mariana Medina-Sánchez (the group leader), and the entire system was manufactured and programmed by the in-house engineers Torsten Seidemann, Hartmut Siegel, and Uwe Biscop to allow intuitive, manual operation.

3.5.2 MiniMag Setup

Large, up-scaled helices and spiral-type micromotors were actuated with the so-called MiniMag system (magnetic field generator MFG-100-i, Magnebotix AG, Switzerland), a commercial setup of eight electromagnetic coils arranged in one plane, pointed at a focal volume that is freely accessible to place and observe samples (Fig. 3.3). The MiniMag was mounted upside down onto an inverted microscope (Eclipse Ti2, Nikon Corp., Japan) so that micromotors in a microfluidic channel platform could be placed into a custom-made sample frame that was inserted into the microscope's motorized stage. A complementary microscope camera (DS-Qi2, Nikon Corp., Japan) and imaging software (NIS-Elements, Nikon Corp., Japan) was utilized for real-time observation and video recording (10 fps) of micromotors. Videos were analyzed as described in the previous section. The RMF generated by the MiniMag was controlled with the

corresponding graphical user interface (Daedalus, Magnebotix AG, Switzerland). Field parameters f and B were altered in the range of 0 – 100 Hz and 0 – 20 mT, respectively. Frequency values could also be set negative to apply counterclockwise rotation. The spatial orientation of the RMF was defined by three angular parameters named "roll", "pitch", and "yaw" to control the field's orientation in relation to the x-, y-, and z-axis of a 3D coordinate system, respectively. These parameters could be changed in the graphical user interface or with a connected 3D mouse (SpaceMouse®, 3Dconnexion GmbH, Germany) to steer rotating magnetic micropropellers such as helices and spirals. A negative influence on micromotor performance and controllability owing to a possible disturbance of the magnetic field regarding the presence of the microscope objective in both setups could not be detected.

3.5.3 Experimental Procedure

In order to actuate and investigate the fabricated and prepared magnetic micropropellers (section 3.2), they had to be separated from their respective fused silica substrate and injected into a microfluidic channel platform (section 3.1) that could be fixed inside the working space of the Helmholtz coil or MiniMag setup under the microscope. Generally, a drop of the liquid medium for the respective experiment was pipetted onto an array of micromotors on the respective sample substrate and the micromotors were gently scratched with a trimmed glass fiber (microhelices) or 10 μ l pipette tip (large helices and spirals) to be separated from the substrate and suspended in the drop of medium. The obtained micromotor suspension was then pipetted to the respective microenvironment for the experiments that will be described in the following sections.

3.5.3.1 Micromotor Performance Evaluation

The propulsion performance of microhelices was investigated inside tailored parafilm channels (section 3.1.1) in DI water at RT, SpTALP at RT, and SpTALP at 38°C. TiNiTi-coated helices (table 1) with 3 and 4 windings, functionalized with pluronic solution (section 3.2.4), were actuated in the Helmholtz coil setup and steered to swim along rectangular tracks, observed live with 20x magnification and recorded with 20 fps. Tracks of each helix were recorded at different actuation frequencies, with increasing f from 0 – 100 Hz in steps of 10 Hz. Temperature control was established with a Peltier element that was mounted onto the sample holder, with the respective parafilm channel fixed on top of it (Fig. 3.3). The micromotor velocity tracking was conducted with Fiji (section 3.5.1) with the recorded video files. The propulsion performance of

large helices and spirals was evaluated by tracking the micromotors as they were traveling through parafilm or PDMS microchannels and tubular channels (section 3.1), actuated by the MiniMag setup and recorded at 10x magnification with 10 fps. Large helices were investigated in TCMair and oviduct fluid (OVF) at 38°C, spiral-type micromotors in TCMair and methyl cellulose-containing medium (MCM), a modification of SpTALP with 0.6 wt% methyl cellulose, dissolved overnight on a platform shaker. OVF was squeezed out from freshly isolated *bovine* oviducts (Südost Fleisch GmbH, Germany) by scraping the backside of a scalpel along the ducts. OVF was collected from several oviducts and centrifuged once for 10 min at 3000x g to remove tissue and cell debris from the fluid. MCM was designed to match the viscosity of OVF, which was measured with a shear rheometer (Paar Physica UDS 200, Anton Paar GmbH, Austria). The measured viscosities of OVF and MCM were in the range of 20 – 25 mPa·s, well comparable to what has been reported in the literature for 0.6 wt% methyl cellulose in DI water [188].

3.5.3.2 Cell Transport Experiments

In order to capture and transport sperm cells with microhelices, helices in a drop of SpTALP medium (after detachment from their substrate) were mixed with a drop of sperm in SpTALP (section 3.4.1) or HOS test medium (section 3.4.4) and injected into a parafilm channel. For micromotor-assisted fertilization experiments, oocytes in IVF culture medium (section 3.4.3) were added individually from the opposite inlet of the respective parafilm channel with a glass pipette. A Peltier element was used to keep the sample temperature at 39°C during the experiments under the Helmholtz coil setup microscope as described in the previous section. Analogously, large helices or spirals and *bovine* zygotes in TCMair, and spirals and *murine* zygotes in M2 (mouse embryo medium, equivalent to TCMair for *murine* zygotes, Merck KGaA, Germany) were added to PDMS microchannels from separate inlets. Moreover, large helices and *bovine* zygotes in OVF, and spirals and *murine* zygotes in M2 with 0.6 wt% methyl cellulose were investigated. These micromotor-assisted ZIFT experiments were conducted in the MiniMag setup. The applied microscope (section 3.5.2) was encased in a custom-made acrylic glass box to enable temperature control of the entire setup with warm air (39°C for *bovine*, 37°C for *murine* cells to emulate the respective animal's body temperature in its reproductive tract). Microparticles based on polystyrene (PS) (dark red, Merck KGaA, Germany) with a diameter of 100 µm were also used as zygote dummies for further experiments with spiral-type micromotors.

3.5.3.3 Cell Transfer Experiments

Spirals in M2 were filled individually into trimmed 10 μ l pipette tips (section 3.1.3) by attaching a larger (100 μ l) pipette to a trimmed 10 μ l tip and sucking up medium with one suspended spiral into the trimmed tip. Subsequently, the large tip was removed and *murine* zygotes were pipetted individually into the 10 μ l tip (from the wider open end) with M2. Spirals that captured *murine* zygotes (or PS particles) were transferred to PDMS microchannels by pipetting (again attaching the trimmed tip to a 100 μ l tip). Analogously, such cargo-loaded spirals were transferred from PDMS channels to Petri dishes, pipetting them into culture drops of KSOM mouse embryo medium that were prepared on the dishes beforehand (section 3.4.3).

4 Micromotor-assisted Sperm Delivery

As a first step towards a potential treatment of a severe case of male factor infertility, complete asthenozoospermia, a micromotor was designed and applied that can couple to an individual, immotile sperm cell and restore its motility via magnetic actuation. The results of this novel approach to assisted reproduction are presented and discussed in this section regarding its potential to provide a viable alternative to conventional ICSI owing to perspective *in vivo* application. Key results and discussions have been published and adapted with permission from [15]. Copyright © 2015 American Chemical Society.

4.1 Micromotor Design and Fabrication

The proposed micromotor was designed to accomplish two principal tasks: to move in a liquid medium under the control of an external magnetic field and to couple to a sperm cell in a reversible manner to transport it to a target (i.e. the oocyte). The helix structure was chosen regarding its established rotary motion dynamics, inspired by the bacterial flagellum, as described in detail in the Fundamentals (section 2.3). Its major advantages are the fairly simple actuation by an external RMF which can be controlled precisely and intuitively, and the possibility to fabricate it by photolithography in a batch process, as has been demonstrated before elsewhere [108]. Besides rotary propulsion, the helix can also accomplish the task of coupling to a sperm cell: As will be demonstrated, a microhelix can wrap itself around the tail of an immotile sperm cell, sufficiently large to envelope the tail in its lumen and sufficiently small not to allow the sperm head to slip into it as well, so that the sperm as a whole can be moved forward together with the rotating helix that is pushing against the sperm head, acting as a propeller (Fig. 4.1 A). This coupling mechanism also entails the capability to release the sperm cell by reversion of the direction of rotation of the helix, making the helix propel away from the sperm head and withdraw from the enveloped sperm tail. In this way, sperm coupling, transport and release can be achieved by a single helical microstructure, actuated by an external RMF, for micromotor-assisted delivery of immotile sperm cells to the oocyte, which will be demonstrated and discussed in the following sections. The final micromotor morphology and dimensions that were settled for (after several optimization steps) are depicted in Fig. 4.1 B. Besides writing and optimization of the program for DLW regarding laser power, scan speed, and line number (section 3.2.1.1 and Appendix) –

which was necessary to obtain stable microstructures – also the helix pitch and number of windings were altered regarding swimming performance, which will be discussed in the following section. In order to make the microhelices susceptible to external magnetic actuation, a multilayer coating of Ni and Ti was applied, as described in section 3.2.3. The helix (and ring) diameter was fixed by the necessity to couple to *bovine* sperm cells which feature a head diameter of ca. 5 μm [158] (Fig. 4.1 B).

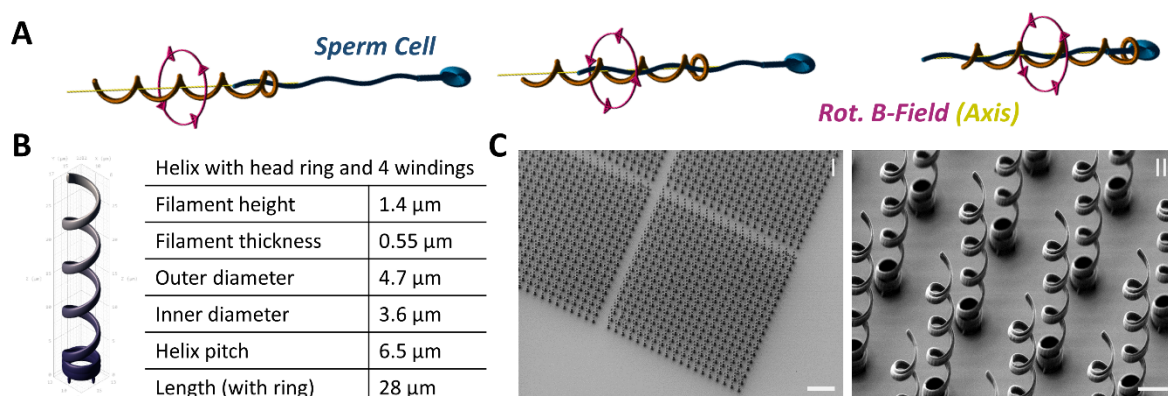


Figure 4.1: Helical micromotor design; A) principle of sperm capture; B) programmed design and dimensions of spermbot microhelix; C) SEM images of arrays (I) and individual (II) microhelices on a fused silica substrate (scale bars 50 and 5 μm , respectively).

Helices were fabricated in large arrays of hundreds and thousands of microstructures on one fused silica substrate and scratched off manually to be suspended in the respective liquid medium for subsequent experiments, as described in section 3.5.3. Fig. 4.1. C displays parts of such arrays and the uniformity of individual helices, although this was partially compromised by the crude scratching procedure which in turn justified the large number of microstructures on one sample. The small posts at the base of the head ring in the final design (Fig. 4.1 A) served to facilitate the release from the fused silica substrate by more cautious scratching to avoid cutting off the head ring in the process. The helix filament height and thickness were minimized, albeit not to the resolution limit of the Nanoscribe, as structural stability had to be ensured. The resulting filament height was larger than its thickness because of the aspect ratio of each polymerized voxel that was addressed by the Nanoscribe laser, i.e. the 2PA absorption cross section, as described in the Fundamentals (section 2.4). Both ring and tail of a helix were written by the laser with five lines each to ensure structural stability by thorough 2PP of the polymer photoresist. Ferromagnetic properties were obtained by multilayer metal coatings – most importantly Ni – as described in section 3.2.3, inspired by [108]. Microhelices were not magnetized before the experiments, i.e.

they possessed no remanent magnetic moment other than that which was induced by the external RMF during actuation.

4.2 Actuation and Propulsion Performance

The propulsion mechanism of a magnetic helix in a RMF was introduced in the Fundamentals (section 2.3.), especially considering the capability of the helix to follow the rotation frequency f of the externally applied field, which depends on the magnetic flux density of the field and the maximum magnetic polarization of the helix. The helices in this work exhibit the general frequency-velocity-dependency with step-out frequency as reported in the discussed literature [96], [100], [112]. Tumbling, wobbling, rolling, and proper corkscrew propulsion was observed, depending on f , which was generally kept in the range of 0 – 100 Hz. The frequency-velocity-profile (FVP) of an individual helix in a given liquid medium was obtained from recordings of the respective helix swimming rectangular tracks at different RMF frequencies in steps of 10 Hz. One example of such a rectangular track is depicted in Fig. 4.2 A, illustrating straight-lined propulsion with no side drift, as well as smooth steerability (here: $f = 50$ Hz). Side drift, i.e. a sideways rolling component of motion, was observed when a helix was swimming too close to the substrate, especially at a reduced f . Owing to the gravitational pull on the microswimmers, a slight z-axis tilt of the external RMF was necessary to make the helices swim upwards marginally when moving forward, to avoid contact with the substrate.

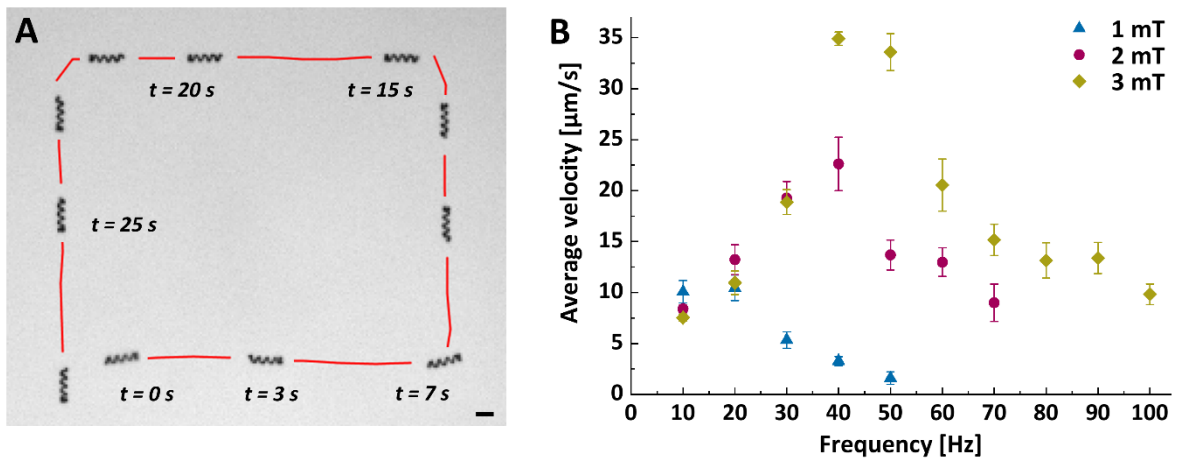


Figure 4.2: Basic helix propulsion experiments; A) rectangular track example for velocity evaluations at different actuation frequencies (here: $f = 50$ Hz, scale bar $10 \mu\text{m}$); B) FVP example for different magnetic flux densities ($B = 1 - 3$ mT) of a helix with 3 windings in DI water (error bars correspond to variations between different velocity measurements along a track at a given actuation frequency).

Without drift, intuitive and immediate real-time steering of the helices was possible under the microscope, as there was no noticeable time lag between the manual alteration of the RMF orientation (via joystick) and the realignment of the actuated helices. The FVP of a helix actuated with varying f is depicted in Fig. 4.2 B, illustrating the significant dependency of the swimming performance on the magnetic flux density B . When the flux density of the RMF was increased, greater velocities could be reached owing to a stronger magnetic polarization of the helix which allows it to follow the rotation of the external field with less loss and up to a higher step-out frequency. The displayed example corresponds to a helix with similar dimensions as presented in Fig. 4.1. Aside from setting B to the maximum of 3 mT in further experiments, optimization of the helix geometry was the second step to improve propulsion performance. Variation of the microswimmer geometry and dimensions were of course restricted by the precondition that the helix had to be able to capture and transport a *bovine* sperm cell, as described in the previous section. As the diameter of the helix had to be marginally smaller than a *bovine* sperm head and was thus held constant at ca. 4 μm , only the length of the helix could be altered, by changing the helix pitch length or the number of windings. The helix head rings were kept simple and slender to avoid unfavorable hydrodynamic drag. In general, as this work was mainly focused on the novel application of microhelices for assisted reproduction and not primarily on optimal propulsion performance, the basic helix structure was kept close to how it was established in the literature [108]. The helix pitch was altered marginally in the range of 5.5 – 7.5 μm , whereupon no significant difference from the ultimately chosen value of 6.5 μm could be confirmed, regarding the recorded FVPs. However, a difference between helices with 3 or 4 windings with constant pitch could be detected and is indicated in Fig. 4.3 A. The FVPs of several different helices suggest that helices with 4 windings reach greater average maximum velocities than helices with 3 windings. In the Fundamentals (section 2.3), it was concluded that the number of windings, i.e. the length of the helix, should not influence the final corkscrew propulsion velocity when helix diameter, pitch, and rotation frequency are fixed. However, this assumption cannot hold when the rotation is externally induced – as in the present case – with the helix following the rotation of the external RMF via magnetic interactions, depending on magnetic susceptibility and polarization. Apparently, microhelices with 4 windings are magnetized by the RMF more efficiently and thus can follow the field up to higher step-out frequencies than helices with 3 windings. Consequently, they can reach greater maximum velocities, which is documented in Fig. 4.3 A by the right-shift of the green shading that marks the range of step-out frequencies of helices with 4 windings approximately, as compared with the orange shading which corresponds to helices with 3 windings. For application as transporters for *bovine* immotile sperm, the

magnetic microhelices had to be applied in sperm cell medium (SpTALP) at 38°C. As indicated in Fig. 4.3 B that comprises data from literature [189] and in-house rheometer measurements, the viscosity of DI water and SpTALP is marginally different from each other, as well as temperature-dependent. These differences also influence the performance of helical micromotors in the respective conditions, as presented in Fig. 4.3 C and D (again for helices with 3 and 4 windings, respectively).

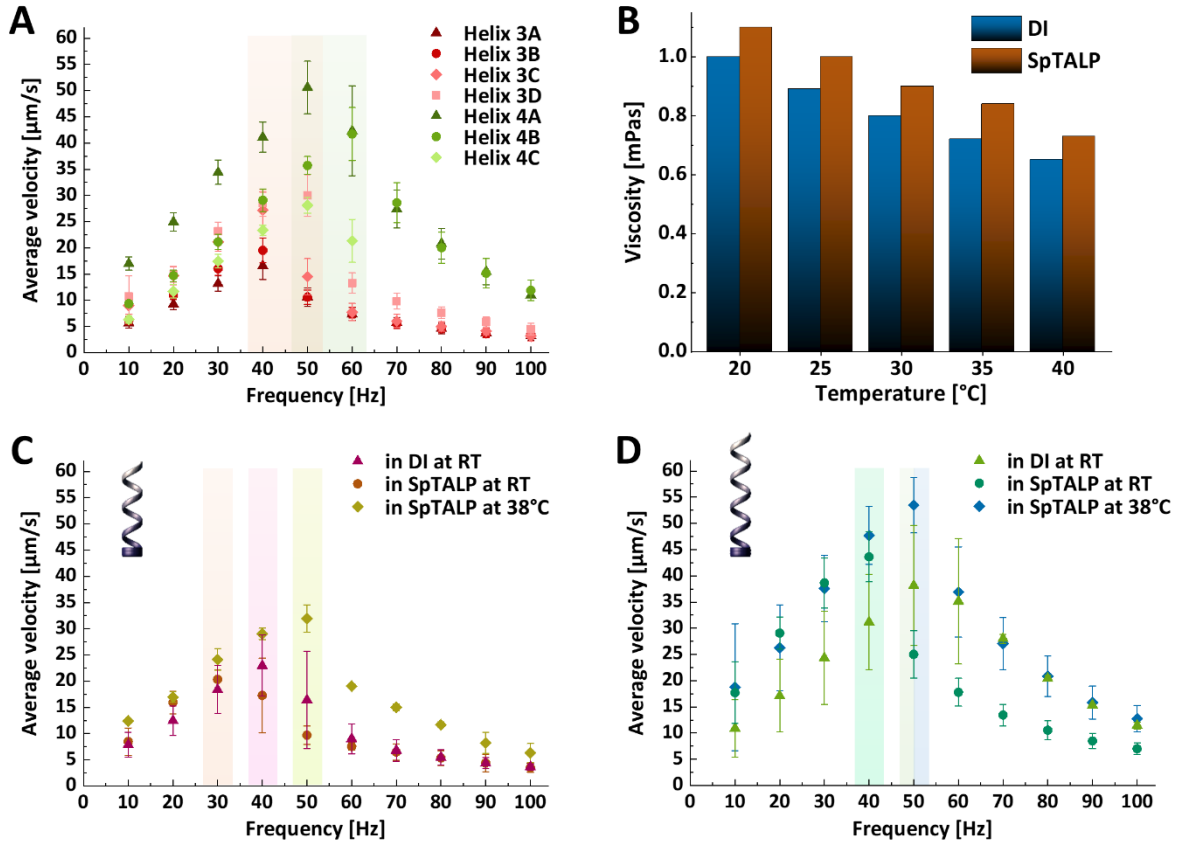


Figure 4.3: Helical micromotor performance; A) FVPs of helices with 3 or 4 windings in DI water; B) viscosity difference of DI water and SpTALP at different temperatures; C) FVPs of helices with 3 windings in different liquid media and at different temperatures; D) FVPs of helices with 4 windings in different liquid media and at different temperatures (error bars correspond to variations between different velocity measurements in A and different individual helices in C and D, color shadings indicate the step-out frequency range of a corresponding data line).

The graphs reflect the discussed advantage of 4 windings (Fig. 4.3 D) over 3 (Fig. 4.3 C) in terms of average maximum velocity. Moreover, both graphs indicate that when the liquid medium is changed from DI water to SpTALP (both at RT), the step-out frequency decreases, i.e. it becomes harder for helices to follow the external RMF because of the higher viscosity of SpTALP, compared with DI water (again marked by corresponding color shadings in Fig. 4.3 C and D, respectively). However, this is not the case in SpTALP at 38°C. Both with 3 and 4 windings, helices reach greater

velocities than in DI water at RT. This can be explained with the temperature-dependence of the viscosity, as plotted in Fig. 4.3 B. At 38°C, the viscosity of SpTALP is lower than that of DI water at RT (20 – 25°C), therefore helices can follow higher RMF frequencies and reach greater velocities. The relatively large error margin, especially in Fig. 4.3 D, reflects the performance differences between individual helices. This is mainly a consequence of the scratching procedure that was applied to release the microhelices from the fused silica substrate after fabrication (as described in section 3.5.3), which can damage and deform individual helices and thus deteriorate their uniformity. As discussed in the Fundamentals (section 2.3), the microswimmers' shape is one of the main factors that determine their propulsion performance, as slight morphology differences between individual helices can lead to different hydrodynamic behavior regarding corkscrew propulsion, e.g. different step-out frequencies. This influence was also observed when dust particles in the liquid medium adhered to micromotors, depending on their size and shape. Interestingly, it has been proposed and demonstrated by others that different step-out frequencies owing to marginally different morphologies of magnetic micromotors can be exploited to actuate and control them independently with one and the same externally applied magnetic field, simply by altering f [112], [190]. In the present work, this strategy was not pursued, as the aim was to manipulate only one single immotile sperm cell and guide it to the oocyte, although in the future it could be desirable to control a squad of spermbots to take advantage of cooperative sperm behavior, for example the release of hyaluronidase to facilitate cumulus penetration, as introduced in the Fundamentals (section 2.5.4). In general, the propulsion performance of the presented helical micromotors proved to be satisfying in terms of controllability and average velocity, with excellent steerability in all three dimensions and maximum velocities of ca. 50 $\mu\text{m/s}$ which corresponds to ca. 2 blps and compares well to similar synthetic helical swimmers in the literature [108], [109], [117], [118], as well as to human sperm cells (up to ca. 70 $\mu\text{m/s}$ [120]), which they intend to support in the case of asthenozoospermia. Experiments that demonstrate the capture, transport, and delivery of immotile sperm cells with the presented magnetic microhelices will be demonstrated and discussed in the following sections.

4.3 Capture, Transport, and Release of Sperm

Immotile *bovine* sperm cells were captured by magnetic microhelices under the microscope according to the principle presented in section 4.1. One example of the capture of an individual sperm is depicted in Fig. 4.4. As the head of this particular

sperm cell stuck to the underlying glass surface, the reversibility of the capture mechanism could be demonstrated without moving out of the same field of view under the microscope. However, different focus steps were necessary to visualize the thin sperm tail in phase contrast mode for threading it in successfully by the helical micromotor.

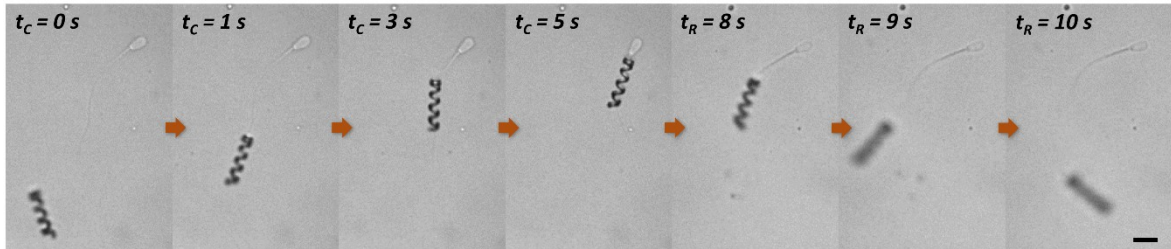


Figure 4.4: Capture (time lapse t_c) and release (time lapse t_R) of a *bovine* sperm cell in SpTALP which adhered to the glass substrate of the parafilm channel (scale bar 10 μm).

The spatial manipulation and transport of a free, immotile sperm cell after successful capture is depicted in Fig. 4.5. Fig. 4.5 A displays the sperm capture and starting point of a clockwise transport track that is continued in the panels B, C, and D, while Fig. 4.5 E displays the long-range transport towards an oocyte in two panels at lower (10x) magnification. Similar capture and transport experiments were conducted with several different sperm cells in tailored parafilm channels that were fabricated as described in the section 3.1.1.

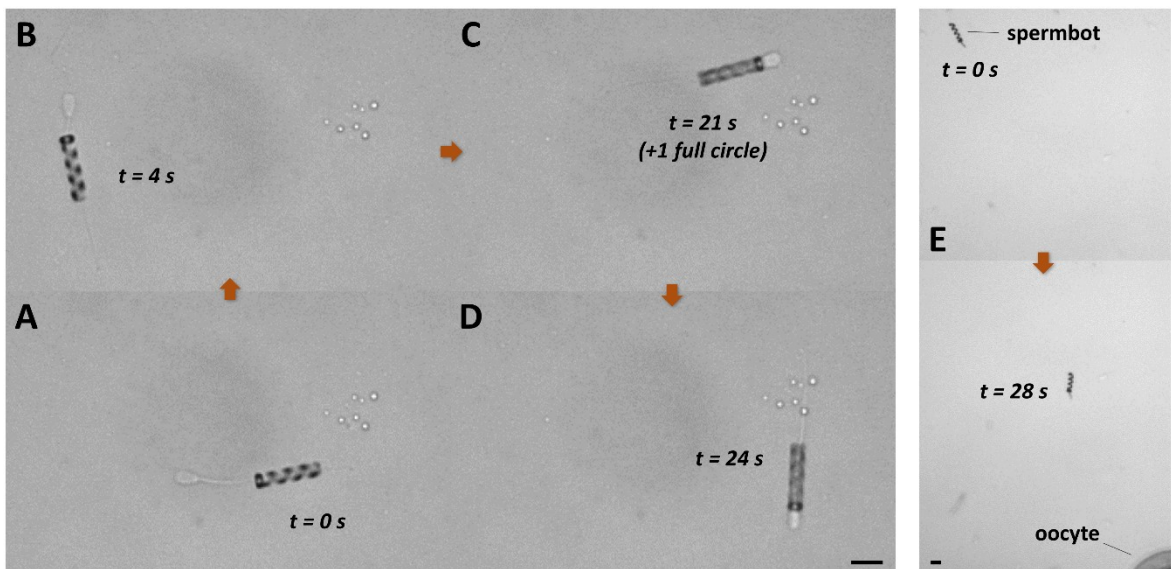


Figure 4.5: Transport of a captured *bovine* sperm cell in SpTALP in a parafilm channel; A) capture; B) – D) transport along a counterclockwise, rectangular track (time lapse t , 20x magnification); E) transport towards an oocyte (time lapse t , 10x magnification, all scale bars 10 μm).

The performance and controllability of the coupled spermbot was thereby not only dependent on the quality of the helical micromotor, as described in the previous section, but also on the quality of the coupling. Best performance was achieved when the sperm tail was accurately threaded into the helix lumen and thus the sperm loosely coupled to be pushed by the magnetically actuated helix at its neck. In other cases, for example when the tail was not enclosed by the helix completely or the sperm head was sticking to the helix by physisorption, severe obstructions of steerability and forward propulsion were observed. In such cases, reversibility, i.e. the release of the sperm cell by rotation reversal of the external RMF after successful transport, could not be achieved. However, also in optimal cases of sperm-to-helix coupling the velocity of the obtained spermbot decreased significantly compared with the free helix before coupling. This relation is documented in Fig. 4.6, displaying the average velocities of six spermbots – normalized to 1 before coupling – taking into account the variation between velocities of individual helices. A velocity decrease of approximately 50 % was recorded in SpTALP at 38°C (Fig. 4.6 B).

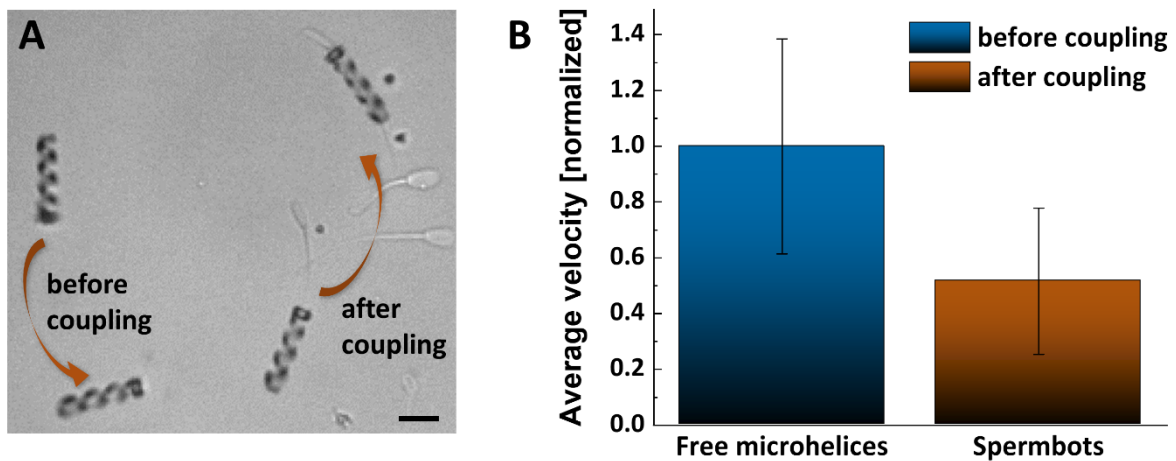


Figure 4.6: Propulsion performance of microhelices before and after sperm coupling; A) Example of one moving microhelix before and after sperm coupling (scale bar 10 μm); B) Average velocities of several microhelices before and after sperm coupling, normalized to their initial velocities (error bars correspond to variations between individual helices).

For tubular spermbots, where a motile sperm cell provides the propulsion force and carries a composite microtube, a velocity decrease of 20 – 80 % when comparing free and coupled sperm has been reported [13], [191]. Accordingly, the magnetic microhelix performs comparably with the additional load of an immotile sperm cell. With an average maximum velocity of the free helix of ca. 50 $\mu\text{m/s}$, as reported in the previous section, helical spermbots can still reach several tens of micrometers per second in SpTALP when actuated close to their respective step-out frequency by the RMF, which

is still sufficient to fulfill their task in a reasonable time frame, i.e. sperm delivery and potential fertilization, which will be discussed in the following section.

4.4 Delivery to the Oocyte

In a proof-of-concept *in vitro* setup, the capability to deliver captured immotile sperm cells to the oocyte for fertilization was verified. An example of the process is depicted in Fig. 4.7. In this experiment, sperm and oocyte were introduced into the same chamber of a parafilm microfluidic platform and the target sperm cell was captured in the immediate vicinity of the oocyte to be delivered in the same field of view of the microscope.

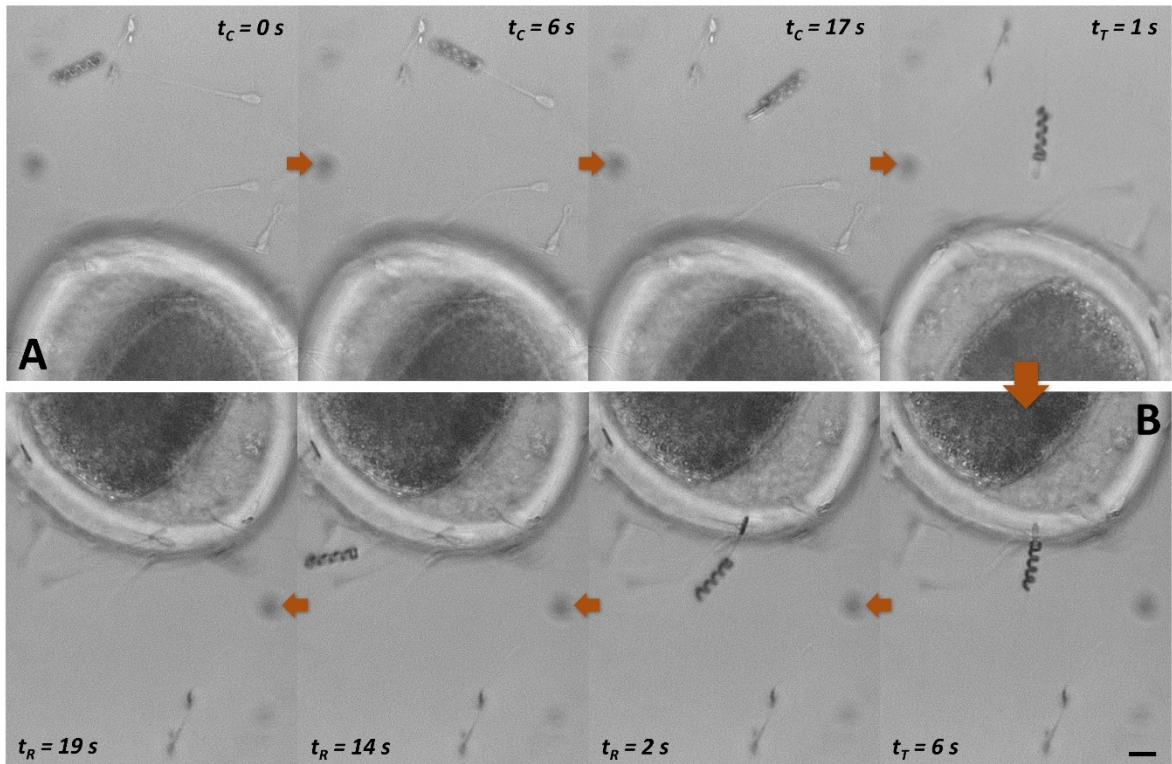


Figure 4.7: Delivery of an immotile *bovine* sperm cell to the oocyte; A) sperm capture (time lapse t_c) and oocyte approach (time lapse t_T); B) sperm delivery (mirrored panel orientation) to the oocyte's zona pellucida and withdrawal (time lapse t_R) of the microhelix (scale bar 10 μm).

This setup proved suitable to illustrate the steps of sperm capture, transport, as well as release after delivery, as displayed in Fig. 4.7, while it suffered from an inherent disadvantage: As there was no spatial separation between introduced sperm cells and the oocyte, it could not be verified whether the micromotor-delivered sperm was actually that which fertilized – if fertilization was achieved – as also other immotile

sperm cells could have attached to the oocyte in the process of pipetting when the microfluidic channel platform was filled, as can be observed in Fig. 4.7. To fix this problem, oocyte and sperm cells were introduced into opposite inlets of a parafilm channel with two main chambers that were connected by a narrow transit passage (as described in section 3.1.1). Additionally, the concentration of sperm cells in the medium was significantly reduced. In Fig. 4.5 in the previous section, an excerpt of a long-distance travel of a spermbot towards an oocyte in such a clean microchannel environment is displayed. However, this approach implicates the disadvantage of a longer sperm transport time period which compromises the viability of the oocyte, as the conditions in this *in vitro* setup were not ideal for the sensitive cells. The quality and viability of the oocytes and the relatively short time window for sperm delivery experiments in the discussed *in vitro* setup, which led to a limited number of successful deliveries (ten in total), were the main issues that impeded successful fertilization with micromotor-assisted immotile sperm cells in the present work. However, the ability of immotile sperm cells to fertilize an oocyte had to be verified, which will be discussed in the following section. Considering potential *in vivo* application, it is necessary to withdraw the helical micromotor after successful sperm delivery (and fertilization) not only from the sperm tail, but from the entire fallopian tube to avoid undesirable interference with the developing embryo. In principle, a microhelix that travelled successfully through the fallopian tube to deliver a coupled sperm cell should also be able to travel the same way back to the uterus by magnetic actuation once the sperm was released. However, as the fallopian tube is an extremely complex structure with many elastic folds, ciliated epithelial cells and sticky secretions as described in the Fundamentals (section 2.5.3), there is a risk that is not negligible that the micromotor becomes stuck on its way. For that reason, and for others which will be discussed in the following section, it is necessary to apply more than one spermbot in one treatment cycle, and also the biocompatibility of the synthetic micromotor becomes even more important. The present microhelices were coated with Ti which forms a passivation layer of titanium oxide that is corrosion-resistant and biocompatible, i.e. no significant inflammatory, cytotoxic or otherwise harmful effects are to be expected when exposed to the *in vivo* environment [192], [193]. Accordingly, when a microhelix becomes stuck and stays in the fallopian tube, it can remain harmless and ultimately be washed out by the flow of oviduct fluid towards the uterus where it can be retrieved more easily. However, this cannot be considered a satisfying solution and it would be far more preferable if the entire synthetic micromotor would be bioresorbable, i.e. made from materials that can be harmlessly degraded by body fluids within several hours or days. Bioresorbable (or biodegradable) helical micromotors – also fabricated by DLW – have been reported recently by others [79]–[81] and the technology could be in principle

transferred to the micromotors presented in this work, which is a step that remains to be taken in the future, as it was beyond the scope of the current work owing to the focus on other issues.

4.5 Sperm Viability and the Ability to Fertilize

The possibility to achieve fertilization with immotile sperm cells was discussed and placed in context in the Fundamentals (section 2.5.3). Nonetheless, a protocol to distinguish merely immotile from dead sperm in the present experiments was required. Staining with fluorophores – fluorescent dyes that bind to proteins such as antibodies or nucleic acids – is an established, diagnostically conclusive method to visualize cell viability or individual cellular compartments and their functionality. There are numerous fluorophores for numerous purposes, yet many of them suffer from one crucial disadvantage: they interfere with the natural function of the stained cell, especially its DNA [194], [195]. This is, of course, an issue in ART, as both gametes, sperm cell and oocyte, ought to remain intact and in their natural state – at least their DNA. Measures following preimplantation genetic diagnosis would be an exception to this proposition, yet also serve to illustrate the controversy over this issue. In state-of-the-art ICSI, the HOS test is used as a non-invasive alternative to determine sperm viability and membrane integrity, also suitable for immotile sperm [186], [196]. This method was adopted in this work, close to the original protocol [184] and applied as described in section 3.4.4., as it also entails the advantage of rendering subjected motile sperm cells immotile. As *bovine* sperm samples were obtained from random batches from a local cattle breeding company, it was more appropriate to render average or high quality samples immotile in this way, than to search for a particular low quality sample where most sperm cells would be already immotile. Regardless of their initial state, the HOS test renders sperm cells immotile as the surrounding liquid medium is taken up by the cells and makes their tails swell and curl in the process. However, this will only happen if the cell membrane is still intact and the cell is viable, which may or may not be the case for initially immotile sperm. The correlation of sperm viability and tail curling by HOS was verified in experiments where sperm samples that were subjected to HOS were also stained with two fluorophores from a commercially available sperm viability kit (section 3.4.5.) to mark live sperm cells green and dead sperm red. Fig. 4.8 A depicts a micrograph of one of these experiments. A good correlation between HOS and staining was observed, i.e. sperm cells that were confirmed viable by the green fluorophore also exhibited HOS behavior, whereas dead (red) sperm did not exhibit any tail curling. Therefore, it could be concluded that tail

curling as a consequence of HOS is a reliable indicator for sperm viability and only such sperm cells were captured and transported by magnetic microhelices in subsequent sperm delivery experiments. One example of a successful delivery of an immotile sperm cell that featured a curled tail in a liquid medium both suitable for HOS and oocyte culture (section 3.5.3.2) is depicted in Fig. 4.8 B.

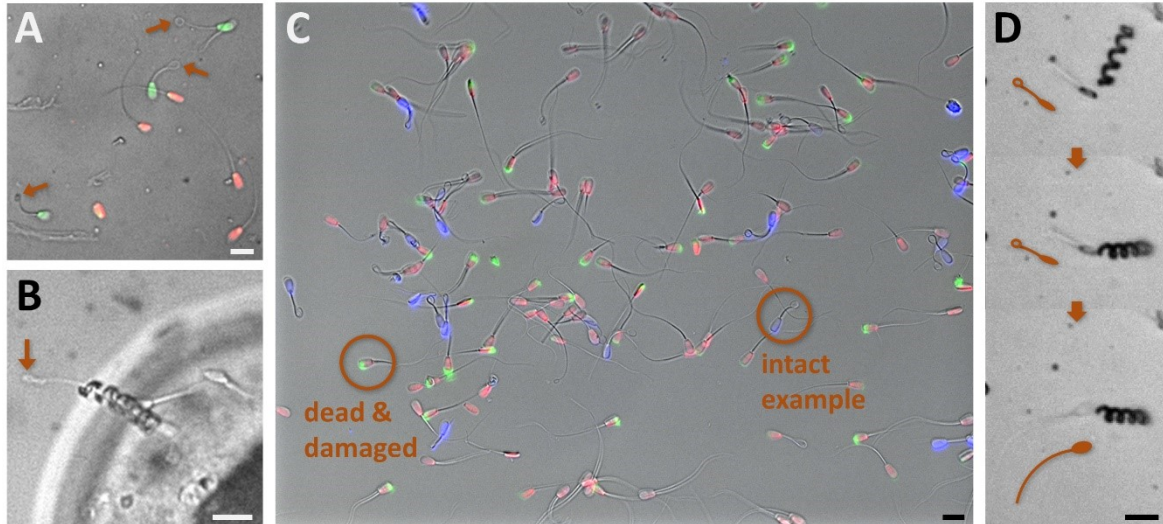


Figure 4.8: Sperm assessment; A) correlation of fluorescence staining of live (green) and dead (red) sperm and HOS (marked with arrows); B) delivery of an immotile sperm cell with intact HOS (marked with arrow) to an oocyte; C) correlation of fluorescence staining of intact (blue) and damaged (green) acrosomes with HOS (dead sperm also stained red); D) approach, contact, and piercing of a hypoosmotically swelled sperm cell which immediately uncurled in the process (all scale bars 10 μ m).

Besides sperm viability, another important precondition for successful fertilization is acrosome integrity. The role of the sperm acrosome in fertilization was already discussed in the Fundamentals (section 2.5.3). A different set of commercial fluorophores was used that marks intact acrosomes blue, damaged acrosomes green, and dead sperm cells red, as described in section 3.4.5. Again, the correlation between staining and HOS was verified. As illustrated in Fig. 4.8 C, again a good correlation between intact acrosomes (blue sperm) and curled tails because of HOS could be observed. Whereas not all dead (red) sperm cells also feature a damaged acrosome (green), almost all sperm cells with curled tail (indicates viability and membrane integrity) also feature blue staining which indicates an intact acrosome. Consequently, it could be concluded that the HOS test not only indicates viable sperm cells regardless of their motility, but also reveals functional acrosomes, i.e. picking up a sperm with curled tail can lead to successful fertilization. Ultimately, it is important to verify that the curled tail as an indicator for sperm viability holds true for the duration of sperm

transport, when the sperm cell is manipulated by the magnetic microhelix, as indicated in Fig. 4.8 B. This could be confirmed by the observation depicted in Fig. 4.8 D. In this sequence of three panels, it is displayed how a helix approaches a live sperm cell with swelled tail, contacts the sperm head, and pierces the sperm membrane with the sharp tip at the end of the helix filament. It was observed that within a fraction of a second, presumably in the moment when the membrane was pierced, the sperm tail uncurled to its original length. When the membrane integrity was lost, the osmotic pressure could no longer be sustained and the sperm's HOS behavior approximated that of a dead sperm. By implication, it can be concluded that while the tail remains curled, the sperm cell is intact and viable, as in the delivery case depicted in Fig. 4.8 B, while a damaged or dead sperm would immediately unswell as in the discussed case. Besides being dead from the start, an immotile sperm could die or lose its ability to fertilize during the micromotor-assisted transport experiment. This could happen because of the suboptimal cell culture conditions during the experiment under the microscope, where temperature control was established only to a certain degree with a Peltier element (section 3.5.3), and CO₂ control was not available. Aside from these issues, cell toxicity of the synthetic microstructure had to be ruled out, i.e. biocompatibility had to be verified. For that, *bovine* sperm cells were co-incubated with microhelices with different coatings (and functionalizations) for 1 h in SpTALP, respectively, and compared with two controls (sperm without helices in SpTALP on an uncoated glass substrate or on a Ti-coated substrate), with all sperm cells collected from the same sperm sample. The results of the live/dead counts after fluorescence staining of these samples are summarized in Fig. 4.9. Microscopy images of stained sperm cells that were also subjected to HOS before incubation are displayed in Fig. 4.9 A, without and with microhelices. The different helix samples were added to sperm in SpTALP in a helix-to-sperm ratio of not more than 1:100 in each case, which served well to reflect the general conditions during micromotor-assisted sperm transport experiments. As indicated in Fig. 4.9 B, NiTi-coated helices that were functionalized with pluronic solution (section 3.2.4) indicated no adverse effects on sperm viability compared with the two control samples without helices. Generally, functionalized helices performed marginally superior to non-functionalized ones. With pluronic- or PEG-thiol-functionalized helices, no adverse effects on sperm viability after 1 h of co-incubation were detected (Fig. 4.9 B). The cell-repellent, biological detergent pluronic solution which was used to avoid the sticking of sperm to the microhelices – as well as the hydrophobic PEG-thiol functionalization of Au-coated helices – apparently also improve the biocompatibility of the helices as they screen the metallic helix coatings, as observed in the comparison to non-functionalized NiTi- and NiTiAu-coated helices which perform marginally worse. However, also bare Ni-coated helices without

functionalization exhibited greater sperm viability than the other non-functionalized helices, which is surprising as the biocompatibility of Ti is known to be superior to Ni [192] and is also supported by the present data comparing the two control samples (uncoated and Ti-coated glass without microhelices), where the latter one performed better. Nonetheless, even though Ni might not be particularly harmful to sperm cells, the Ti-layer must remain to prevent corrosion and to avoid potential allergic reactions to Ni of the surrounding endothelium inside the patient's body [192].

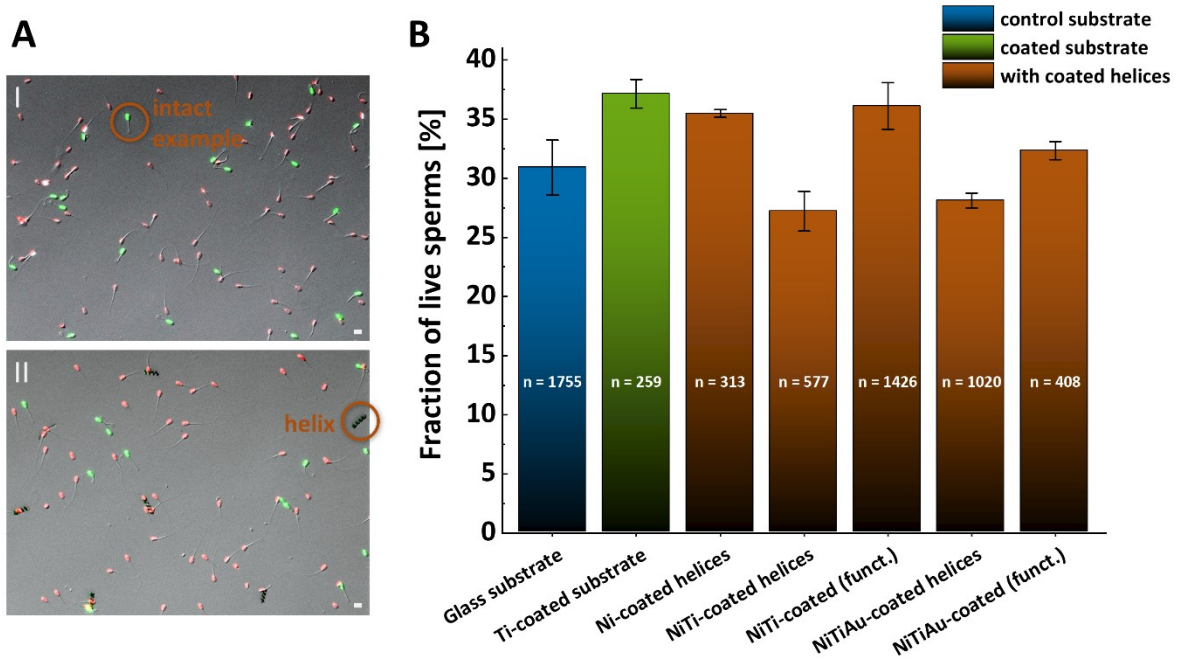


Figure 4.9: Sperm viability assay; A) Fluorescence staining of live (green) and dead (red) sperm cells after 1 h incubation without (I) and with (II) metal-coated microhelices in SpTALP on a glass substrate (scale bars 10 μ m); B) Evaluation of sperm viability results after 1 h incubation in different conditions (n = number of counted sperm cells, error bars correspond to variations between different field of view countings on one sample).

However, considering the overall low quality of the investigated sperm sample (approximately 30 – 40 % live sperm cells in both controls), the observed differences regarding the different helix coatings should not be overestimated, while the general non-toxicity of the investigated microhelices proved to be satisfying at this point. It must be noted that because of the externally applied magnetic guidance, the total number of spermbots, i.e. microhelices transporting immotile sperm in the case of asthenozoospermia, can be much reduced compared to the millions of sperm cells that are deployed in the natural case. Therefore, also the amount of synthetic material is strictly limited and can be ideally retrieved from the patient's uterus after successful sperm delivery by magnetic actuation. It is estimated that a squad of ca. 100

micromotors could be sufficient to ensure fertilization in the final *in vivo* application case. As it is known that sperm cells do not only depend on their motility, but also cooperate via biochemical cues (section 2.5.3), the sufficiency of only ca. 100 sperm cells at the fertilization site had to be verified. For that, conventional IVF was conducted with healthy *bovine* sperm with reduced numbers of sperm cells in the fertilization medium. As discussed in the Fundamentals (section 2.5.3), a multitude of sperm cells at the fertilization site cooperates to penetrate the cumulus around the oocyte, by whipping at the sticky cells with their tails and by secreting hyaluronidase which chemically cleaves the hyaluronan links between the cumulus cells [151], [168]. This cooperative attack is illustrated in Fig. 4.10 A, I in an *in vitro* setup. Moreover, a case of successful fertilization and a first stage of zygote cleavage are displayed in Fig. 4.10 A, II and III, respectively. Such results were routinely achieved in the laboratory by conventional IVF with *bovine* sperm and oocytes according to the protocol described in section 3.4.3. Frequently, success rates of approximately 40 % cleaved zygotes were observed in one IVF cycle, which is not too far away from the results in professional IVF laboratories [178], [197]. Fig. 4.10 B depicts the results of the two cycles that were carried out with drastically reduced numbers of sperm cells per oocyte to ca. 1000, 100, and only 10. Although the control samples that were fertilized with the usual amount of sperm exhibited a relatively low success rate of only 26.7 %, comparable success rates were still achieved with the reduced sperm counts, even 26.9 % with only approximately 10 sperm cells per oocyte. This experiment serves to prove that a relatively small number of sperm cells at the fertilization site can complete its mission, apparently providing sufficient physical and biochemical proficiency to penetrate the cumulus and zona pellucida of the oocyte. Nonetheless, in the case of asthenozoospermia, even if a squad of 100 spermbots could fulfill the biochemical preconditions to fertilize by the amount of sperm that are carried, the micromotors can only restore the sperm cells' impaired motility, but not their ability to whip away cumulus cells. As displayed in Fig. 4.10 C, a magnetically actuated microhelix quickly becomes stuck in the tough and sticky cumulus. For *in vitro* experiments as demonstrated in section 4.4, this may not be a problem as the cumulus can be removed from the oocytes in the laboratory beforehand, as described in section 3.4.3. However, in order to achieve micromotor-assisted fertilization in an *in vivo* setup, cumulus penetration is absolutely necessary. Conceptually, the functionalization of microhelices with hyaluronidase could aid in chemically cleaving and dividing the cumulus, additional to the hyaluronidase that the carried sperm cells secrete. It was observed in the laboratory that an increased concentration of hyaluronidase in the fertilization medium (added by pipetting) lead to complete disintegration of the cumulus oophorus during IVF experiments. The possibility to functionalize the

microhelices biochemically was demonstrated with a fluorescent antibody, displayed in Fig. 4.10 D. The functionalization, which could be visualized by fluorescence microscopy, was clearly distinguishable (Fig. 4.10 D, I) in comparison to the control helix (Fig. 4.10 D, II) which was treated with the same linker molecules (section 3.2.4) but without fluorescent antibody. The anisotropic distribution of antibodies on the functionalized helix was created intentionally and is demonstrated in detail in Fig. 4.10 E. Two helices were functionalized from head ring to tail, owing to an asymmetric distribution of SiO₂ which served as the mediator between helix surface and linker molecules for the antibodies.

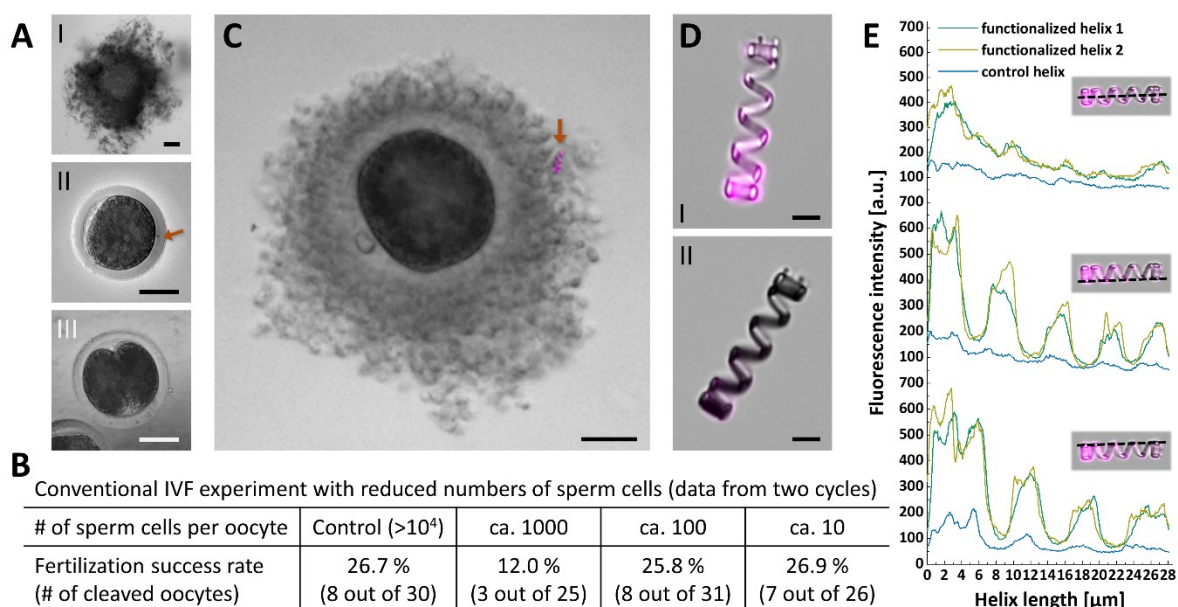


Figure 4.10: Penetrating the cumulus oophorus; A) steps of conventional IVF: a multitude of sperm cells is loosening up and penetrating the cumulus (I), one sperm (marked with arrow) achieves fertilization (II), the fertilized zygote cleaves (scale bars 50 μ m); B) verification of the possibility to achieve fertilization with a limited number of sperm cells (results of conventional IVF); C) a magnetic microhelix (fluorescing, marked with arrow) cannot penetrate the cumulus (scale bar 50 μ m); D) microhelices with (I) and without (II) anisotropic functionalization with a fluorescent marker (scale bars 5 μ m); E) fluorescence intensity profiles of two functionalized helices and one control, three different profile lines indicate the increased intensities at the respective helix head rings and where the helix windings overlap in the respective top views (dashed lines in the small insets indicate corresponding intensity measurements along the respective helix).

Different signals were obtained depending on the axis where the fluorescence intensity distribution was measured along the respective helix owing to the overlap of material at the rings and certain winding positions in the top view detection mode (Fig. 4.10 E). The replacement of the fluorescent marker with actual hyaluronidase is currently

under investigation, first results must be deferred to future work. Nonetheless, the present results represent the first steps towards functionalizing and enhancing a magnetically actuated micromotor that can capture, transport, and deliver immotile sperm cells. The successful adaption of the previously reported helical micropropeller to realize this novel application towards micromotor-assisted fertilization, *in vitro* and potentially *in vivo*, was demonstrated and implemented in this section 4. In section 5, a different case of micromotor-assisted delivery of cellular cargo will be presented – also applied in the field of ART – with a novel magnetic micropropeller design.

5 Micromotor-assisted Zygote Transfer

The motivation and purpose of the work presented in this section is the combination of the main advantage of ZIFT, i.e. cell culture and development of an *in vitro*-fertilized oocyte in its natural *in vivo* environment, with the non-invasive micromanipulation capability of a customized micromotor to achieve zygote transfer without surgery. Analogous to section 4, capture, transport, delivery, and release of cells by micromotors are demonstrated. Considering the different size and shape of the target cell (fertilized oocyte instead of immotile sperm cell), a novel microstructure was designed and applied for proof-of-concept experiments towards alternative, non-invasive, micromotor-assisted ZIFT. Especially the resilience of the cargo-to-micromotor-coupling when transferring the cargo-loaded micromotor between different environments will be confirmed and discussed, as well as the micromotor's performance in high-viscosity media and spatially confined channels. These and further steps towards *in vivo* applicability will be placed in context in the following sections. Key results and discussions have been published and adapted with permission from [157]. Creative Commons Attribution License © 2020 Wiley.

5.1 Micromotor Design and Fabrication

In principle, an oocyte can be manipulated by a magnetic microhelix similar to an immotile sperm cell as was demonstrated in section 4. The helix can be scaled up in size so that the ring at the head end is marginally smaller in diameter than an oocyte (50 – 150 μm in most mammals) to simply shove the cell forward, as will be demonstrated as follows with *bovine* oocytes and zygotes and up-scaled helices with 100 μm ring diameter, and is illustrated in Fig. 5.1 A. However, compared with the spermbot approach, there is one significant difference that compromises this concept for oocytes. In the case of a transported sperm cell, the cell body is shoved forward by the microhelix while the sperm tail is confined within the helix lumen. In the oocyte transport case there is no flagellum, hence the spherical cell cannot be geometrically trapped by the pushing helix and can easily become lost in the flow of the liquid medium, especially when the propelling helix changes its orientation or stops completely. To fix this issue, a novel micromotor design that incorporates a resilient cell trapping and release mechanism was conceived. In line with the already presented spermbot micromotor, the simple, controllable, and biocompatible actuation principle based on an RMF and the use of materials that are photopatternable by DLW were

retained. In the literature, reversible cargo capture and release by stimuli-responsive microstructures has been realized by using light [198], temperature [199], electric [50] or gradient magnetic fields [200], or assemblies of multiple components [64] to bind or encapsulate particles and cells. However, such complex mechanisms would be difficult to realize for potential *in vivo* applications, as for example (UV/visible/IR) light can hardly penetrate the skin, local heating can compromise cell viability, and sophisticated assemblies with hinges and joints are prone to sticking or buckling in the complex *in vivo* environment.

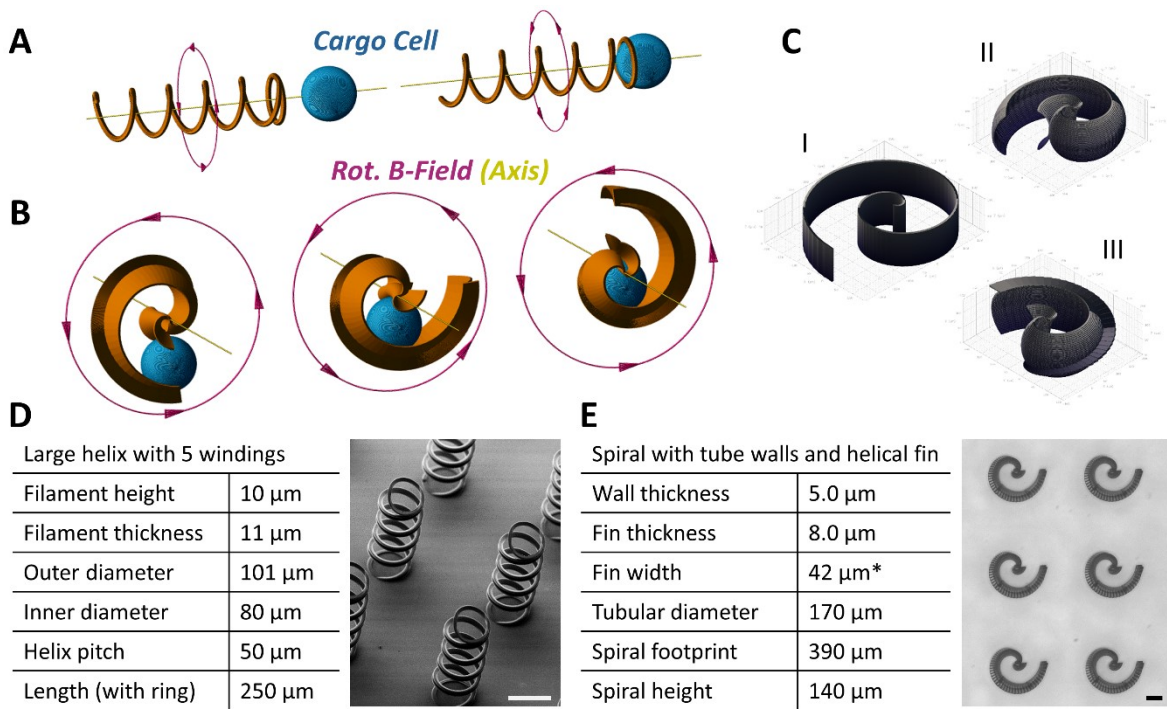


Figure 5.1: Micromotor designs for oocyte/zygote manipulation; A) cargo capture and transport with an up-scaled helix; B) cargo capture and transport with a spiral-type micromotor C) shape evolution from spiral layout (I) to tubular spiral (II), and with fin (III); D) dimensions of large helix for 100 – 150 μm diameter cargo spheres and SEM image of DLW-fabricated and coated helices; E) dimensions of spiral for 100 – 150 μm diameter cargo spheres, the tubular diameter defines the width of the spiral opening, the spiral footprint is the length of a spiral when lying flat on a substrate, as displayed in the microscopy image of DLW-fabricated and coated spirals (all scale bars 100 μm , *the fin width decreases along the spiral's backbone from opening to center).

Considering the specifically sensitive cargo in this work – early stage embryos – a geometrical trapping mechanism was conceived that is solely based on magnetically induced rotation, refraining from any other external triggers or material cues. Based on the concept of a sphere rolling along a spiral track, reaching a definite end point when going inwards while escaping it when going outwards, a spiral-shaped

micromotor was designed that can capture an oocyte by rotating its open end towards the cell to enclose it until it is trapped in the center point of the spiral, and release the confined cell by reversing the spiral rotation until the open end of the spiral sets the cell free again (Fig. 5.1 B). To realize this principle, the micromotor layout of an arithmetic spiral that suits the oocyte's diameter was extended with half-tubular walls to guide and confine the spherical cell inside the structure, as illustrated in Fig. 5.1 C, I and II. In the final design, the tubular spiral layout was shortened to span only over one winding (2π) and a helical fin was added at the backbone of the spiral to enhance hydrodynamic properties regarding forward motion when rotating (Fig. 5.1. C, III). As discussed in the Fundamentals (section 2.3), chirality, i.e. shape anisotropy, is important for efficient propulsion at the microscale. The swimming performance of the proposed spiral micromotors will be evaluated in the following section. Up-scaled helices and spirals were fabricated by DLW, analogous to microhelices, although coated with Fe as magnetic layer instead of Ni, as described in 3.2.3. Fabricated helices and spirals are depicted in Fig. 5.1 D and E, respectively, with dimensions suited to capture spherical cargo of 100 – 150 μm diameter, to match the size range of *bovine* oocytes and *zygotes*. Smaller spirals to capture *murine* oocytes and *zygotes* of 50 – 80 μm diameter were also fabricated with equal wall and fin thicknesses and all other dimensions scaled down uniformly with the tubular diameter (to 150, 130, and 110 μm) to preserve the shape (not displayed).

5.2 Actuation and Propulsion Performance

The forward propulsion of the described spiral micromotors in liquid medium differs from the discussed screw-propeller behavior of helices in several aspects. Both structures are actuated by an external RMF and move forward because of drag anisotropy arising from their chirality (Fundamentals, section 2.3), however, the spirals are rather rolling along the respective channel surface than swimming through the bulk fluid. As with the helices, different modes of motion can be observed, depending on the rotation frequency of the RMF and on its orientation and inclination in the workspace. When a spiral is lying flat on the channel surface as in Fig. 5.1 E and the RMF is rotating in the substrate plane, the spiral rotates in plane as well, following the field's direction of rotation, albeit with (almost) no net forward motion (Fig. 5.2 A). Tilting the orientation of the RMF by altering the parameters roll, pitch, and yaw (section 3.5.2) inclines the rotating spiral micromotor relative to the x-, y-, and z-axis, respectively, of a 3D coordinate system with x and y spanning the substrate plane and z pointing away from the center of gravity (of the earth). For example, a

stable mode of progression is achieved with roll = 90° and pitch = 0° , making the spiral stand up perpendicular to the channel surface and rotate in the x-z-plane, rolling forward in x-direction on the substrate (Fig. 5.2 B). Forward and backward rolling of spiral micromotors was observed, induced by clockwise or counterclockwise RMF rotation, respectively. The yaw parameter was utilized to steer the rolling micromotor, inclining its forward orientation to the left or right while rolling, which allowed intuitive and immediate directional control during live observations, as no significant time lag between RMF- and micromotor-reorientation was observed, similar to helical microswimmers (Fig. 5.3 A and B, in two different media). Intermediate pitch angles lead to less efficient forward propulsion. Depending on actuation frequency and field inclination, tumbling instead of rolling could be observed when the actuated spiral's rotation switched to a mode where its axis of rotation was no longer normal to its spiral footprint, similar to wobbling and tumbling of helical micromotors which was described in the Fundamentals (section 2.3).

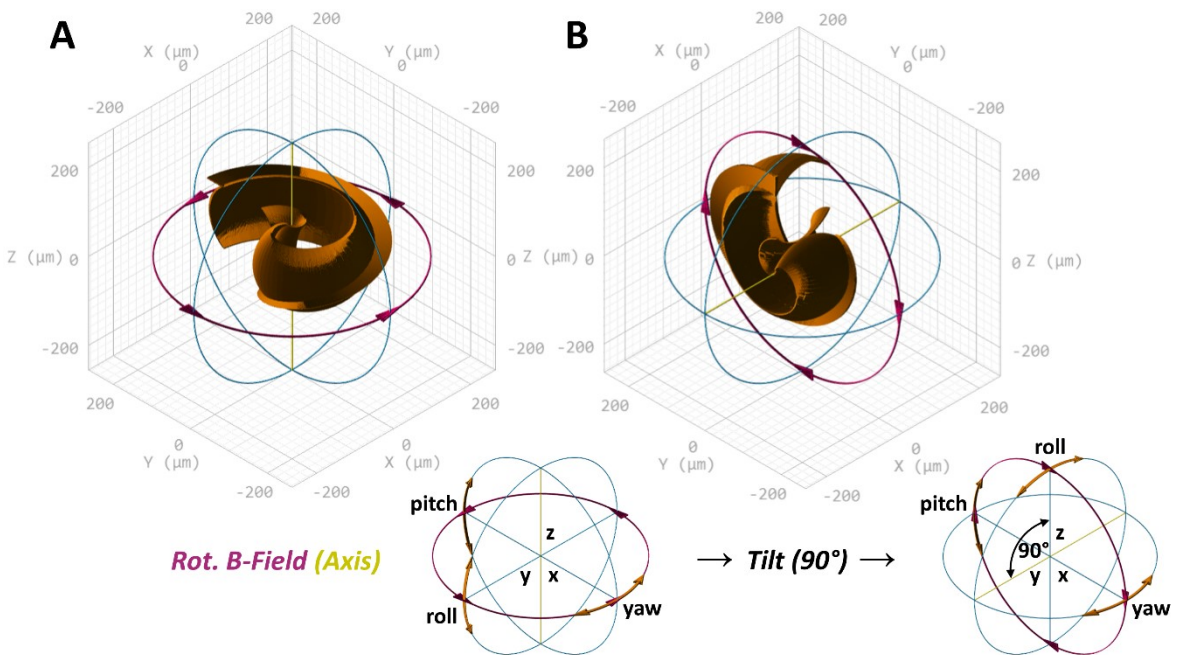


Figure 5.2: Orientation of a spiral-type micromotor relative to the magnetic field parameters roll, pitch, and yaw; A) in-plane rotation with roll = pitch = yaw = 0° ; B) forward propulsion with roll = 90° (purple circles with arrows denote the direction of rotation of the RMF, orange arrows denote possible inclinations with alterations of roll, pitch, and yaw, respectively).

Contrary to helices, spiral micromotors did not exhibit a defined step-out frequency above which the swimmer's velocity sharply decreased, yet their forward velocity reached a saturation point and plateau phase at higher frequencies, until they suddenly switched to a tumbling mode upon further increase of f . This behavior has

been reported for other magnetically actuated rolling-type micromotors recently as well [114]. As with helices, maximum rotation frequencies and corresponding maximum velocities proved to be strongly dependent on the viscosity of the liquid medium. In water-based media such as TCMair, spiral-type micromotors reached much greater average velocities than up-scaled helical micromotors at their respective maximum actuation frequency. Fig. 5.3 E displays a comparison of average maximum velocities of the spiral-type micromotors, the large, up-scaled helices with 100 μm diameter, and the spermbot microhelices of section 4. Blue columns denote absolute velocities in water-based media, red columns denote corresponding velocities in blps. Naturally, the large helices (Fig. 5.3 D) are faster than the microhelices in absolute values, however, not when normalized to their respective size. For the spirals, two sets of blue and red columns are depicted. With a footprint length of 390 μm , one spiral is so large that it escapes the field of view of the microscope quickly, even at only 10x magnification. The right blue column displays the average velocity of spirals at ca. 5 Hz, well below the maximum possible actuation frequency in water-based cell culture medium, where the swimming spirals could still be followed continuously with manual stage movements under the microscope. Here, the average velocity normalized to blps is comparable to both types of helices at ca. 2 blps, whereas the absolute average velocity is significantly greater than that of large helices which were designed for the same purpose of oocyte and zygote transport. However, the left blue column indicates that even greater velocities of more than 2000 $\mu\text{m/s}$ (ca. 5.5 blps) can be reached in TCMair when f is increased up to 25 Hz and higher. In this case, spirals were actuated and steered on circular paths to quickly propel in and out of the microscope's field of view (in the substrate plane) without moving the stage (Fig. 5.3 A displays an excerpt of this movement). Such great velocities are not practicable for most *in vitro* experiments, yet serve to illustrate the spiral's capability to outperform helical micromotors in terms of propulsion efficiency. Towards applicability as cell-carrying cargo transporters, the micromotors' performance in high-viscosity media was investigated to mimic more *in vivo*-like conditions (Fig. 5.3. B). Here, no significant velocity increase for $f > 5$ Hz could be measured for individual spiral-type micromotors in methyl cellulose-containing medium (MCM), which is a direct consequence of the medium's high viscosity (ca. 20x that of water, section 3.5.2.1) that limits the micromotors' capability to follow higher actuation frequencies because of high viscous drag (section 2.3). Moreover, the average maximum velocity at these relatively low frequencies (green column in Fig. 5.3 E) was significantly smaller in total than at comparable actuation frequencies in water-based cell culture medium (i.e. TCMair). This can be explained by the fact that spirals are not directly rolling on the substrate floor of the respective channel, contrary to what observations by live microscopy would

suggest. If a spiral that is standing perpendicular to the substrate plane (as in Fig. 5.2 B) is simplified as a rolling wheel with a circumference of approximately 1000 μm , it should also travel that distance on the substrate for every full turn that it rotates when actuated by the external RMF – which means that at $f = 5 \text{ Hz}$ it should cover 5 mm in one second, whereas it only reaches ca. 800 $\mu\text{m/s}$ in cell culture medium and ca. 150 $\mu\text{m/s}$ in MCM (Fig. 5.3 E). This discrepancy can be explained to a certain degree by the fact that the spiral micromotor does not directly follow the externally applied actuation frequency. As mentioned above, it was observed under the microscope that the velocity of the spirals saturates at a certain frequency, i.e. they do not rotate synchronous to the externally applied f , albeit they do rotate nonetheless (unlike helices above their respective step-out frequency). Moreover, most spirals rotated and propelled stably at $f = 1 \text{ Hz}$, and while their average velocity increased marginally in the actuation range up to $f \approx 10 \text{ Hz}$, it did not increase with a factor directly proportional to f , e.g. spirals rotated and propelled faster at 5 Hz compared with 1 Hz, yet not 5 times faster. This behavior was clearly visible in MCM, as the velocities of spirals in that medium were generally smaller compared with those in cell culture medium. Nonetheless, the measured velocities in MCM are actually so low that a rolling spiral should not be able to make even only one full turn in one second, as this would already result in a multitude of the actually observed 150 $\mu\text{m/s}$ according to the aforementioned estimation. However, with a frame rate of 10 fps it was verified with live microscopy videos that spirals rotated stably in the range of 1 – 2 Hz in MCM. This means, also in accordance with the aforementioned observations, that a spiral does not simply roll on the substrate floor, but that there is a stream of fluid between the substrate and the micromotor where it is slipping (and paddling) rather than rolling, which hampers the directly proportional translation of rotational to forward motion, and even more so in high-viscosity fluids. In that sense, spiral micromotors behave comparably to helical micromotors, which propel by corkscrew "gliding" (because of drag anisotropy), and not by rolling [111]. Similarly, helical micromotors that swim close to the substrate also exhibit a rolling (or drift) component that diverts them sideways relative to their forward swimming motion, as was observed in this work and many other studies of similar helical swimmers [96], [117], [201]. In fact, the tubular opening of a spiral micromotor – as the part where the approximate spiral-shaped "wheel" is broken – is the geometrical feature that dominates its rolling motion and makes it overcome hydrodynamic slipping to a certain degree. With every turn, a spiral is gliding along the substrate surface while rotating up to the point where the fin along its backbone is interrupted, drawing closer to the surface with the spiral opening, and hobbling over the opening secant until further rotation reestablishes the gliding along its backbone. This uneven hobbling motion was confirmed with live microscopy

observations. Moreover, simulations of hydrodynamics (implemented by the author's colleague Dmitriy Karnaushenko, data not provided) confirmed that the contribution to forward propulsion of anisotropic hydrodynamic drag owing to the spiral's chirality is not significant, compared with the described periodic hobbling over the spiral's opening when rolling on a surface as in Fig. 5.2. The secant along the spiral opening, i.e. from the outer spiral wall along the tubular opening diameter up to the point on the spiral backbone where the helical fin has its starting point, has a length of ca. 228.9 μm (for spirals with dimensions as in Fig. 5.1 E) and represents the step length that the spiral can translate with every full turn, although still compromised by hydrodynamic slip. In high-viscosity MCM, when spirals rotated at an effective frequency of ca. 1 Hz, those 228.9 $\mu\text{m}/(\text{s})$ serve as a good approximation for the maximum attainable velocity.

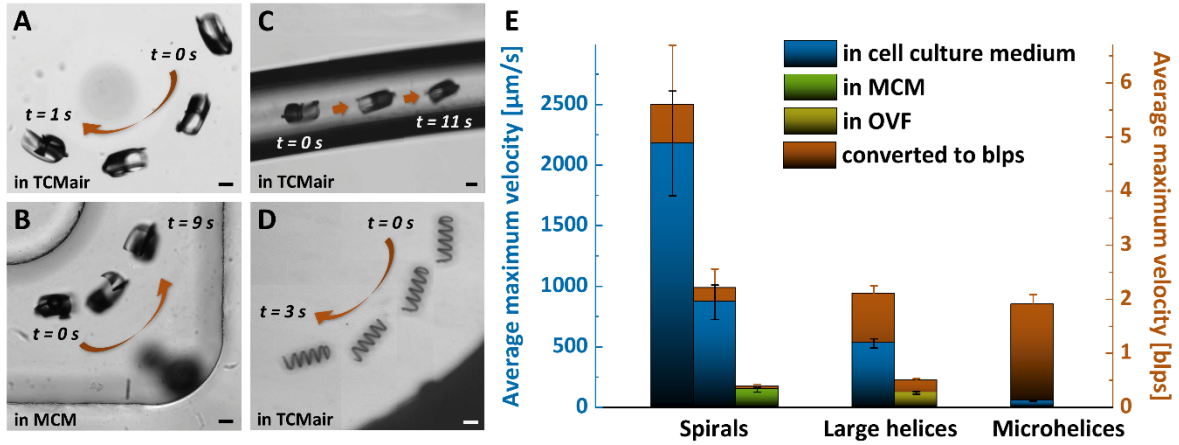


Figure 5.3: Propulsion performance of micromotors in different environments; A) spiral-type micromotors in TCMair cell culture medium; B) in MCM; C) in a narrow PTFE tubing in TCMair; D) large helix in TCMair (all scale bars 100 μm); E) average maximum velocities (blue), normalized to respective body lengths (red) of different micromotors in different media at respective maximum actuation frequencies; microhelices as in section 4; large helices as up-scaled versions of microhelices as in Fig. 5.1 D; spiral-type micromotors as in Fig. 5.1 E (two sets of blue and red columns for spirals at maximum frequency (left) and at ca. 5 Hz (right); yellow and green columns (with associated red columns) denote samples in high-viscosity media (MCM and OVF).

The large helices were also investigated in high-viscosity medium, albeit in real *bovine* oviduct fluid (OVF), not MCM. In fact, MCM with 0.6 % methyl cellulose was composed to mimic OVF in terms of viscosity, as OVF could only be obtained in extremely low quantities (section 3.5.3.1). As depicted in Fig. 5.3 E, the large helices reached marginally smaller average velocities in OVF than the spirals in MCM, following the trend of both types of micromotors in water-based cell culture medium. However, it

must be noted that at this point it is not clear whether the viscosity matching of MCM to OVF is sufficient to accurately mimic the latter's hydrodynamic behavior, for example regarding non-Newtonian behavior and cellular debris in the natural body fluid. Swimming experiments of small and large helices in MCM could serve to clarify this, yet were not conducted within the scope of this work, as helices in general were outperformed by spirals regarding the intended task of cargo transport, which will be demonstrated and discussed in the following sections. Besides properties of the respective body fluid, spatial confinement is another constraint that challenges *in vivo* applicability of micromotors. In the natural case of fertilization and subsequent embryo development, the dividing zygote is actually squeezed through a relatively narrow and flexible oviduct, and also sperm cells swim close to the walls of the oviduct before fertilization, and not freely in the tubal lumen [150], [161], [165]. Consequently, a micromotor that has the task to place a fertilized oocyte into the oviduct (coming from the uterus), executing the proposed alternative ZIFT concept, has to be able to propel in this environment as well, closely surrounded by epithelium-lined walls. In principle, the spiral-type and helical micromotors should both be able to propel in such confinement, provided there is still liquid between the respective propeller and the walls, which allows the structure to rotate and displace liquid without becoming stuck. Nonetheless, the motion efficiency, i.e. the translation of rotation to forward motion will be severely decreased because of greater hydrodynamic resistance and viscous dissipation close to the walls [202]. Regarding magnetic actuation, spatially confined propellers might not be able to follow frequencies of the RMF which they still could follow in the bulk fluid, because of the increased "power consumption" close to walls [202]. These assumptions were verified in experiments where spirals and large helices were actuated to swim through PTFE tubings with an inner diameter of 500 μm (Fig. 5.3 C). The spiral-type micromotors could travel through the tubings, albeit with relatively low average velocities of $85 \pm 6.8 \mu\text{m/s}$ in TCMair and $22 \pm 6.0 \mu\text{m/s}$ in MCM, respectively. The large helices could only be actuated successfully with a maximum frequency of 1.5 Hz and reached an average velocity of $26 \pm 6.9 \mu\text{m/s}$ in MCM. So, both types of micromotors propelled ca. 4 times more slowly in a narrow tubing compared with swimming with no significant confinement in high-viscosity medium. In absolute values, helices might have reached marginally greater velocities than spirals because they rotate along their long axis which is aligned parallel to the tubing walls, which means that, considering their diameter of 100 μm , their rotation was less confined by the tubing than that of spirals with their rotation axis perpendicular to the tubing and a diameter (the spiral footprint) of 390 μm . Considering this, it cannot be concluded unequivocally which type of micromotor is the better swimmer for *in vivo* applications in general, however, considering the intended application of zygote transport and

delivery, the spiral proved to be superior to the helix, as will be demonstrated in the following section.

5.3 Capture, Transport, and Release of Zygotes

The possibility to capture, transport, and release zygotes, i.e. fertilized oocytes, with micromotors to realize a novel, alternative ZIFT concept was investigated in several proof-of-concept experiments. The customized spiral-type micromotor design was tested and compared with up-scaled helical micromotors. Fig. 5.4 A and B illustrate the capture and release of a *murine* oocyte with one and the same spiral micromotor in a PDMS microchannel, respectively. Note that in the depicted case, the two inverse processes both happen during counterclockwise rotation of the spiral. The difference lies in the orientation of the spiral.

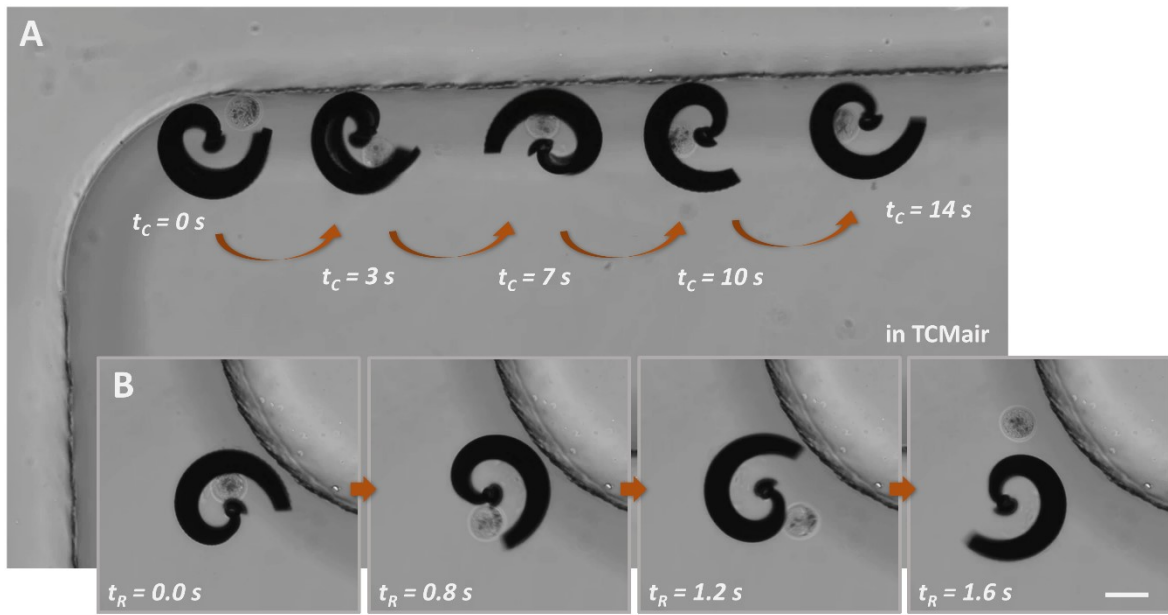


Figure 5.4: Coupling of spiral-type micromotors with cellular cargo; A) capture of a *murine* oocyte; B) release of the same cell at a different position in the PDMS microchannel (scale bars 100 μm).

For cargo capture, the opening of the spiral has to rotate towards the target cell, whereas for cargo release, the opening rotates away from the contained cell, which was achieved with the same direction of rotation in the depicted case as the spiral was oriented with flipped z-orientation in the release case compared with the capture case. Note that for cargo capture, the spiral has to travel towards the target cell first, so a slight tilt of the apparently flat orientation with respect to the substrate plane was

necessary to achieve progressive motion, as discussed in the previous section, which lead to further forward progression of the rotating spiral during the capture process, as displayed in the depicted case (Fig. 5.4 A). However, the inclination was kept below 15° , as cargo capture was easier with relatively low forward velocities and to ensure visualization of the capture process from the top view perspective. For cargo release, no progressive motion is necessary, so the captured oocyte in Fig. 5.4 B could be released simply by in-plane rotation of the spiral lying flat (but inversed) on the channel surface. Nonetheless, this fact necessitated a different arrangement of the time-lapse screenshots which explains the asymmetric arrangement of the capture and release processes in Fig. 5.4. Also evident from the images in Fig. 5.4 is the fact that the cargo-loaded spiral travelled to a different part of the PDMS channel before the oocyte was released. Such cargo capture, transport, and release sequences in microfluidic channels were recorded with several micromotor samples and fertilized oocytes (after conventional IVF, section 3.4.3). An exemplary transport case of a zygote, a fertilized oocyte that underwent cell division, is displayed in Fig. 5.5 A. The zygote was captured by the spiral micromotor beforehand and transported from one end to the other in a PDMS microfluidic channel platform. Note that, unlike with the oocyte in Fig. 5.4, the cleaved cell nuclei of the transported zygote are clearly visible in Fig. 5.5 A, V. Especially when going around corners, as displayed in panels II and IV of Fig. 5.5 A, the advantage of the spiral design, as compared with helices, becomes apparent. The cellular cargo was not lost unintentionally at any point of the transport, neither by sudden changes of direction or orientation of the micromotor, nor by contingent stops or necessary realignments. With the large, up-scaled helices, such resilient transport behavior could not be achieved. Fig. 5.5 B, II displays an exemplary case where a helix that pushed a zygote was directed to swim around a corner in a parafilm channel in OVF and the cell was lost in the process. Although this was not always the case, as it was observed that a weak hydrodynamic vortex is established inside of a rotating microhelix, which can pull the cellular cargo towards the front opening of the moving helix and thus fix it there even when the helix changes its direction, this mechanism did not prove to be sufficiently reliable to guarantee fast and efficient transport. Moreover, once the helix stops rotating, this "connection" to the cargo is lost immediately. With the spiral-type micromotor, zygotes or similar spherical cells and particles can be captured and transported reliably through channels of several centimeters of length, which was verified in several transport experiments similar to the one depicted in Fig. 5.5 A. In the given example, a track of approximately 2.6 cm was covered in 31 s, i.e. the captured zygote was transported with an average velocity of approximately $840 \mu\text{m/s}$. When comparing this velocity to the sperm cell transport case of section 4, several important points must be considered. First of all, the spiral

micromotor is much larger than a spermbot microhelix, so naturally its average velocity is greater. Moreover, in the process of cell capture, an actuated magnetic microhelix was slowed down at first to make it easier to thread in the sperm tail, and then driven with the maximum possible rotation frequency after successful capture, to transport the sperm efficiently. However, a cargo-loaded spiral micromotor was so large and fast that it could not be controlled conveniently at the maximum possible velocity, given that even at the lowest magnification of 10x under the microscope it would have still gone out of the field of view too fast, so that continuous and fast stage movements would have been necessary to constantly visualize the micromotor during cell transport. This problem was already discussed in the previous section and applies to cargo-loaded spiral-type micromotors as well.

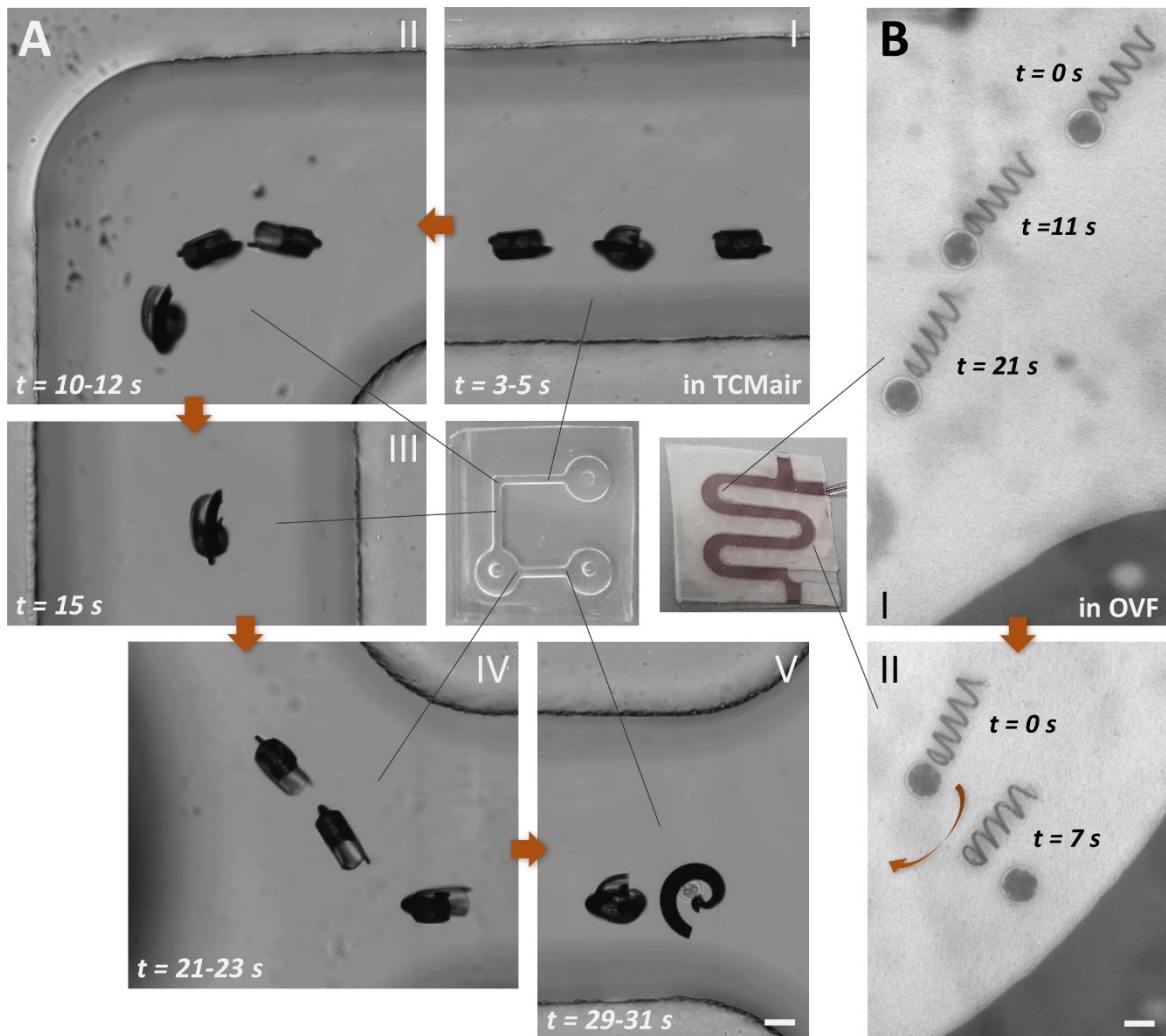


Figure 5.5: Transport of zygotes through microchannels; A) *murine* zygote transported by a spiral-type micromotor through PDMS channel (I – V); B) *bovine* zygote transported (I) and lost (II) by an up-scaled helical micromotor in a parafilm channel (scale bars 100 μm , smaller images in the middle depict the respective microfluidic channel platforms).

Consequently, the aforementioned $840 \mu\text{m/s}$ were still far from the maximum possible velocity of a cargo-loaded spiral micromotor in the given setup, as here the rotation frequency of the external RMF was limited to 5 – 10 Hz during transport. Fig. 5.6 serves to illustrate how cargo-loaded spirals compare with unloaded ones, regarding average velocity, again also compared with large, up-scaled helical micromotors, and in different liquid media. The average velocities of several spirals and large helices when swimming through a microfluidic channel, and the velocity of the same microstructure swimming in the same channel when coupled with a fertilized oocyte, respectively, are displayed (Fig. 5.6 A). Actuation frequencies were held constant for spirals and helices, respectively, in the cases before and after coupling.

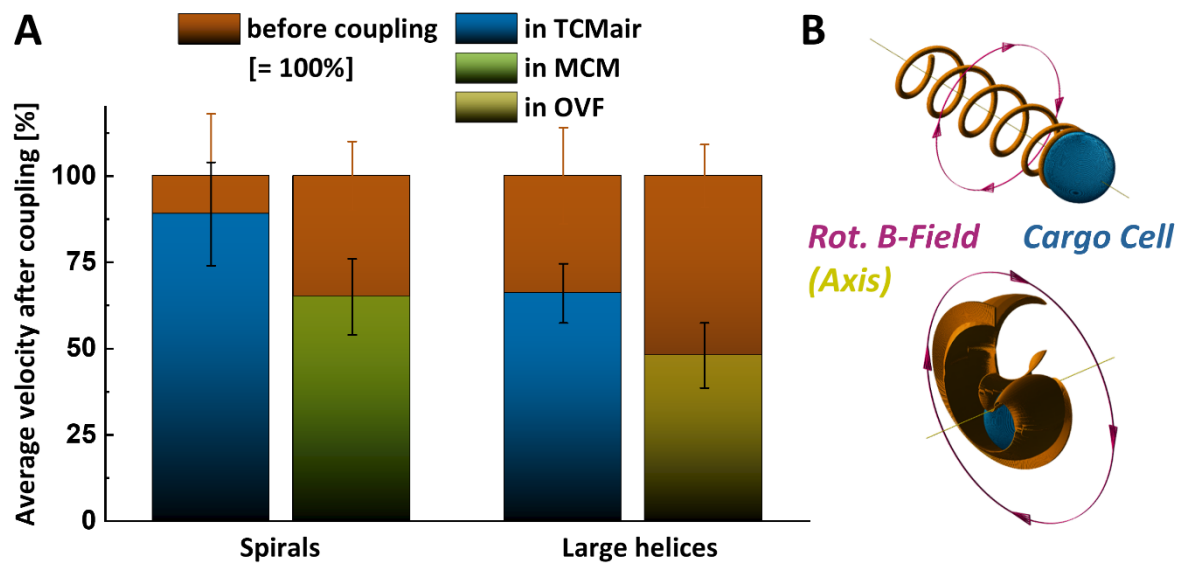


Figure 5.6: Propulsion performance of zygote-carrying micromotors before and after cargo coupling; A) average velocities before (red) and after coupling (blue), relative to the respective initial average velocity (green and yellow columns denote average velocities after coupling in MCM and OVF, respectively); B) cargo transportation scheme of large helix (above) and spiral (below) with marked axis of rotation (yellow lines) of the respective micromotor as well as the RMF (purple circles with arrows).

Normalized to the average velocity of the respective unloaded micromotor, it becomes clear that spirals are not only faster than large helices in general after cargo coupling, but also that the relative velocity decrease of the cargo-loaded spirals, compared with the unloaded ones, is not as pronounced as the relative velocity decrease of large helices after coupling. Whereas the spirals with coupled cells retain ca. 90 % of their initial velocity in TCMAir, the velocity of the cell-coupled large helices drops to approximately two thirds of the initial value. Considering the even greater velocity decrease of approximately 50 % for the sperm-capturing microhelices discussed in

section 4.3, it should be noted that in the case of coupled spherical cells such as zygotes, there is no tail that can interfere with the swimming performance of the coupled micromotor, regarding hydrodynamic drag, which could explain why large helices with zygotes perform superior to helical spermbots in terms of relative velocity decrease. Hydrodynamic drag also explains the different performance of the cell-coupled spirals and the large helices compared with their respective uncoupled states. A spiral micromotor takes the cellular cargo up "into" its body, close to its axis of rotation and center of resistance (Fig. 5.6 B). The outer surface area of the coupled micromotor as a whole entity, which is subject to hydrodynamic drag, is not altered significantly compared with the uncoupled spiral. However, a helical micromotor carries the spherical cargo in front of itself simply by pushing, so the drag on the cargo adds significantly to the drag on the helix, as the entire front surface of the cargo sphere is subject to drag while it does not contribute any drag anisotropy that could benefit the forward movement of the propelling helix (Fig. 5.6 B). Simulations of hydrodynamics (implemented by the author's colleague Dmitriy Karnaushenko, data not provided) confirmed that the flow profile around a helix changes with a coupled cargo particle, and its velocity decreases significantly, while such a strong influence of the cargo could not be observed with a loaded spiral-type micromotor. In line with these findings, the cargo-loaded spirals also perform better in high-viscosity medium than the large helices that are pushing zygotes (Fig. 5.6 A), while both velocities scale down, as compared with the respective velocities after coupling in TCMair, with approximately the same factor. Note that these velocities are all relative to the respective velocities of the uncoupled micromotors as they were summarized with absolute values in Fig. 5.3 E in the previous section. The efficient and reliable transport of spherical cellular cargo in cell culture medium and high-viscosity fluid justifies the novel design of the spiral-type micromotors, and their applicability for zygote capture, transport, and release towards micromotor-assisted ZIFT has been demonstrated.

5.4 Transfer between Separate Environments

As mentioned above, the crucial advantage of spiral-type micromotors over helices is their ability to reversibly encapsulate cellular cargo and protect it during transport. The resilience of the cargo coupling was demonstrated in transport experiments through microfluidic channels in the previous section and shall also be verified during pipette transfers of the cargo-loaded spirals between different microenvironments. This would be important for the potential *in vivo* application of any microcarrier, given that a micromotor has to be loaded in the laboratory and transferred to the body by

injection before it can operate and deliver its cargo inside the body. Evidently, a micromotor such as a helix that loosely shoves cargo cannot be transferred together with the cargo, e.g. a zygote, without losing the cargo coupling in the process. Conversely, the spiral-type micromotor can protect and preserve the cargo coupling not only during its own (magnetically actuated) motion, but also when being pipetted between different environments, for example from a PDMS microchip to a Petri dish. This was verified experimentally with *murine* zygotes and is displayed in Fig. 5.7. The spirals were actuated inside of a trimmed 10 μl pipette tip that served as a tubular microchannel with an inner diameter of 500 – 1500 μm .

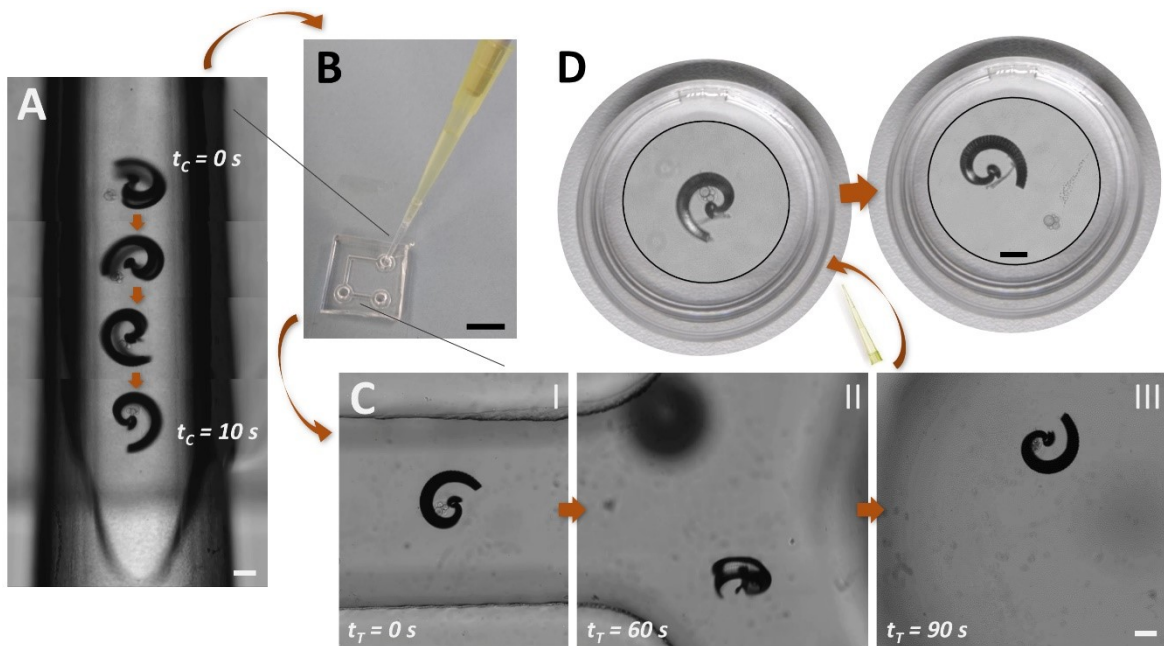


Figure 5.7: Transfer of a cargo-loaded spiral between different environments; A) capture of a *murine* zygote inside of a trimmed 10 μl pipette tip in M2; B) transfer of the cargo-loaded spiral to a PDMS microfluidic channel by pipetting; C) transport of the zygote to the other end of the PDMS channel by magnetic actuation in M2; D) transfer of the cargo-loaded spiral to a Petri dish by pipetting, and release of the *murine* zygote by magnetic actuation (all scale bars 100 μm except in B) 1 cm, and in D) Petri dish diameter is 3 cm, with magnified insets).

As displayed in Fig. 5.7 A, a *murine* zygote that already underwent cell division after fertilization was captured by a spiral-type micromotor under external magnetic control in M2 mouse embryo medium. By attaching the trimmed pipette tip to a larger, clean 100 μl tip, the cargo-loaded micromotor could be transferred to a PDMS microfluidic channel platform by pipetting (Fig. 5.7 B), all in the same cell culture medium (M2). As already demonstrated similarly in the previous section, the captured zygote could be transported through the PDMS channel and delivered to the opposite channel outlet

by magnetic actuation under the microscope (Fig. 5.7 C). Ultimately, the cargo-loaded micromotor was transferred again by pipetting to a Petri dish filled with M2. The zygote remained confined inside the spiral carrier (Fig. 5.7 D, left) until it was released intentionally by magnetic actuation (Fig. 5.7 D, right), similar to the case depicted in section 5.3. The images of Fig. 5.7 depict the same zygote and spiral in all transfer and transport steps, although a dust particle became stuck to the micromotor during the last step of transfer to the Petri dish, probably owing to a pollution of the pipette tip that was used (Fig. 5.7 D). Nonetheless, the consecutive capture, transport, and resilient transfer of a zygote coupled to a spiral-type micromotor was demonstrated in this proof-of-concept experiment. Especially the safe and resilient transfer of the loaded carrier between separate microenvironments, and also the controlled cargo transport and release solely by an external RMF, are important steps towards *in vivo* applicability that have not been achieved in this coherent manner prior to this work. The different steps depicted in Fig. 5.7 D were reproduced individually with several spirals, zygotes and 100 μm diameter PS particles (as cell dummies), also in MCM instead of M2, and two times more in a consecutive manner with PS particles. Transfer failures, i.e. cargo loss during pipetting, was observed when the pipetting was performed too carelessly and when bubbles were generated in the channels, which lead to unwanted capillary forces. Moreover, an adjustment of the dimensions of the spiral-type micromotor was required, given that *murine* zygotes were smaller than the PS particles (whereas *bovine* zygotes were larger). If the spiral was too large, the captured cellular cargo was more likely to be lost during pipetting, whereas if the spiral was too small, a cell could not be captured at all, or captured, yet not easily released by (reversed) rotation. This straightforward and obvious size adaption necessity was complicated by the fact that oocytes and zygotes of one donor species are not perfectly uniform in size, and the size of one cell might change depending on its viability. When the cells were of bad quality, or when the experiment ran for too long, it could be observed that cells which were presumably dead or about to die, swelled significantly, i.e. their diameter increased beyond the usual average. Cell viability during the experiment, and also the success rate of the preceding conventional IVF, proved to be critical factors that will be discussed in the following section.

5.5 Zygote Viability and Further Development

With the sperm-carrying microhelices, the retained viability of the captured cell during the microrobotic transport could be monitored by hypoosmotic swelling, as demonstrated in section 4.5. Such a convenient indication of viability was not available

for the oocytes and zygotes transported by spiral-type micromotors. A natural confirmation of the innocuousness of the manipulation of fertilized oocytes with magnetically actuated spirals would be the observation of further cell divisions of the developing embryos after micromanipulation. However, this was not observed in the laboratory with the described setups and experiments. Nonetheless, from that alone it cannot be concluded that the spiral-type micromotors are not biocompatible. Fluorescence stainings of fertilized and unfertilized (control) oocytes were conducted with *murine* and *bovine* cells after IVF and after micromanipulation experiments, as described in section 3.4.5. Here, fertilized, unfertilized, incubated, co-incubated (with micromotors), and also micromanipulated oocytes all exhibited relatively poor viability rates two days after the fertilization time point, along with poor IVF success rates especially for *murine* cells. Apparently, the laboratory conditions and the handling of oocytes in general were not ideal to ensure proper embryo development with the means available, while the experimental conditions during micromanipulation did not work in favor of that as well, as no CO₂ control was available during magnetic actuation and also the deployed temperature control was compromised by the eventual heating of the electromagnetic coils (during prolonged operation at 20 mT), and the necessity of many steps of pipetting, e.g. from the sample to the microfluidic channel and back to the cell culture dish. Fig 5.8 A displays a typical example of stained *bovine* oocytes after IVF.

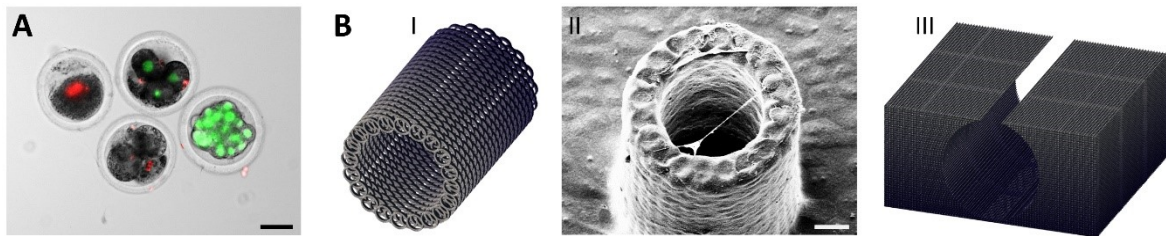


Figure 5.8: Embryo development and the artificial oviduct; A) live/dead (green/red) fluorescence staining of fertilized *bovine* oocytes in early stages of embryo development (scale bar 50 μm); B) artificial oviduct design with mesh-like morphology (I) to allow cell adhesion and proliferation (II) of MDCK cells as model epithelium (SEM image, scale bar 25 μm), and alternative artificial oviduct design for on-chip integration and microfluidic flow application (III).

As displayed in Fig. 5.7 A, *murine* zygotes that already underwent cell division after fertilization were captured by spiral-type micromotors under external magnetic control in M2 mouse embryo medium. In general, the quality of the oocytes, the IVF success rates, and the viability of the early embryos were not sufficiently good to allow a confident assessment of the influence of subsequent micromanipulation experiments, as the amount of control embryos was limited and frequently exhibited poor viability as well. Nonetheless, it should be noted that the base materials of the spiral-type

micromotors, i.e.Ormocomp coated with Fe and Ta, were chosen because of their known biocompatibility [177], [192], which is considered as superior to IP-Dip, Ni, and Ti, the materials of the microhelices that proved to be biocompatible, at least when co-incubated with sperm cells, in section 4.5. Considering the unfavorable cell culture conditions *in vitro*, this issue can be solved when the entire setup is transferred to its intended *in vivo* application where the conditions for embryo development are supposedly ideal. However, other obstacles are then to be expected, for example the spatial confinement that could hamper the motors' motion, as was demonstrated with narrow PTFE tubings and discussed in section 5.2. Moreover, the elastic, epithelium-lined walls of the natural oviduct could prove to be too sticky and the oviduct fluid in its natural state too viscous for micromotors to move, complete their task, and be retrieved afterwards, within a reasonable time frame. *In vivo* experiments, for example in mice, are necessary to confirm the applicability of the proposed concept of micromotor-assisted ZIFT conclusively. It was not possible to conduct such experiments in the available laboratories within the scope of this work, however, first steps towards an alternative approach to accurately mimic *in vivo* conditions with an *in vitro* setup are presented in Fig. 5.8 B. An artificial oviduct can be a suitable environment, if real oviduct epithelial cells of the target species can be seeded to proliferate naturally on a synthetic scaffold. The alignment and polarization of the cells is thereby crucial and the integration of the tubular scaffold into an on-chip setup would be desirable to apply fluid flow and to control the incubation conditions, as was demonstrated in an exemplary work with *bovine* oviduct epithelial cells [203] that features a more mature setup than the preliminary results of a tubular mesh with seeded MDCK cells that is displayed in Fig 5.8 B, I and II, respectively. Nonetheless, the proposed design in Fig 5.8, III potentially allows to culture natural *murine* or *bovine* oviduct epithelial cells in an on-chip environment similar to [203], to establish realistic conditions for micromotor-assisted fertilization, ZIFT, and subsequent embryo development experiments in an advanced *in vitro* setup.

6 Conclusions and Prospects

The relevance of magnetically actuated micromotors for biomedical *in vivo* applications was reviewed in detail. Assisted reproductive technology in particular is a field where magnetic micromotors can make a significant impact with their ability of untethered transport and delivery of microscopic cargo. It was demonstrated that the established corkscrew propeller helix [94], [95], as well as a novel spiral structure can be designed and fabricated by 3D laser lithography to serve the purpose of transporting *bovine* sperm cells and *bovine* and *murine* oocytes and zygotes at the microscale. Individual capture and transport of non-motile *bovine* sperm cells by microhelices was performed as a novel approach to remedy complete asthenozoospermia. The successful delivery to oocytes in an *in vitro* setup was achieved, as well as subsequent release of the sperm from the microhelix in a proof-of-concept experiment, to demonstrate the feasibility of micromotor-assisted fertilization. Further steps towards the goal of fertilization were presented, demonstrating the possibility to monitor the viability of micromotor-coupled, immotile sperm cells by hypoosmotic swelling, the biocompatibility of the synthetic carriers, and the potential biochemical functionalization of micromotors to achieve cumulus penetration. The propulsion velocity of spermbot microhelices was found to be comparable to motile *bovine* sperm, however, the qualitative difference between corkscrew propulsion and sperm tail beating could result in significant performance differences in the *in vivo* environment, especially regarding cumulus penetration. Nonetheless, the potential transfer of the micromotor-assisted fertilization concept to the *in vivo* environment is its main advantage over ICSI which is the current method of choice to counter complete asthenozoospermia [171]. It was verified experimentally that even as few as 10 sperm cells at the fertilization site can achieve fertilization, although the realization of that goal with spermrobots in an *in vivo* model, i.e. animal testing, remained beyond the scope of this work. The requirement of a suitable *in vivo* imaging technology for the deep-tissue monitoring of individual microcarriers in real time was discussed, and remains a key challenge for biomedical micromotors in general. Prospective improvements of propulsion performance, especially considering *in vivo* challenges such as high-viscosity body fluids and confined environments, could be faced with further modifications of the micromotor geometry, which was demonstrated with the second magnetic micropropeller presented in this work, the novel spiral-type micromotor. The spiral, as mentioned above, was applied to capture and transport fertilized *bovine* and *murine* oocytes for the purpose of untethered, non-invasive embryo transfer (after IVF). Analogous to micromotor-assisted fertilization, the advantage of the presented approach lies in the

possible *in vivo* transfer of a decisive step of conventional IVF – embryo development – which is currently done *in vitro* (after IVF) or by surgery, i.e. ZIFT [154]. Capture, transport, and release of *bovine* oocytes and zygotes was demonstrated with the spirals, as well as with up-scaled helical propellers, and the superior propulsion and transport performance of the spirals was verified in cell culture medium and high-viscosity fluid, in microfluidic channels and confined tubings. The spirals and helices were both actuated by a rotating magnetic field, however, the different swimming mechanism and the cargo-enclosing geometry of the spiral exhibited a significant advantage over the helix. *Bovine* and *murine* zygotes could be captured in a safe and resilient manner, i.e. the cargo-to-micromotor coupling was not lost during magnetic actuation and also not during pipetting between different *in vitro* environments, while the couplings still proved to be reversible upon intentional magnetic (counter-) actuation. Unlike other reported reversible and resilient cargo capture and release mechanisms, which are often based on stimuli-responsive polymers [199], or complex geometries and actuation modes [64], [198], the proposed spirals are simple and rely only on a rotating magnetic field, which greatly benefits feasibility and biocompatibility regarding potential *in vivo* application. However, a favorable outcome of embryo development, as compared with conventional surgical ZIFT, which would be the main motivation for applying the described untethered, non-invasive ZIFT by micromotors, could not be verified because of the aforementioned absence of *in vivo* experiments within the scope of this work. Considering this, conceptual and preliminary studies on a tissue engineering scaffold were presented towards the implementation of a 3D *in vitro* culture of oviduct epithelial cells, with the goal of designing an artificial oviduct that would improve the experimental setup of *in vitro* studies of micromotor-assisted fertilization and embryo development significantly. Prospectively, this approach can serve to mimic *in vivo* conditions in the laboratory more accurately and advance the studies on micromotor-assisted reproductive technology, as well as studies on sperm behavior and embryo development inside the fallopian tube in general. In summary, the present dissertation reports conceptual and technical advances in the novel field of micromotor-assisted reproduction and the realization of two novel applications, transport and delivery of immotile sperm cells and transport and delivery of fertilized oocytes by tailored magnetic micropropellers – verified in proof-of-concept experiments – towards micromotor-assisted fertilization and micromotor-assisted ZIFT. The presented steps towards the realization of controlled, untethered, non-invasive operation of micromotors inside the patient's body are expected to benefit current ART to counter infertility in particular, and the bustling research on micromotors for biomedical applications in general.

Appendix

A1: GWL programming sheet of microhelices with annotations*

```

1  TimestampOn %% for documentation
2  InvertZAxis 1 %% for dip-in laser lithography configuration
3  var $pitch = 6.5 %% parameter to set the helix pitch length
4  var $windings = 4 %% parameter to set the number of helix windings
5  var $radius = 2 %% parameter to set the helix radius
6  var $pi = 3.14159265359 %% parameter for the number  $\pi$ 
7  var $x = 0 %% dynamic parameter to iterate over x
8  var $y = 0 %% dynamic parameter to iterate over y
9  var $z = 0 %% dynamic parameter to iterate over z
10 var $phi = 0 %% dynamic parameter to iterate over an angle
11 var $h = 0 %% dynamic parameter to iterate over a height
12 var $x_i = 1 %% dynamic parameter to iterate over positions along x in an inner loop
13 var $y_i = 1 %% dynamic parameter to iterate over positions along y in an inner loop
14 var $x_j = 1 %% dynamic parameter to iterate over positions along x in an outer loop
15 var $y_j = 1 %% dynamic parameter to iterate over positions along y in an outer loop
16 StageVelocity 200 %% velocity of motorized stage in  $\mu\text{m/s}$  for positioning of the writing field
17 PiezoScanMode 1 %% writing mode (here: scanning within the writing field by the piezo-motorized stage)
18 PerfectShapeQuality %% for automatic scan speed adjustment
19 PowerScaling 1.0 %% scaling of maximum laser power (here "LaserPower 100" =  $100\% \cdot 1.0 \cdot 180\text{ mW}$ )
20 PiezoSettlingTime 50 %% waiting time after every "Write" command to allow accurate scanning
21 LineStartMode 1 %% for automatically taking into account the settling time after each individual line
22 LineDistance 25 %% distance between individual lines in nm
23 PolyLineMode 0 %% for the positioning of all individual lines on one side of the programmed coordinates
24 MeanderOn %% for the alternation of the writing direction of individual lines
25 for $y_j = 1 to 2 step 1 %% outer loop to iterate over positions of the entire writing field along y
26   for $x_j = 1 to 2 step 1 %% outer loop to iterate over positions of the entire writing field along x
27     ResetInterface %% for resetting the position of the interface between substrate and resist
28     MeasureTilt 4 %% for measuring the tilt of the substrate in the sample holder at 4 x 4 positions
29     TiltCorrectionOn %% for enabling the tilt correction regarding the measured positions in z
30     for $y_i = 1 to 19 step 1 %% inner loop to iterate over positions of helices along y
31       Wait 0.3 %% waiting time in s
32       FindInterfaceAt 0 %% for finding the interface between substrate and resist in z
33       ZOffset 0.1 %% offset of all programmed coordinates in z
34       YOffset 15 + ($y_i - 1) * 15 %% offset in y to position the helices within one writing field
35       for $x_i = 1 to 19 step 1 %% inner loop to iterate over positions of helices along x
36         XOffset 10 + ($x_i - 1) * 15 %% offset in x to position the helices within one writing field
37         PulsedMode %% for the addressing of individual points without connecting to lines
38         ConnectPointsOff %% for no interpolation of additional points between programmed coordinates
39         ExposureTime 50 %% exposure time at every programmed and addressed coordinate
40         LaserPower 20 %% exposure with 20 % power, relative to the power scaling of the laser
41         LineNumber 2 %% number of individual lines that are written at every addressed coordinate
42         for $phi = $pi / 2 to 2 * $pi step $pi / 2 %% loop to iterate over four points on a circle
43           set $x = ($radius + 0.0625) * cos($phi) %% x-coordinates to write a circle (the posts)
44           set $y = ($radius + 0.0625) * sin($phi) %% y-coordinates to write a circle (the posts)
45           set $z = 0 %% z-coordinate to write a circle (the posts)
46           $x $y $z %% for the addressing of the programmed coordinates within the loop
47         end %% for closing the loop over the angle $phi
48       Write %% for the exposure over all programmed coordinates of the preceding loop
49       ZOffset 0.9 %% offset of all programmed coordinates in z
50       ContinuousMode %% for continuous exposure by connecting programmed coordinates to lines
51       ConnectPointsOn %% for the interpolation of additional points between programmed coordinates
52       PerfectShapeQuality %% for automatic scan speed adjustment
53       LaserPower 40 %% exposure with 40 % power, relative to the power scaling of the laser
54       LineNumber 5 %% number of individual lines that are written at every addressed coordinate
55       for $h = 0 to 0.7 step 0.7 %% loop to iterate over a height at two positions
56         for $phi = 0 to 2 * $pi + 0.1 step 0.1 %% loop to iterate over a circle
57           set $x = $radius * cos($phi) %% x-coordinates to write a cylinder (the head ring)
58           set $y = $radius * sin($phi) %% y-coordinates to write a cylinder (the head ring)
59           set $z = $h %% z-coordinates to write a cylinder (the head ring)
60           $x $y $z %% for the addressing of the programmed coordinates within the loop
61         end %% for closing the loop over the angle $phi
62       Write %% for the exposure over all programmed coordinates of the preceding loop
63     end %% for closing the loop over the height $h
64     ZOffset 1.6 %% offset of all programmed coordinates in z
65     for $phi = 0 to $windings * 2 * $pi + 0.1 step 0.1 %% loop to iterate over several circles
66       set $x = $radius * cos($phi) %% x-coordinates to write a helix (the helical tail)
67       set $y = $radius * sin($phi) %% y-coordinates to write a helix (the helical tail)
68       set $z = $pitch / (2 * $pi) * $phi %% z-coordinates to write a helix (the helical tail)
69       $x $y $z %% for the addressing of the programmed coordinates within the loop

```

```

70     end %% for closing the loop over the angle $phi
71     Write %% for the exposure over all programmed coordinates of the preceding loop
72     end %% for closing the loop over all helix positions along x in the writing field
73     end %% for closing the loop over all helix positions along y in the writing field
74     MoveStageX 300 %% for moving the entire writing field to the next position along x
75     end %% for closing the loop over all writing field positions along x
76     MoveStageX -$x_j * 300 %% for moving the entire writing field back to the initial position along x
77     MoveStageY 300 %% for moving the entire writing field to the next position along y
78     end %% for closing the loop over all writing field positions along y
79     MoveStageY -$y_j * 300 %% for moving the entire writing field back to the initial position along y
80     SaveMessages %% for documentation

```

*An array of 1444 microhelices is represented. A microhelix consists of four posts that carry a helix head ring and a helical tail attached to the ring.

A2: GWL programming sheet of large helices with annotations*

```

1   TimeStampOn %% for documentation
2   InvertZAxis 1 %% for dip-in laser lithography configuration
3   var $pitch = 50 %% parameter to set the helix pitch length
4   var $windings = 5 %% parameter to set the number of helix windings
5   var $radius = 50 %% parameter to set the helix radius
6   var $pi = 3.14159265359 %% parameter for the number  $\pi$ 
7   var $x1 = 0 %% dynamic parameter to iterate over x
8   var $y1 = 0 %% dynamic parameter to iterate over y
9   var $x2 = 0 %% dynamic parameter to iterate over x
10  var $y2 = 0 %% dynamic parameter to iterate over y
11  var $z = 0 %% dynamic parameter to iterate over z
12  var $phi = 0 %% dynamic parameter to iterate over an angle
13  var $x_i = 1 %% dynamic parameter to iterate over positions along x in a loop
14  var $y_i = 1 %% dynamic parameter to iterate over positions along y in a loop
15  StageVelocity 300 %% velocity of motorized stage in  $\mu\text{m/s}$  for positioning of the writing field
16  GalvoScanMode %% writing mode (here: scanning within the writing field by the galvanometer-guided laser)
17  PerfectShapeIntermediate %% for automatic positioning adjustment
18  PowerScaling 1.0 %% scaling of maximum laser power (here "LaserPower 100" =  $100 \% \cdot 1.0 \cdot 180 \text{ mW}$ )
19  LaserPower 100 %% exposure with 100 % power, relative to the power scaling of the laser
20  PiezoSettlingTime 5 %% waiting time after every "Write" command to allow accurate scanning
21  GalvoAcceleration 1 %% for automatic positioning and scan speed correction
22  ContinuousMode %% for continuous exposure by connecting programmed coordinates to lines
23  ConnectPointsOn %% for the interpolation of additional points between programmed coordinates
24  LineNumber 20 %% number of individual lines that are written at every addressed coordinate
25  LineDistance 20 %% distance between individual lines in nm
26  PolyLineMode 2 %% for the positioning of all individual lines on both sides of the programmed coordinates
27  MeanderOn %% for the alternation of the writing direction of individual lines
28  ResetInterface %% for resetting the position of the interface between substrate and resist
29  for $y_i = 1 to 5 step 1 %% loop to iterate over writing field positions for a helix along y
30    for $x_i = 1 to 5 step 1 %% loop to iterate over writing field positions for a helix along x
31      Wait 0.3 %% waiting time in s
32      FindInterfaceAt 0 %% for finding the interface between substrate and resist in z
33      XOffset 0 %% offset of all programmed coordinates in x
34      YOffset 0 %% offset of all programmed coordinates in y
35      ZOffset 0 %% offset of all programmed coordinates in z
36      ScanSpeed 20000 %% laser scanning and writing speed in  $\mu\text{m/s}$  during exposure
37      for $phi = $pi to 3 * $pi + 0.02 step 0.02 %% loop to iterate over a circle
38        set $x1 = $radius * cos($phi - $pi / 5) %% x-coordinates to write a circle (the base ring)
39        set $x2 = $radius * cos($phi + $pi / 5) %% x-coordinates to write a circle (the base ring)
40        set $y1 = $radius * sin($phi - $pi / 5) %% y-coordinates to write a circle (the base ring)
41        set $y2 = $radius * sin($phi + $pi / 5) %% y-coordinates to write a circle (the base ring)
42        set $z = 0 %% z-coordinate to write a circle (the base ring)
43        $x1 $y1 $z %% for the addressing of the programmed coordinates within the loop
44        $x2 $y2 $z %% for the addressing of the programmed coordinates within the loop
45        Write %% for the exposure of a line from ($x1,$y1,$z) to ($x2,$y2,$z) within the loop
46      end %% for closing the loop over the angle $phi
47      ZOffset -3 %% offset of all programmed coordinates in z
48      ScanSpeed 10000 %% laser scanning and writing speed in  $\mu\text{m/s}$  during exposure
49      for $phi = 0 to $windings * 2 * $pi + 0.01 step 0.01 %% loop to iterate over several circles
50        set $x1 = $radius * cos($phi - $pi / 5) %% x-coordinates to write a helix (the helical tail)
51        set $x2 = $radius * cos($phi + $pi / 5) %% x-coordinates to write a helix (the helical tail)
52        set $y1 = $radius * sin($phi - $pi / 5) %% y-coordinates to write a helix (the helical tail)
53        set $y2 = $radius * sin($phi + $pi / 5) %% y-coordinates to write a helix (the helical tail)
54        set $z = $pitch / (2 * $pi) * $phi %% z-coordinates to write a helix (the helical tail)
55        $x1 $y1 $z %% for the addressing of the programmed coordinates within the loop

```

```

56      $x2 $y2 $z %% for the addressing of the programmed coordinates within the loop
57      Write %% for the exposure of a line from ($x1,$y1,$z) to ($x2,$y2,$z) within the loop
58  end %% for closing the loop over the angle $phi
59  ZOffset $windings * $pitch - 6 %% offset of all programmed coordinates in z
60  ScanSpeed 20000 %% laser scanning and writing speed in  $\mu\text{m/s}$  during exposure
61  for $phi = $pi to 3 * $pi + 0.02 step 0.02 %% loop to iterate over a circle
62      set $x1 = $radius * cos($phi - $pi / 5) %% x-coordinates to write a circle (the head ring)
63      set $x2 = $radius * cos($phi + $pi / 5) %% x-coordinates to write a circle (the head ring)
64      set $y1 = $radius * sin($phi - $pi / 5) %% y-coordinates to write a circle (the head ring)
65      set $y2 = $radius * sin($phi + $pi / 5) %% y-coordinates to write a circle (the head ring)
66      set $z = 0 %% z-coordinate to write a circle (the head ring)
67      $x1 $y1 $z %% for the addressing of the programmed coordinates within the loop
68      $x2 $y2 $z %% for the addressing of the programmed coordinates within the loop
69      Write %% for the exposure of a line from ($x1,$y1,$z) to ($x2,$y2,$z) within the loop
70  end %% for closing the loop over the angle $phi
71  MoveStageX 300 %% for moving the writing field to the next position along x
72  end %% for closing the loop over all writing field positions along x
73  MoveStageX -$x_i * 300 %% for moving the writing field back to the initial position along x
74  MoveStageY 300 %% for moving the writing field to the next position along y
75  end %% for closing the loop over all writing field positions along y
76  MoveStageY -$y_i * 300 %% for moving the writing field back to the initial position along y
77  SaveMessages %% for documentation

```

*An array of 25 large helices is represented. A large helix consists of a base ring, a helical tail attached to it, and a head ring on top.

A3: GWL programming sheet of spirals with annotations*

```

1  TimestampOn %% for documentation
2  InvertZAxis 1 %% for dip-in laser lithography configuration
3  var $radius = 85 %% parameter to set the tubular spiral opening radius (alternatively: 75, 65, or 55)
4  var $pi = 3.14159265359 %% parameter for the number  $\pi$ 
5  var $x1 = 0 %% dynamic parameter to iterate over x
6  var $y1 = 0 %% dynamic parameter to iterate over y
7  var $x2 = 0 %% dynamic parameter to iterate over x
8  var $y2 = 0 %% dynamic parameter to iterate over y
9  var $z = 0 %% dynamic parameter to iterate over z
10 var $phi = 0 %% dynamic parameter to iterate over an angle
11 var $theta = 0 %% dynamic parameter to iterate over an angle
12 var $i = 0 %% dynamic parameter to iterate over a thickness
13 var $j = 0 %% dynamic parameter to iterate over a width
14 var $x_i = 1 %% dynamic parameter to iterate over positions along x in a loop
15 var $y_i = 1 %% dynamic parameter to iterate over positions along y in a loop
16 StageVelocity 300 %% velocity of motorized stage in  $\mu\text{m/s}$  for positioning of the writing field
17 GalvoScanMode %% writing mode (here: scanning within the writing field by the galvanometer-guided laser)
18 PerfectShapeIntermediate %% for automatic positioning adjustment
19 PowerScaling 1.0 %% scaling of maximum laser power (here "LaserPower 100" =  $100 \cdot 1.0 \cdot 180 \text{ mW}$ )
20 LaserPower 100 %% exposure with 100 % power, relative to the power scaling of the laser
21 ScanSpeed 20000 %% laser scanning and writing speed in  $\mu\text{m/s}$  during exposure
22 PiezoSettlingTime 5 %% waiting time after every "Write" command to allow accurate scanning
23 GalvoAcceleration 1 %% for automatic positioning and scan speed correction
24 ContinuousMode %% for continuous exposure by connecting programmed coordinates to lines
25 ConnectPointsOn %% for the interpolation of additional points between programmed coordinates
26 LineNumber 100 %% number of individual lines that are written at every addressed coordinate
27 LineDistance 50 %% distance between individual lines in nm
28 PolyLineMode 2 %% for the positioning of all individual lines on both sides of the programmed coordinates
29 MeanderOn %% for the alternation of the writing direction of individual lines
30 ResetInterface %% for resetting the position of the interface between substrate and resist
31 for $y_i = 1 to 2 step 1 %% loop to iterate over writing field positions for a spiral along y
32     for $x_i = 1 to 6 step 1 %% loop to iterate over writing field positions for a spiral along x
33         MoveStageX 30 %% for adjusting the writing field along x
34         MoveStageY -50 %% for adjusting the writing field along y
35         Wait 0.3 %% waiting time in s
36         FindInterfaceAt 0 %% for finding the interface between substrate and resist in z
37         XOffset -30 %% offset of all programmed coordinates in x
38         YOffset 50 %% offset of all programmed coordinates in y
39         ZOffset $radius * cos(1.8 * $pi) %% offset of all programmed coordinates in z
40         for $theta = 1.8 * $pi to 1.5 * $pi step -$pi / 60 %% loop to iterate over the half-tubular spiral height
41             for $phi = 0.5 * $pi to 1.49 * $pi step $pi / 30 %% loop to iterate along the spiral backbone
42                 for $i = 0 to 4 step 1 %% loop to iterate over writing block layers
43                     set $x1 = $radius / $pi * ($phi - $pi / 30 + $pi * sin($theta)) * -cos($phi - $pi / 30)
44                     set $x2 = $radius / $pi * ($phi + $pi / 30 + $pi * sin($theta)) * -cos($phi + $pi / 30)

```

```

45     set $y1 = $radius / $pi * ($phi - $pi / 30 + $pi * sin($theta)) * -sin($phi - $pi / 30)
46     set $y2 = $radius / $pi * ($phi + $pi / 30 + $pi * sin($theta)) * -sin($phi + $pi / 30)
47     set $z = $radius * -cos($theta) + $i
48     $x1 $y1 $z %% for the addressing of the programmed coordinates within the loop
49     $x2 $y2 $z %% for the addressing of the programmed coordinates within the loop
50     Write %% for the exposure of a line from ($x1,$y1,$z) to ($x2,$y2,$z) within the loop
51     end %% for closing the loop over one writing block with $i layers of lines
52     end %% for closing the loop over the angle $phi along the spiral backbone
53 end %% for closing the loop over the angle $theta along the half-tubular spiral height
54 for $theta = 0.2 * $pi to 0.5 * $pi step $pi / 60 %% loop to iterate over the half-tubular spiral height
55     for $phi = -0.5 * $pi to 0.79 * $pi step $pi / 30 %% loop to iterate along the spiral backbone
56         for $i = 0 to 4 step 1 %% loop to iterate over writing block layers
57             set $x1 = $radius / $pi * ($phi - $pi / 30 + $pi * sin($theta)) * -cos($phi - $pi / 30)
58             set $x2 = $radius / $pi * ($phi + $pi / 30 + $pi * sin($theta)) * -cos($phi + $pi / 30)
59             set $y1 = $radius / $pi * ($phi - $pi / 30 + $pi * sin($theta)) * -sin($phi - $pi / 30)
60             set $y2 = $radius / $pi * ($phi + $pi / 30 + $pi * sin($theta)) * -sin($phi + $pi / 30)
61             set $z = $radius * -cos($theta) + $i
62             $x1 $y1 $z %% for the addressing of the programmed coordinates within the loop
63             $x2 $y2 $z %% for the addressing of the programmed coordinates within the loop
64             Write %% for the exposure of a line from ($x1,$y1,$z) to ($x2,$y2,$z) within the loop
65         end %% for closing the loop over one writing block with $i layers of lines
66     end %% for closing the loop over the angle $phi along the spiral backbone
67 end %% for closing the loop over the angle $theta along the half-tubular spiral height
68 for $theta = 0.2 * $pi to 0.5 * $pi step $pi / 90 %% loop to iterate over the half-tubular spiral height
69     set $phi = 3 * $theta - 0.9 * $pi %% for setting the helical fin position along the spiral backbone
70     for $j = 0.5 to 6 step 0.5 %% loop to iterate over the helical fin width
71         for $i = 0 to 4 step 1 %% loop to iterate over writing block layers
72             set $x1 = ($radius / $pi + $j) * ($phi - $pi / 30 + $pi * sin($theta)) * -cos($phi - $pi / 30)
73             set $x2 = ($radius / $pi + $j) * ($phi + $pi / 30 + $pi * sin($theta)) * -cos($phi + $pi / 30)
74             set $y1 = ($radius / $pi + $j) * ($phi - $pi / 30 + $pi * sin($theta)) * -sin($phi - $pi / 30)
75             set $y2 = ($radius / $pi + $j) * ($phi + $pi / 30 + $pi * sin($theta)) * -sin($phi + $pi / 30)
76             set $z = $radius * -cos($theta) + $i
77             $x1 $y1 $z %% for the addressing of the programmed coordinates within the loop
78             $x2 $y2 $z %% for the addressing of the programmed coordinates within the loop
79             Write %% for the exposure of a line from ($x1,$y1,$z) to ($x2,$y2,$z) within the loop
80         end
81     end
82 end
83 MoveStageX 100 %% for adjusting the writing field along x
84 MoveStageY 50 %% for adjusting the writing field along y
85 Wait 0.3 %% waiting time in s
86 FindInterfaceAt 0 %% for finding the interface between substrate and resist in z
87 XOffset -130 %% offset of all programmed coordinates in x
88 YOffset 0 %% offset of all programmed coordinates in y
89 ZOffset $radius * cos(0.2 * $pi) %% offset of all programmed coordinates in z
90 for $theta = 0.2 * $pi to 0.5 * $pi step $pi / 60 %% loop to iterate over the half-tubular spiral height
91     for $phi = 0.8 * $pi to 1.19 * $pi step $pi / 30 %% loop to iterate along the spiral backbone
92         for $i = 0 to 4 step 1 %% loop to iterate over writing block layers
93             set $x1 = $radius / $pi * ($phi - $pi / 30 + $pi * sin($theta)) * -cos($phi - $pi / 30)
94             set $x2 = $radius / $pi * ($phi + $pi / 30 + $pi * sin($theta)) * -cos($phi + $pi / 30)
95             set $y1 = $radius / $pi * ($phi - $pi / 30 + $pi * sin($theta)) * -sin($phi - $pi / 30)
96             set $y2 = $radius / $pi * ($phi + $pi / 30 + $pi * sin($theta)) * -sin($phi + $pi / 30)
97             set $z = $radius * -cos($theta) + $i
98             $x1 $y1 $z %% for the addressing of the programmed coordinates within the loop
99             $x2 $y2 $z %% for the addressing of the programmed coordinates within the loop
100            Write %% for the exposure of a line from ($x1,$y1,$z) to ($x2,$y2,$z) within the loop
101        end %% for closing the loop over one writing block with $i layers of lines
102    end %% for closing the loop over the angle $phi along the spiral backbone
103 end %% for closing the loop over the angle $theta along the half-tubular spiral height
104 MoveStageX -50 %% for adjusting the writing field along x
105 MoveStageY 150 %% for adjusting the writing field along y
106 Wait 0.3 %% waiting time in s
107 FindInterfaceAt 0 %% for finding the interface between substrate and resist in z
108 XOffset -80 %% offset of all programmed coordinates in x
109 YOffset -150 %% offset of all programmed coordinates in y
110 ZOffset $radius * cos(0.2 * $pi) %% offset of all programmed coordinates in z
111 for $theta = 0.2 * $pi to 0.5 * $pi step $pi / 60 %% loop to iterate over the half-tubular spiral height
112     for $phi = 1.2 * $pi to 1.49 * $pi step $pi / 30 %% loop to iterate along the spiral backbone
113         for $i = 0 to 4 step 1 %% loop to iterate over writing block layers
114             set $x1 = $radius / $pi * ($phi - $pi / 30 + $pi * sin($theta)) * -cos($phi - $pi / 30)
115             set $x2 = $radius / $pi * ($phi + $pi / 30 + $pi * sin($theta)) * -cos($phi + $pi / 30)
116             set $y1 = $radius / $pi * ($phi - $pi / 30 + $pi * sin($theta)) * -sin($phi - $pi / 30)
117             set $y2 = $radius / $pi * ($phi + $pi / 30 + $pi * sin($theta)) * -sin($phi + $pi / 30)
118             set $z = $radius * -cos($theta) + $i
119             $x1 $y1 $z %% for the addressing of the programmed coordinates within the loop
120             $x2 $y2 $z %% for the addressing of the programmed coordinates within the loop

```

```

121 Write %% for the exposure of a line from ($x1,$y1,$z) to ($x2,$y2,$z) within the loop
122 end %% for closing the loop over one writing block with $i layers of lines
123 end %% for closing the loop over the angle $phi along the spiral backbone
124 end %% for closing the loop over the angle $theta along the half-tubular spiral height
125 MoveStageX -50 %% for adjusting the writing field along x
126 MoveStageY -200 %% for adjusting the writing field along y
127 Wait 0.3 %% waiting time in s
128 FindInterfaceAt 0 %% for finding the interface between substrate and resist in z
129 XOffset -30 %% offset of all programmed coordinates in x
130 YOffset 50 %% offset of all programmed coordinates in y
131 ZOffset $radius * cos(1.8 * $pi) %% offset of all programmed coordinates in z
132 for $theta = 1.5 * $pi to 1.2 * $pi step -$pi / 60 %% loop to iterate over the half-tubular spiral height
133   for $phi = 0.5 * $pi to 1.49 * $pi step $pi / 30 %% loop to iterate along the spiral backbone
134     for $i = 0 to 4 step 1 %% loop to iterate over writing block layers
135       set $x1 = $radius / $pi * ($phi - $pi / 30 + $pi * sin($theta)) * -cos($phi - $pi / 30)
136       set $x2 = $radius / $pi * ($phi + $pi / 30 + $pi * sin($theta)) * -cos($phi + $pi / 30)
137       set $y1 = $radius / $pi * ($phi - $pi / 30 + $pi * sin($theta)) * -sin($phi - $pi / 30)
138       set $y2 = $radius / $pi * ($phi + $pi / 30 + $pi * sin($theta)) * -sin($phi + $pi / 30)
139       set $z = $radius * -cos($theta) + $i
140       $x1 $y1 $z %% for the addressing of the programmed coordinates within the loop
141       $x2 $y2 $z %% for the addressing of the programmed coordinates within the loop
142       Write %% for the exposure of a line from ($x1,$y1,$z) to ($x2,$y2,$z) within the loop
143     end %% for closing the loop over one writing block with $i layers of lines
144   end %% for closing the loop over the angle $phi along the spiral backbone
145 end %% for closing the loop over the angle $theta along the half-tubular spiral height
146 for $theta = 0.5 * $pi to 0.8 * $pi step $pi / 60 %% loop to iterate over the half-tubular spiral height
147   for $phi = -0.5 * $pi to 0.79 * $pi step $pi / 30 %% loop to iterate along the spiral backbone
148     for $i = 0 to 4 step 1 %% loop to iterate over writing block layers
149       set $x1 = $radius / $pi * ($phi - $pi / 30 + $pi * sin($theta)) * -cos($phi - $pi / 30)
150       set $x2 = $radius / $pi * ($phi + $pi / 30 + $pi * sin($theta)) * -cos($phi + $pi / 30)
151       set $y1 = $radius / $pi * ($phi - $pi / 30 + $pi * sin($theta)) * -sin($phi - $pi / 30)
152       set $y2 = $radius / $pi * ($phi + $pi / 30 + $pi * sin($theta)) * -sin($phi + $pi / 30)
153       set $z = $radius * -cos($theta) + $i
154       $x1 $y1 $z %% for the addressing of the programmed coordinates within the loop
155       $x2 $y2 $z %% for the addressing of the programmed coordinates within the loop
156       Write %% for the exposure of a line from ($x1,$y1,$z) to ($x2,$y2,$z) within the loop
157     end %% for closing the loop over one writing block with $i layers of lines
158   end %% for closing the loop over the angle $phi along the spiral backbone
159 end %% for closing the loop over the angle $theta along the half-tubular spiral height
160 for $theta = 0.5 * $pi to 0.5 * $pi + $pi / 15 step $pi / 90 %% loop to iterate over the half-tubular spiral height
161   set $phi = 3 * $theta - 0.9 * $pi %% for setting the helical fin position along the spiral backbone
162   for $j = 0.5 to 6 step 0.5 %% loop to iterate over the helical fin width
163     for $i = 0 to 4 step 1 %% loop to iterate over writing block layers
164       set $x1 = ($radius / $pi + $j) * ($phi - $pi / 30 + $pi * sin($theta)) * -cos($phi - $pi / 30)
165       set $x2 = ($radius / $pi + $j) * ($phi + $pi / 30 + $pi * sin($theta)) * -cos($phi + $pi / 30)
166       set $y1 = ($radius / $pi + $j) * ($phi - $pi / 30 + $pi * sin($theta)) * -sin($phi - $pi / 30)
167       set $y2 = ($radius / $pi + $j) * ($phi + $pi / 30 + $pi * sin($theta)) * -sin($phi + $pi / 30)
168       set $z = $radius * -cos($theta) + $i
169       $x1 $y1 $z %% for the addressing of the programmed coordinates within the loop
170       $x2 $y2 $z %% for the addressing of the programmed coordinates within the loop
171       Write %% for the exposure of a line from ($x1,$y1,$z) to ($x2,$y2,$z) within the loop
172     end %% for closing the loop over one writing block with $i layers of lines
173   end %% for closing the loop over one helical fin part with the fin width $j
174 end %% for closing the loop over the angle $theta along the half-tubular spiral height
175 MoveStageX 100 %% for adjusting the writing field along x
176 MoveStageY 50 %% for adjusting the writing field along y
177 Wait 0.3 %% waiting time in s
178 FindInterfaceAt 0 %% for finding the interface between substrate and resist in z
179 XOffset -130 %% offset of all programmed coordinates in x
180 YOffset 0 %% offset of all programmed coordinates in y
181 ZOffset $radius * cos(0.2 * $pi) %% offset of all programmed coordinates in z
182 for $theta = 0.5 * $pi to 0.8 * $pi step $pi / 60 %% loop to iterate over the half-tubular spiral height
183   for $phi = 0.8 * $pi to 1.19 * $pi step $pi / 30 %% loop to iterate along the spiral backbone
184     for $i = 0 to 4 step 1 %% loop to iterate over writing block layers
185       set $x1 = $radius / $pi * ($phi - $pi / 30 + $pi * sin($theta)) * -cos($phi - $pi / 30)
186       set $x2 = $radius / $pi * ($phi + $pi / 30 + $pi * sin($theta)) * -cos($phi + $pi / 30)
187       set $y1 = $radius / $pi * ($phi - $pi / 30 + $pi * sin($theta)) * -sin($phi - $pi / 30)
188       set $y2 = $radius / $pi * ($phi + $pi / 30 + $pi * sin($theta)) * -sin($phi + $pi / 30)
189       set $z = $radius * -cos($theta) + $i
190       $x1 $y1 $z %% for the addressing of the programmed coordinates within the loop
191       $x2 $y2 $z %% for the addressing of the programmed coordinates within the loop
192       Write %% for the exposure of a line from ($x1,$y1,$z) to ($x2,$y2,$z) within the loop
193     end %% for closing the loop over one writing block with $i layers of lines
194   end %% for closing the loop over the angle $phi along the spiral backbone
195 end %% for closing the loop over the angle $theta along the half-tubular spiral height
196 for $theta = 0.5 * $pi + $pi / 15 to 0.69 * $pi step $pi / 90 %% loop to iterate over the half-tubular spiral height

```

```

197 set $phi = 3 * $theta - 0.7 * $pi - $pi / 5 %% for setting the helical fin position along the spiral backbone
198 for $j = 0.5 to 6 step 0.5 %% loop to iterate over the helical fin width
199   for $i = 0 to 4 step 1 %% loop to iterate over writing block layers
200     set $x1 = ($radius / $pi + $j) * ($phi - $pi / 30 + $pi * sin($theta)) * -cos($phi - $pi / 30)
201     set $x2 = ($radius / $pi + $j) * ($phi + $pi / 30 + $pi * sin($theta)) * -cos($phi + $pi / 30)
202     set $y1 = ($radius / $pi + $j) * ($phi - $pi / 30 + $pi * sin($theta)) * -sin($phi - $pi / 30)
203     set $y2 = ($radius / $pi + $j) * ($phi + $pi / 30 + $pi * sin($theta)) * -sin($phi + $pi / 30)
204     set $z = $radius * -cos($theta) + $i
205     $x1 $y1 $z %% for the addressing of the programmed coordinates within the loop
206     $x2 $y2 $z %% for the addressing of the programmed coordinates within the loop
207     Write %% for the exposure of a line from ($x1,$y1,$z) to ($x2,$y2,$z) within the loop
208   end %% for closing the loop over one writing block with $i layers of lines
209 end %% for closing the loop over one helical fin part with the fin width $j
210 end %% for closing the loop over the angle $theta along the half-tubular spiral height
211 MoveStageX -50 %% for adjusting the writing field along x
212 MoveStageY 150 %% for adjusting the writing field along y
213 Wait 0.3 %% waiting time in s
214 FindInterfaceAt 0 %% for finding the interface between substrate and resist in z
215 XOffset -80 %% offset of all programmed coordinates in x
216 YOffset -150 %% offset of all programmed coordinates in y
217 ZOffset $radius * cos(0.2 * $pi) %% offset of all programmed coordinates in z
218 for $theta = 0.5 * $pi to 0.8 * $pi step $pi / 60 %% loop to iterate over the half-tubular spiral height
219   for $phi = 1.2 * $pi to 1.49 * $pi step $pi / 30 %% loop to iterate along the spiral backbone
220     for $i = 0 to 4 step 1 %% loop to iterate over writing block layers
221       set $x1 = $radius / $pi * ($phi - $pi / 30 + $pi * sin($theta)) * -cos($phi - $pi / 30)
222       set $x2 = $radius / $pi * ($phi + $pi / 30 + $pi * sin($theta)) * -cos($phi + $pi / 30)
223       set $y1 = $radius / $pi * ($phi - $pi / 30 + $pi * sin($theta)) * -sin($phi - $pi / 30)
224       set $y2 = $radius / $pi * ($phi + $pi / 30 + $pi * sin($theta)) * -sin($phi + $pi / 30)
225       set $z = $radius * -cos($theta) + $i
226       $x1 $y1 $z %% for the addressing of the programmed coordinates within the loop
227       $x2 $y2 $z %% for the addressing of the programmed coordinates within the loop
228       Write %% for the exposure of a line from ($x1,$y1,$z) to ($x2,$y2,$z) within the loop
229     end %% for closing the loop over one writing block with $i layers of lines
230   end %% for closing the loop over the angle $phi along the spiral backbone
231 end %% for closing the loop over the angle $theta along the half-tubular spiral height
232 for $theta = 0.7 * $pi to 0.79 * $pi step $pi / 90 %% loop to iterate over the half-tubular spiral height
233   set $phi = 3 * $theta - 0.9 * $pi %% for setting the helical fin position along the spiral backbone
234   for $j = 0.5 to 6 step 0.5 %% loop to iterate over the helical fin width
235     for $i = 0 to 4 step 1 %% loop to iterate over writing block layers
236       set $x1 = ($radius / $pi + $j) * ($phi - $pi / 30 + $pi * sin($theta)) * -cos($phi - $pi / 30)
237       set $x2 = ($radius / $pi + $j) * ($phi + $pi / 30 + $pi * sin($theta)) * -cos($phi + $pi / 30)
238       set $y1 = ($radius / $pi + $j) * ($phi - $pi / 30 + $pi * sin($theta)) * -sin($phi - $pi / 30)
239       set $y2 = ($radius / $pi + $j) * ($phi + $pi / 30 + $pi * sin($theta)) * -sin($phi + $pi / 30)
240       set $z = $radius * -cos($theta) + $i
241       $x1 $y1 $z %% for the addressing of the programmed coordinates within the loop
242       $x2 $y2 $z %% for the addressing of the programmed coordinates within the loop
243       Write %% for the exposure of a line from ($x1,$y1,$z) to ($x2,$y2,$z) within the loop
244     end %% for closing the loop over one writing block with $i layers of lines
245   end %% for closing the loop over one helical fin part with the fin width $j
246 end %% for closing the loop over the angle $theta along the half-tubular spiral height
247 MoveStageX -80 %% for adjusting the writing field along x
248 MoveStageY -150 %% for adjusting the writing field along y
249 MoveStageX 600 %% for moving the writing field to the next position along x
250 end %% for closing the loop over all writing field positions along x
251 MoveStageX -$x_i * 600 %% for moving the writing field back to the initial position along x
252 MoveStageY 600 %% for moving the writing field to the next position along y
253 end %% for closing the loop over all writing field positions along y
254 MoveStageY -$y_i * 600 %% for moving the writing field back to the initial position along y
255 SaveMessages %% for documentation

```

*An array of 12 spirals is represented. A spiral consists of an inner half-tube and an outer half-tube which delineate an arithmetic spiral, and a helical fin which runs along the outer half-tube wall that forms the spiral backbone. The laser writing of a spiral is split up into six parts as it spans over three writing fields which are written in two steps, i.e. first the three bottom halves and then the three upper halves. The formulas for the addressed x-, y-, and z-coordinates thereby remain the same. Analogously, the helical fin along the spiral backbone is written in four steps with identical formulas while only the iteration ranges (and writing field alignments) change.

Bibliography

- [1] V. Blumenauer *et al.*, “D.I.R-Annual 2017 - The German IVF-Registry,” *Journal of Reproductive Medicine and Endocrinology*, vol. 15, no. 5–6, pp. 216–249, 2018.
- [2] “Fertility Treatment 2017: Trends and Figures,” *Human Fertilization & Embryology Authority*, <https://www.hfea.gov.uk/about-us/publications/research-and-data/fertility-treatment-2018-trends-and-figures/> (accessed: Sep 2020).
- [3] “Assisted Reproductive Technology 2016 National Summary Report,” *National Center for Chronic Disease Prevention and Health Promotion, Division of Reproductive Health, USA*, <https://www.cdc.gov/art/reports/2016/national-summary.html> (accessed: Sep 2020).
- [4] E. Carlsen, A. Giwercman, N. Keiding, and N. E. Skakkebaek, “Evidence for Decreasing Quality of Semen During Past 50 Years,” *Br. Med. J.*, vol. 305, no. 6854, pp. 609–613, 1992.
- [5] R. B. Hakim, R. H. Gray, and H. Zacur, “Alcohol and Caffeine Consumption and Decreased Fertility,” *Fertil. Steril.*, vol. 70, no. 4, pp. 632–637, 1998.
- [6] C. H. Ramlau-Hansen, A. M. Thulstrup, A. S. Aggerholm, M. S. Jensen, G. Toft, and J. P. Bonde, “Is Smoking a Risk Factor for Decreased Semen Quality? A Cross-Sectional Analysis,” *Hum. Reprod.*, vol. 22, no. 1, pp. 188–196, 2007.
- [7] N. E. Skakkebaek *et al.*, “Populations, Decreasing Fertility, and Reproductive Health,” *Lancet*, vol. 393, no. 10180, pp. 1500–1501, 2019.
- [8] H. Merzenich, H. Zeeb, and M. Blettner, “Decreasing Sperm Quality: A Global Problem?,” *BMC Public Health*, vol. 10, pp. 24(1–5), 2010.
- [9] M. Medina-Sánchez, H. Xu, and O. G. Schmidt, “Micro- and Nano-Motors: The New Generation of Drug Carriers,” *Ther. Deliv.*, vol. 9, no. 4, pp. 303–316, 2018.
- [10] P. Erkoc, I. C. Yasa, H. Ceylan, O. Yasa, Y. Alapan, and M. Sitti, “Mobile Microrobots for Active Therapeutic Delivery,” *Adv. Ther.*, vol. 2, no. 1, pp. 1800064(1–18), 2019.
- [11] L. Ricotti, A. Cafarelli, V. Iacovacci, L. Vannozzi, and A. Menciasci, “Advanced Micro-Nano-Bio Systems for Future Targeted Therapies,” *Curr. Nanosci.*, vol. 11, no. 2, pp. 144–160, 2015.
- [12] V. Magdanz, S. Sánchez, and O. G. Schmidt, “Method for the Controlled Movement of Motile Cells in Liquid or Gaseous Media,” Patent No. DE102012212427A1 (Germany), US9883889B2 (USA), 2012.
- [13] V. Magdanz, S. Sanchez, and O. G. Schmidt, “Development of a Sperm-Flagella Driven Micro-Bio-Robot,” *Adv. Mater.*, vol. 25, no. 45, pp. 6581–6588, 2013.
- [14] O. G. Schmidt, “Method for Mobilizing Immobilized Cells,” Patent No.

- DE102014201760A1 (Germany), US20170166882A1 (USA), 2014.
- [15] M. Medina-Sánchez, L. Schwarz, A. K. Meyer, F. Hebenstreit, and O. G. Schmidt, “Cellular Cargo Delivery: Toward Assisted Fertilization by Sperm-Carrying Micromotors,” *Nano Lett.*, vol. 15, no. 1, pp. 555–561, 2016.
 - [16] L. Schwarz, M. Medina-Sánchez, and O. G. Schmidt, “Sperm-Hybrid Micromotors: On-Board Assistance for Nature’s Bustling Swimmers,” *Reproduction*, vol. 159, no. 2, pp. R83–R96, 2020.
 - [17] The Nobel Assembly at Karolinska Institutet, “The Nobel Prize in Physiology or Medicine 2010 to Robert G. Edwards for the Development of In Vitro Fertilization,” *Press Release 2010-10-04*, 2010.
 - [18] Y. Shirai, A. J. Osgood, Y. Zhao, K. F. Kelly, and J. M. Tour, “Directional Control in Thermally Driven Single-Molecule Nanocars,” *Nano Lett.*, vol. 5, no. 11, pp. 2330–2334, 2005.
 - [19] S. Erbas-Cakmak, D. A. Leigh, C. T. McTernan, and A. L. Nussbaumer, “Artificial Molecular Machines,” *Chem. Rev.*, vol. 115, no. 18, pp. 10081–10206, 2015.
 - [20] J. Rogers, Y. Huang, O. G. Schmidt, and D. H. Gracias, “Origami MEMS and NEMS,” *MRS Bull.*, vol. 41, no. 2, pp. 123–129, 2016.
 - [21] E. M. Purcell, “Life at Low Reynolds Number,” *Am. J. Phys.*, vol. 45, pp. 3–11, 1977.
 - [22] K. E. Peyer, L. Zhang, and B. J. Nelson, “Bio-Inspired Magnetic Swimming Microrobots for Biomedical Applications,” *Nanoscale*, vol. 5, no. 4, pp. 1259–1272, 2013.
 - [23] S. Palagi and P. Fischer, “Bioinspired Microrobots,” *Nat. Rev. Mater.*, vol. 3, no. 6, pp. 113–124, 2018.
 - [24] T. Xu, W. Gao, L.-P. Xu, X. Zhang, and S. Wang, “Fuel-Free Synthetic Micro-/Nanomachines,” *Adv. Mater.*, vol. 29, no. 9, pp. 1603250(1–27), 2017.
 - [25] L. Schwarz, M. Medina-Sánchez, and O. G. Schmidt, “Hybrid BioMicromotors,” *Appl. Phys. Rev.*, vol. 4, no. 3, pp. 031301(1–23), 2017.
 - [26] K. Bente, A. Codutti, F. Bachmann, and D. Faivre, “Biohybrid and Bioinspired Magnetic Microswimmers,” *Small*, vol. 14, no. 29, pp. 1704374(1–25), 2018.
 - [27] V. Magdanz, M. Medina-Sánchez, L. Schwarz, H. Xu, J. Elgeti, and O. G. Schmidt, “Spermatozoa as Functional Components of Robotic Microswimmers,” *Adv. Mater.*, vol. 29, no. 24, pp. 1606301(1–18), 2017.
 - [28] M. Medina-Sánchez and O. G. Schmidt, “Medical Microbots Need Better Imaging and Control,” *Nature*, vol. 545, no. 7655, pp. 406–408, 2017.
 - [29] A. A. Solovev, Y. Mei, E. B. Ureña, G. Huang, and O. G. Schmidt, “Catalytic Microtubular Jet Engines Self-Propelled by Accumulated Gas Bubbles,” *Small*, vol. 5, no. 14, pp. 1688–

- 1692, 2009.
- [30] W. F. Paxton, S. Sundararajan, T. E. Mallouk, and A. Sen, "Chemical Locomotion," *Angew. Chemie - Int. Ed.*, vol. 45, no. 33, pp. 5420–5429, 2006.
 - [31] M. Guix, S. M. Weiz, O. G. Schmidt, and M. Medina-Sánchez, "Self-Propelled Micro/Nanoparticle Motors," *Part. Part. Syst. Charact.*, vol. 35, no. 2, pp. 1700382(1–31), 2018.
 - [32] R. Dreyfus, J. Baudry, M. L. Roper, M. Fermigier, H. A. Stone, and J. Bibette, "Microscopic Artificial Swimmers," *Nature*, vol. 437, no. 7060, pp. 862–865, 2005.
 - [33] X.-Z. Chen *et al.*, "Recent Developments in Magnetically Driven Micro- and Nanorobots," *Appl. Mater. Today*, vol. 9, pp. 37–48, 2017.
 - [34] D. Nishiguchi, J. Iwasawa, H.-R. Jiang, and M. Sano, "Flagellar Dynamics of Chains of Active Janus Particles Fueled by an AC Electric Field," *New J. Phys.*, vol. 20, pp. 015002(1–14), 2018.
 - [35] L. Bouffier, V. Ravaine, N. Sojic, and A. Kuhn, "Electric Fields for Generating Unconventional Motion of Small Objects," *Curr. Opin. Colloid Interface Sci.*, vol. 21, pp. 57–64, 2016.
 - [36] L. Baraban *et al.*, "Fuel-Free Locomotion of Janus Motors: Magnetically Induced Thermophoresis," *ACS Nano*, vol. 7, no. 2, pp. 1360–1367, 2013.
 - [37] A. Mourran, H. Zhang, R. Vinokur, and M. Möller, "Soft Microrobots Employing Nonequilibrium Actuation via Plasmonic Heating," *Adv. Mater.*, vol. 29, no. 2, pp. 1604825(1–8), 2017.
 - [38] S. Palagi *et al.*, "Structured Light Enables Biomimetic Swimming and Versatile Locomotion of Photoresponsive Soft Microrobots," *Nat. Mater.*, vol. 15, no. 6, pp. 647–653, 2016.
 - [39] L. Xu, F. Mou, H. Gong, M. Luo, and J. Guan, "Light-Driven Micro/Nanomotors: From Fundamentals to Applications," *Chem. Soc. Rev.*, vol. 46, no. 22, pp. 6905–6926, 2017.
 - [40] D. Ahmed, T. Baasch, B. Jang, S. Pane, J. Dual, and B. J. Nelson, "Artificial Swimmers Propelled by Acoustically Activated Flagella," *Nano Lett.*, vol. 16, no. 8, pp. 4968–4974, 2016.
 - [41] K. J. Rao, F. Li, L. Meng, H. Zheng, F. Cai, and W. Wang, "A Force to Be Reckoned With: A Review of Synthetic Microswimmers Powered by Ultrasound," *Small*, vol. 11, no. 24, pp. 2836–2846, 2015.
 - [42] R. Dong, Y. Cai, Y. Yang, W. Gao, and B. Ren, "Photocatalytic Micro/Nanomotors: From Construction to Applications," *Acc. Chem. Res.*, vol. 51, no. 9, pp. 1940–1947, 2018.
 - [43] W. Gao, K. M. Manesh, J. Hua, S. Sattayasamitsathit, and J. Wang, "Hybrid Nanomotor:

- A Catalytically/Magnetically Powered Adaptive Nanowire Swimmer,” *Small*, vol. 7, no. 14, pp. 2047–2051, 2011.
- [44] D. Ahmed, C. Dillinger, A. Hong, and B. J. Nelson, “Artificial Acousto-Magnetic Soft Microswimmers,” *Adv. Mater. Technol.*, vol. 2, no. 7, pp. 1700050(1–5), 2017.
- [45] L. Soler, V. Magdanz, V. M. Fomin, S. Sanchez, and O. G. Schmidt, “Self-Propelled Micromotors for Cleaning Polluted Water,” *ACS Nano*, vol. 7, no. 11, pp. 9611–9620, 2013.
- [46] Y. Ying and M. Pumera, “Micro/Nanomotors for Water Purification,” *Chem. - A Eur. J.*, vol. 25, no. 1, pp. 106–121, 2019.
- [47] B. Jurado-Sánchez and J. Wang, “Micromotors for Environmental Applications: A Review,” *Environ. Sci. Nano*, vol. 5, no. 7, pp. 1530–1544, 2018.
- [48] S. E. Chung, X. Dong, and M. Sitti, “Three-Dimensional Heterogeneous Assembly of Coded Microgels Using an Untethered Mobile Microgripper,” *Lab Chip*, vol. 15, no. 7, pp. 1667–1676, 2015.
- [49] A. Paris, D. Decanini, and G. Hwang, “On-Chip Multimodal Vortex Trap Micro-Manipulator with Multistage Bi-Helical Micro-Swimmer,” *Sensors Actuators A*, vol. 276, pp. 118–124, 2018.
- [50] J. Guo, J. J. Gallegos, A. R. Tom, and D. Fan, “Electric-Field-Guided Precision Manipulation of Catalytic Nanomotors for Cargo Delivery and Powering Nanoelectromechanical Devices,” *ACS Nano*, vol. 12, no. 2, pp. 1179–1187, 2018.
- [51] T. Xu, J. Yu, X. Yan, H. Choi, and L. Zhang, “Magnetic Actuation Based Motion Control for Microrobots: An Overview,” *Micromachines*, vol. 6, no. 9, pp. 1346–1364, 2015.
- [52] G.-Z. Yang *et al.*, “The Grand Challenges of Science Robotics,” *Sci. Robot.*, vol. 3, no. 14, p. eaar7650(1-14), 2018.
- [53] H. Xu, M. Medina-Sánchez, V. Magdanz, L. Schwarz, F. Hebenstreit, and O. G. Schmidt, “Sperm-Hybrid Micromotor for Targeted Drug Delivery,” *ACS Nano*, vol. 12, no. 1, pp. 327–337, 2018.
- [54] M. Medina-Sánchez, V. Magdanz, L. Schwarz, H. Xu, and O. G. Schmidt, “Spermbots: Concept and Applications,” in *Biomimetic and Biohybrid Systems. Living Machines 2017. Lecture Notes in Computer Science*, Springer, 2017, pp. 579–588.
- [55] Z. Hosseinidoust, B. Mostaghaci, O. Yasa, B.-W. Park, A. V. Singh, and M. Sitti, “Bioengineered and Biohybrid Bacteria-Based Systems for Drug Delivery,” *Adv. Drug Deliv. Rev.*, vol. 106, pp. 27–44, 2016.
- [56] B. Jurado-Sánchez, “Nanoscale Biosensors Based on Self-Propelled Objects,” *Biosensors*, vol. 8, no. 3, pp. 59(1–15), 2018.

- [57] S. Campuzano, B. Esteban-Fernández de Ávila, P. Yáñez-Sedeño, J. M. Pingarrón, and J. Wang, "Nano/Microvehicles for Efficient Delivery and (Bio)sensing at the Cellular Level," *Chem. Sci.*, vol. 8, no. 10, pp. 6750–6763, 2017.
- [58] W. Xi, A. A. Solovev, A. N. Ananth, D. H. Gracias, S. Sanchez, and O. G. Schmidt, "Rolled-Up Magnetic Microdrillers: Towards Remotely Controlled Minimally Invasive Surgery," *Nanoscale*, vol. 5, no. 4, pp. 1294–1297, 2013.
- [59] G. Chatzipirpiridis *et al.*, "Electroforming of Implantable Tubular Magnetic Microrobots for Wireless Ophthalmologic Applications," *Adv. Healthc. Mater.*, vol. 4, no. 2, pp. 209–214, 2015.
- [60] M. Hansen-Bruhn *et al.*, "Active Intracellular Delivery of a Cas9/sgRNA Complex Using Ultrasound-Propelled Nanomotors," *Angew. Chemie - Int. Ed.*, vol. 57, no. 10, pp. 2657–2661, 2018.
- [61] X. Xu *et al.*, "Precision-Guided Nanospears for Targeted and High-Throughput Intracellular Gene Delivery," *ACS Nano*, vol. 12, no. 5, pp. 4503–4511, 2018.
- [62] S. Jeon *et al.*, "Magnetically Actuated Microrobots as a Platform for Stem Cell Transplantation," *Sci. Robot.*, vol. 4, no. 30, p. eaav4317(1-11), 2019.
- [63] I. C. Yasa, A. F. Tabak, O. Yasa, H. Ceylan, and M. Sitti, "3D-Printed Microrobotic Transporters with Recapitulated Stem Cell Niche for Programmable and Active Cell Delivery," *Adv. Funct. Mater.*, vol. 29, no. 17, pp. 1808992(1–10), 2019.
- [64] S. Lee *et al.*, "A Capsule-Type Microrobot with Pick-and-Drop Motion for Targeted Drug and Cell Delivery," *Adv. Healthc. Mater.*, vol. 7, no. 9, pp. 1700985(1–6), 2018.
- [65] W. Gao *et al.*, "Artificial Micromotors in the Mouse's Stomach: A Step Toward In Vivo Use of Synthetic Motors," *ACS Nano*, vol. 9, no. 1, pp. 117–123, 2015.
- [66] A. Servant, F. Qiu, M. Mazza, K. Kostarelos, and B. J. Nelson, "Controlled In Vivo Swimming of a Swarm of Bacteria-Like Microrobotic Flagella," *Adv. Mater.*, vol. 27, no. 19, pp. 2981–2988, 2015.
- [67] O. Felfoul *et al.*, "Magneto-Aerotactic Bacteria Deliver Drug-Containing Nanoliposomes to Tumour Hypoxic Regions," *Nat. Nanotechnol.*, vol. 11, no. 11, pp. 941–947, 2016.
- [68] D. Schamel *et al.*, "Nanopropellers and Their Actuation in Complex Viscoelastic Media," *ACS Nano*, vol. 8, no. 9, pp. 8794–8801, 2014.
- [69] B. J. Nelson and K. E. Peyer, "Micro- and Nanorobots Swimming in Heterogeneous Liquids," *ACS Nano*, vol. 8, no. 9, pp. 8718–8724, 2014.
- [70] Z. Li, S. Hu, and K. Cheng, "Platelets and Their Biomimetics for Regenerative Medicine and Cancer Therapies," *J. Mater. Chem. B*, vol. 6, no. 45, pp. 7354–7365, 2018.
- [71] H. Yan, D. Shao, Y.-H. Lao, M. Li, H. Hu, and K. W. Leong, "Engineering Cell Membrane-

- Based Nanotherapeutics to Target Inflammation,” *Adv. Sci.*, vol. 6, no. 15, pp. 1900605(1–24), 2019.
- [72] X. Zhen, P. Cheng, and K. Pu, “Recent Advances in Cell Membrane–Camouflaged Nanoparticles for Cancer Phototherapy,” *Small*, vol. 15, no. 1, pp. 1804105(1–19), 2019.
- [73] J. F. Schenck, “Health and Physiological Effects of Human Exposure to Whole-Body Four-Tesla Magnetic Fields during MRI,” *Ann. N. Y. Acad. Sci.*, vol. 649, no. 1, pp. 285–301, 1992.
- [74] J. F. Schenck, “Safety of Strong, Static Magnetic Fields,” *J. Magn. Reson. Imaging*, vol. 12, no. 1, pp. 2–19, 2000.
- [75] F. G. Shellock and J. V. Crues, “MR Procedures: Biologic Effects, Safety, and Patient Care,” *Radiology*, vol. 232, no. 3, pp. 635–652, 2004.
- [76] J. J. Abbott *et al.*, “How Should Microrobots Swim?,” *Int. J. Rob. Res.*, vol. 28, no. 11–12, pp. 1434–1447, 2009.
- [77] V. Iacovacci, L. Ricotti, E. Sinibaldi, G. Signore, F. Vistoli, and A. Menciassi, “An Intravascular Magnetic Catheter Enables the Retrieval of Nanoagents from the Bloodstream,” *Adv. Sci.*, vol. 5, no. 9, pp. 1800807(1–8), 2018.
- [78] D. Kim, H. Lee, S. Kwon, H. Choi, and S. Park, “Magnetic Nano-Particles Retrievable Biodegradable Hydrogel Microrobot,” *Sensors Actuators B*, vol. 289, pp. 65–77, 2019.
- [79] C. Peters, M. Hoop, S. Pané, B. J. Nelson, and C. Hierold, “Degradable Magnetic Composites for Minimally Invasive Interventions: Device Fabrication, Targeted Drug Delivery, and Cytotoxicity Tests,” *Adv. Mater.*, vol. 28, no. 3, pp. 533–538, 2016.
- [80] X. Wang *et al.*, “3D Printed Enzymatically Biodegradable Soft Helical Microswimmers,” *Adv. Funct. Mater.*, vol. 28, no. 45, pp. 1804107(1–8), 2018.
- [81] H. Ceylan, I. C. Yasa, O. Yasa, A. F. Tabak, J. Giltinan, and M. Sitti, “3D-Printed Biodegradable Microswimmer for Theranostic Cargo Delivery and Release,” *ACS Nano*, vol. 13, no. 3, pp. 3353–3362, 2019.
- [82] Z. Wu, X. Lin, X. Zou, J. Sun, and Q. He, “Biodegradable Protein-Based Rockets for Drug Transportation and Light-Triggered Release,” *ACS Appl. Mater. Interfaces*, vol. 7, no. 1, pp. 250–255, 2015.
- [83] Y. Tu, F. Peng, A. A. M. André, Y. Men, M. Srinivas, and D. A. Wilson, “Biodegradable Hybrid Stomatocyte Nanomotors for Drug Delivery,” *ACS Nano*, vol. 11, no. 2, pp. 1957–1963, 2017.
- [84] X. Yan *et al.*, “Multifunctional Biohybrid Magnetite Microrobots for Imaging-Guided Therapy,” *Sci. Robot.*, vol. 2, no. 12, p. eaaq1155(1–14), 2017.
- [85] M. De Niz, F. Spadin, M. Marti, J. V. Stein, M. Frenz, and F. Frischknecht, “Toolbox for

- In Vivo Imaging of Host–Parasite Interactions at Multiple Scales,” *Trends Parasitol.*, vol. 35, no. 3, pp. 193–212, 2019.
- [86] S. Pané *et al.*, “Imaging Technologies for Biomedical Micro- and Nanoswimmers,” *Adv. Mater. Technol.*, vol. 4, no. 4, pp. 1800575(1–16), 2019.
- [87] B. Wang, Y. Zhang, and L. Zhang, “Recent Progress on Micro- and Nano-Robots: Towards In Vivo Tracking and Localization,” *Quant. Imaging Med. Surg.*, vol. 8, no. 5, pp. 461–479, 2018.
- [88] B. Gleich and J. Weizenecker, “Tomographic Imaging Using the Nonlinear Response of Magnetic Particles,” *Nature*, vol. 435, no. 7046, pp. 1214–1217, 2005.
- [89] T. Knopp, N. Gdaniec, and M. Möddel, “Magnetic Particle Imaging: From Proof of Principle to Preclinical Applications,” *Phys. Med. Biol.*, vol. 62, no. 14, pp. R124–R178, 2017.
- [90] X. Wang, Y. Pang, G. Ku, X. Xie, G. Stoica, and L. V. Wang, “Noninvasive Laser-Induced Photoacoustic Tomography for Structural and Functional In Vivo Imaging of the Brain,” *Nat. Biotechnol.*, vol. 21, no. 7, pp. 803–806, 2003.
- [91] C. Moore and J. V. Jokerst, “Strategies for Image-Guided Therapy, Surgery, and Drug Delivery Using Photoacoustic Imaging,” *Theranostics*, vol. 9, no. 6, pp. 1550–1571, 2019.
- [92] S. Latus *et al.*, “Bimodal Intravascular Volumetric Imaging Combining OCT and MPI,” *Med. Phys.*, vol. 46, no. 3, pp. 1371–1383, 2019.
- [93] A. Aziz, M. Medina-Sánchez, J. Claussen, and O. G. Schmidt, “Real-Time Optoacoustic Tracking of Single Moving Micro-Objects in Deep Phantom and Ex Vivo Tissues,” *Nano Lett.*, vol. 19, no. 9, pp. 6612–6620, 2019.
- [94] L. Zhang, J. J. Abbott, L. Dong, B. E. Kratochvil, D. Bell, and B. J. Nelson, “Artificial Bacterial Flagella: Fabrication and Magnetic Control,” *Appl. Phys. Lett.*, vol. 94, no. 6, pp. 064107(1–3), 2009.
- [95] A. Ghosh and P. Fischer, “Controlled Propulsion of Artificial Magnetic Nanostructured Propellers,” *Nano Lett.*, vol. 9, no. 6, pp. 2243–2245, 2009.
- [96] L. Zhang *et al.*, “Characterizing the Swimming Properties of Artificial Bacterial Flagella,” *Nano Lett.*, vol. 9, no. 10, pp. 3663–3667, 2009.
- [97] H. C. Berg and R. A. Anderson, “Bacteria Swim by Rotating Their Flagellar Filaments,” *Nature*, vol. 245, no. 5425, pp. 380–382, 1973.
- [98] E. Lauga and T. R. Powers, “The Hydrodynamics of Swimming Microorganisms,” *Reports Prog. Phys.*, vol. 72, no. 9, pp. 096601(1–36), 2009.
- [99] E. E. Keaveny, S. W. Walker, and M. J. Shelley, “Optimization of Chiral Structures for Microscale Propulsion,” *Nano Lett.*, vol. 13, no. 2, pp. 531–537, 2013.
- [100] Y. Man and E. Lauga, “The Wobbling-to-Swimming Transition of Rotated Helices,” *Phys.*

- Fluids*, vol. 25, no. 7, pp. 071904(1–16), 2013.
- [101] K. I. Morozov and A. M. Leshansky, “The Chiral Magnetic Nanomotors,” *Nanoscale*, vol. 6, no. 3, pp. 1580–1588, 2014.
 - [102] B. Bet, G. Boosten, M. Dijkstra, and R. Van Roij, “Efficient Shapes for Microswimming: From Three-Body Swimmers to Helical Flagella,” *J. Chem. Phys.*, vol. 146, no. 8, pp. 084904(1–8), 2017.
 - [103] T. Honda, K. I. Arai, and K. Ishiyama, “Micro Swimming Mechanisms Propelled by External Magnetic Fields,” *IEEE Trans. Magn.*, vol. 32, no. 5, pp. 5085–5087, 1996.
 - [104] D. Walker, M. Kübler, K. I. Morozov, P. Fischer, and A. M. Leshansky, “Optimal Length of Low Reynolds Number Nanopropellers,” *Nano Lett.*, vol. 15, no. 7, pp. 4412–4416, 2015.
 - [105] A. Ghosh, D. Paria, H. J. Singh, P. L. Venugopalan, and A. Ghosh, “Dynamical Configurations and Bistability of Helical Nanostructures Under External Torque,” *Phys. Rev. E*, vol. 86, no. 3, pp. 031401(1–5), 2012.
 - [106] F. Bachmann, K. Bente, A. Codutti, and D. Faivre, “Using Shape Diversity on the Way to New Structure-Function Designs for Magnetic Micropropellers,” *Phys. Rev. Appl.*, vol. 11, no. 3, pp. 034039(1–24), 2019.
 - [107] E. M. Purcell, “The Efficiency of Propulsion by a Rotating Flagellum,” *Proc. Natl. Acad. Sci.*, vol. 94, no. 21, pp. 11307–11311, 1997.
 - [108] S. Tottori, L. Zhang, F. Qiu, K. K. Krawczyk, A. Franco-Obregón, and B. J. Nelson, “Magnetic Helical Micromachines: Fabrication, Controlled Swimming, and Cargo Transport,” *Adv. Mater.*, vol. 24, no. 6, pp. 811–816, 2012.
 - [109] W. Gao *et al.*, “Bioinspired Helical Microswimmers Based on Vascular Plants,” *Nano Lett.*, vol. 14, no. 1, pp. 305–310, 2014.
 - [110] P. Serrano, D. Decanini, L. Leroy, L. Couraud, and G. Hwang, “Multiflagella Artificial Bacteria for Robust Microfluidic Propulsion and Multimodal Micromanipulation,” *Microelectron. Eng.*, vol. 195, pp. 145–152, 2018.
 - [111] K. E. Peyer, E. Siringil, L. Zhang, and B. J. Nelson, “Magnetic Polymer Composite Artificial Bacterial Flagella,” *Bioinspiration and Biomimetics*, vol. 9, no. 4, pp. 046014(1–10), 2014.
 - [112] A. W. Mahoney, N. D. Nelson, K. E. Peyer, B. J. Nelson, and J. J. Abbott, “Behavior of Rotating Magnetic Microrobots Above the Step-Out Frequency with Application to Control of Multi-Microrobot Systems,” *Appl. Phys. Lett.*, vol. 104, no. 14, pp. 144101(1–5), 2014.
 - [113] A. Oulmas, N. Andreff, and S. Régnier, “3D Closed-Loop Swimming at Low Reynolds

- Numbers,” *Int. J. Rob. Res.*, vol. 37, no. 11, pp. 1359–1375, 2018.
- [114] D. Gong *et al.*, “Controlled Propulsion of Wheel-Shape Flaky Microswimmers Under Rotating Magnetic Fields,” *Appl. Phys. Lett.*, vol. 114, no. 12, pp. 123701(1–5), 2019.
- [115] J. Liu, T. Xu, Y. Guan, X. Yan, C. Ye, and X. Wu, “Swimming Characteristics of Bioinspired Helical Microswimmers Based on Soft Lotus-Root Fibers,” *Micromachines*, vol. 8, no. 12, pp. 349(1–20), 2017.
- [116] B. E. Kratochvil *et al.*, “MiniMag: A Hemispherical Electromagnetic System for 5-DOF Wireless Micromanipulation,” in *Experimental Robotics. Springer Tracts in Advanced Robotics*, vol. 79, Springer, Germany, 2014, pp. 317–329.
- [117] A. Barbot, D. Decanini, and G. Hwang, “On-Chip Microfluidic Multimodal Swimmer Toward 3D Navigation,” *Sci. Rep.*, vol. 6, pp. 19041(1–8), 2016.
- [118] P. L. Venugopalan, R. Sai, Y. Chandorkar, B. Basu, S. Shivashankar, and A. Ghosh, “Conformal Cytocompatible Ferrite Coatings Facilitate the Realization of a Nanovoyager in Human Blood,” *Nano Lett.*, vol. 14, no. 4, pp. 1968–1975, 2014.
- [119] M. Guix, C. C. Mayorga-Martinez, and A. Merkoçi, “Nano/Micromotors in (Bio)chemical Science Applications,” *Chem. Rev.*, vol. 114, no. 12, pp. 6285–6322, 2014.
- [120] C. Harvey, “The Speed of Human Spermatozoa and the Effect on It of Various Diluents, with Some Preliminary Observations on Clinical Material,” *J. Reprod. Fertil.*, vol. 1, no. 1, pp. 84–95, 1960.
- [121] H. Chang, B. J. Kim, Y. S. Kim, S. S. Suarez, and M. Wu, “Different Migration Patterns of Sea Urchin and Mouse Sperm Revealed by a Microfluidic Chemotaxis Device,” *PLoS One*, vol. 8, no. 4, p. e60587(1–8), 2013.
- [122] P. J. Vach, P. Fratzl, S. Klumpp, and D. Faivre, “Fast Magnetic Micropropellers with Random Shapes,” *Nano Lett.*, vol. 15, no. 10, pp. 7064–7070, 2015.
- [123] T. O. Tasci, P. S. Herson, K. B. Neeves, and D. W. M. Marr, “Surface-Enabled Propulsion and Control of Colloidal Microwheels,” *Nat. Commun.*, vol. 7, pp. 10225(1–6), 2016.
- [124] K. Ishimoto and E. A. Gaffney, “Mechanical Tuning of Mammalian Sperm Behaviour by Hyperactivation, Rheology and Substrate Adhesion: A Numerical Exploration,” *J. R. Soc. Interface*, vol. 13, no. 124, pp. 20160633(1–11), 2016.
- [125] G. E. Moore, “Cramming More Components onto Integrated Circuits,” *Electronics*, vol. 38, no. 8, pp. 114–117, 1965.
- [126] C. A. Mack, “Fifty Years of Moore’s Law,” *IEEE Trans. Semicond. Manuf.*, vol. 24, no. 2, pp. 202–207, 2011.
- [127] R. P. Feynman, “There’s Plenty of Room at the Bottom,” *Eng. Sci.*, vol. 23, no. 5, pp. 22–26, 1960.

- [128] O. G. Schmidt and K. Eberl, "Thin Solid Films Roll Up into Nanotubes," *Nature*, vol. 410, no. 6842, p. 168, 2001.
- [129] S. V. Golod, V. Y. Prinz, V. I. Mashanov, and A. K. Gutakovsky, "Fabrication of Conducting GeSi/Si Micro- and Nanotubes and Helical Microcoils," *Semicond. Sci. Technol.*, vol. 16, no. 3, pp. 181–185, 2001.
- [130] K. Robbie, M. J. Brett, and A. Lakhtakia, "Chiral Sculptured Thin Films," *Nature*, vol. 384, no. 6610, p. 616, 1996.
- [131] M. J. Brett and M. M. Hawkeye, "New Materials at a Glance," *Science*, vol. 319, no. 5867, pp. 1192–1193, 2008.
- [132] J. Li *et al.*, "Template Electrosynthesis of Tailored-Made Helical Nanoswimmers," *Nanoscale*, vol. 6, no. 16, pp. 9415–9420, 2014.
- [133] X. Wang *et al.*, "Facile Fabrication of Magnetic Microrobots Based on Spirulina Templates for Targeted Delivery and Synergistic Chemo-Photothermal Therapy," *ACS Appl. Mater. Interfaces*, vol. 11, no. 5, pp. 4745–4756, 2019.
- [134] W. Wang *et al.*, "Controllable Microfluidic Fabrication of Microstructured Materials from Nonspherical Particles to Helices," *Macromol. Rapid Commun.*, vol. 38, no. 23, pp. 1700429(1–7), 2017.
- [135] Y. Yu, L. Shang, W. Gao, Z. Zhao, H. Wang, and Y. Zhao, "Microfluidic Lithography of Bioinspired Helical Micromotors," *Angew. Chemie - Int. Ed.*, vol. 56, no. 40, pp. 12127–12131, 2017.
- [136] H.-B. Sun and S. Kawata, "Two-Photon Photopolymerization and 3D Lithographic Microfabrication," *Adv. Polym. Sci.*, vol. 170, pp. 169–273, 2004.
- [137] X. Zhou, Y. Hou, and J. Lin, "A Review on the Processing Accuracy of Two-Photon Polymerization," *AIP Adv.*, vol. 5, no. 3, pp. 030701(1–22), 2015.
- [138] M. G. Guney and G. K. Fedder, "Estimation of Line Dimensions in 3D Direct Laser Writing Lithography," *J. Micromechanics Microengineering*, vol. 26, no. 10, pp. 105011(1–10), 2016.
- [139] S. Wang *et al.*, "Sub-10-nm Suspended Nano-Web Formation by Direct Laser Writing," *Nano Futur.*, vol. 2, no. 2, pp. 025006(1–9), 2018.
- [140] L. Schwarz, M. Medina-Sánchez, and O. G. Schmidt, "Easily Scalable High Speed Magnetic Micropropellers," in *2016 International Conference on Manipulation, Automation and Robotics at Small Scales (MARSS)*, 2016, pp. 205–208.
- [141] J. M. Sims, *Clinical Notes on Uterine Surgery. With Special Reference to the Management of the Sterile Condition*. Wood, USA, 1866.
- [142] K. W. Swanson, "Adultery by Doctor: Artificial Insemination, 1890-1945," *Chic. Kent.*

- Law Rev.*, vol. 87, no. 2, pp. 591–633, 2012.
- [143] “Clinical Notes on Uterine Surgery. With Special Reference to the Management of the Sterile Condition - Bibilographical Record,” in *The British and Foreign Medico-Chirurgical Review*, vol. 39, no. 77, 1867, pp. 143–147.
 - [144] M. C. Inhorn and P. Patrizio, “Infertility Around the Globe: New Thinking on Gender, Reproductive Technologies and Global Movements in the 21st Century,” *Hum. Reprod. Update*, vol. 21, no. 4, pp. 411–426, 2015.
 - [145] M. Aboulghar *et al.*, “Intrauterine Insemination,” *Hum. Reprod. Update*, vol. 15, no. 3, pp. 265–277, 2009.
 - [146] P. C. Steptoe and R. G. Edwards, “Birth After the Reimplantation of a Human Embryo,” *Lancet*, vol. 312, no. 8085, p. 366, 1978.
 - [147] G. Palermo, H. Joris, P. Devroey, and A. C. Van Steirteghem, “Pregnancies After Intracytoplasmic Injection of Single Spermatozoon into an Oocyte,” *Lancet*, vol. 340, no. 8810, pp. 17–18, 1992.
 - [148] D. Rizos, F. Ward, P. Duffy, M. P. Boland, and P. Lonergan, “Consequences of Bovine Oocyte Maturation, Fertilization or Early Embryo Development In Vitro Versus In Vivo: Implications for Blastocyst Yield and Blastocyst Quality,” *Mol. Reprod. Dev.*, vol. 61, no. 2, pp. 234–248, 2002.
 - [149] E. Van Royen *et al.*, “Characterization of a Top Quality Embryo, a Step Towards Single-Embryo Transfer,” *Hum. Reprod.*, vol. 14, no. 9, pp. 2345–2349, 1999.
 - [150] H. B. Croxatto and M.-E. S. Ortiz, “Egg Transport in the Fallopian Tube,” *Gynecol. Invest.*, vol. 6, no. 3–4, pp. 215–225, 1975.
 - [151] P. Coy, F. A. García-Vázquez, P. E. Visconti, and M. Avilés, “Roles of the Oviduct in Mammalian Fertilization,” *Reproduction*, vol. 144, no. 6, pp. 649–660, 2012.
 - [152] P. Devroey, P. Braeckmans, J. Smits, L. Van Waesberghe, A. Wisanto, and A. Van Steirteghem, “Pregnancy After Translaparoscopic Zygote Intrafallopian Transfer in a Patient with Sperm Antibodies,” *Lancet*, vol. 1, no. 8493, p. 1329, 1986.
 - [153] A. Vorrsselmans, P. Platteau, A. De Vos, C. Albano, A. Van Steirteghem, and P. Devroey, “Comparison of Transfers to Fallopian Tubes or Uterus After ICSI,” *Reprod. Biomed. Online*, vol. 7, no. 1, pp. 82–85, 2003.
 - [154] O. Ozkaya *et al.*, “Comparison of Tubal Transfer and Transcervical Uterine Embryo Transfer of Immediate Injected Oocytes and 2-3 Days Old Cultured Embryos,” *Geburtshilfe Frauenheilkd.*, vol. 66, no. 4, pp. 377–382, 2006.
 - [155] A. Alleyassin, A. Mahmoodan, M. Aghahosseini, L. Safdarian, and H. S. Saeidabadi, “Comparison of Immediate and Delayed Transfer of Micro-Injected Oocytes into Fallopian

- Tubes: A Prospective, Randomized Clinical Trial,” *Int. J. Fertil. Steril.*, vol. 2, no. 2, pp. 86–89, 2008.
- [156] L. Schwarz, M. Medina-Sanchez, and O. G. Schmidt, “Magnetic micromotors for resilient and reversible cargo transport in and between microfluidic environments,” in *2019 International Conference on Manipulation, Automation and Robotics at Small Scales (MARSS)*, 2019, pp. 169–173.
- [157] L. Schwarz, D. D. Karnaushenko, F. Hebenstreit, R. Naumann, O. G. Schmidt, and M. Medina-Sánchez, “A Rotating Spiral Micromotor for Noninvasive Zygote Transfer,” *Adv. Sci.*, vol. 7, no. 18, pp. 2000843(1–14), 2020.
- [158] J. M. Cummins and P. F. Woodall, “On Mammalian Sperm Dimensions,” *J. Reprod. Fertil.*, vol. 75, no. 1, pp. 153–175, 1985.
- [159] E. A. Gaffney, H. Gadêlha, D. J. Smith, J. R. Blake, and J. C. Kirkman-Brown, “Mammalian Sperm Motility: Observation and Theory,” *Annu. Rev. Fluid Mech.*, vol. 43, no. 1, pp. 501–528, 2011.
- [160] R. E. Brannigan and L. I. Lipshultz, “Sperm Transport and Capacitation,” *Glob. Libr. Women’s Med.*, pp. 1-13 (ISSN: 1756-2228), 2008.
- [161] S. S. Suarez, “Mammalian Sperm Interactions with the Female Reproductive Tract,” *Cell Tissue Res.*, vol. 363, no. 1, pp. 185–194, 2016.
- [162] A. Salustri, M. Yanagishita, C. B. Underhill, T. C. Laurent, and V. C. Hascall, “Localization and Synthesis of Hyaluronic Acid in the Cumulus Cells and Mural Granulosa Cells of the Preovulatory Follicle,” *Dev. Biol.*, vol. 151, no. 2, pp. 541–551, 1992.
- [163] P. M. Wassarman, “The Biology and Chemistry of Fertilization,” *Science*, vol. 235, no. 4788, pp. 553–560, 1987.
- [164] S. S. Suarez and A. A. Pacey, “Sperm Transport in the Female Reproductive Tract,” *Hum. Reprod. Update*, vol. 12, no. 1, pp. 23–37, 2006.
- [165] S. S. Suarez, “Regulation of Sperm Storage and Movement in the Mammalian Oviduct,” *Int. J. Dev. Biol.*, vol. 52, no. 5–6, pp. 455–462, 2008.
- [166] J. M. Bedford and H. H. Kim, “Cumulus Oophorus as a Sperm Sequestering Device, In Vivo,” *J. Exp. Zool.*, vol. 265, no. 3, pp. 321–328, 1993.
- [167] S. Tanghe, A. Van Soom, H. Nauwynck, M. Coryn, and A. De Kruif, “Minireview: Functions of the Cumulus Oophorus During Oocyte Maturation, Ovulation, and Fertilization,” *Mol. Reprod. Dev.*, vol. 61, no. 3, pp. 414–424, 2002.
- [168] Y. Lin, K. Mahan, W. F. Lathrop, D. G. Myles, and P. Primakoff, “A Hyaluronidase Activity of the Sperm Plasma Membrane Protein PH-20 Enables Sperm to Penetrate the Cumulus

- Cell Layer Surrounding the Egg,” *J. Cell Biol.*, vol. 125, no. 5, pp. 1157–1163, 1994.
- [169] U. B. Kaupp and T. Strünker, “Signaling in Sperm: More Different than Similar,” *Trends Cell Biol.*, vol. 27, no. 2, pp. 101–109, 2017.
- [170] J. Liu, Y.-L. Tsai, E. Katz, G. Compton, J. E. Garcia, and T. A. Baramaki, “High Fertilization Rate Obtained After Intracytoplasmic Sperm Injection With 100% Nonmotile Spermatozoa Selected by Using a Simple Modified Hypo-Osmotic Swelling Test,” *Fertil. Steril.*, vol. 68, no. 2, pp. 373–375, 1997.
- [171] C. Ortega, G. Verheyen, D. Raick, M. Camus, P. Devroey, and H. Tournaye, “Absolute Asthenozoospermia and ICSI: What Are the Options?,” *Hum. Reprod. Update*, vol. 17, no. 5, pp. 684–692, 2011.
- [172] A. Barros, M. Sousa, C. Oliveira, J. Silva, V. Almeida, and J. Beires, “Pregnancy and Birth After Intracytoplasmic Sperm Injection with Totally Immotile Sperm Recovered from the Ejaculate,” *Fertil. Steril.*, vol. 67, no. 6, pp. 1091–1094, 1997.
- [173] S. Kahraman, A. Z. Işık, K. Vicdan, S. Özgür, and O. D. Özgün, “A Healthy Birth After Intracytoplasmic Sperm Injection by Using Immotile Testicular Spermatozoa in a Case with Totally Immotile Ejaculated Spermatozoa Before and After Percoll Gradients,” *Hum. Reprod.*, vol. 12, no. 2, pp. 292–293, 1997.
- [174] M. Amiji and K. Park, “Prevention of Protein Adsorption and Platelet Adhesion on Surfaces by PEO/PPO/PEO Triblock Copolymers,” *Biomaterials*, vol. 13, no. 10, pp. 682–692, 1992.
- [175] S. L. Percival, R. Chen, D. Mayer, and A.-M. Salisbury, “Mode of Action of Poloxamer-Based Surfactants in Wound Care and Efficacy on Biofilms,” *Int. Wound J.*, vol. 15, no. 5, pp. 749–755, 2018.
- [176] A. K. Boardman, S. Allison, A. Sharon, and A. F. Sauer-Budge, “Comparison of Anti-Fouling Surface Coatings for Applications in Bacteremia Diagnostics,” *Anal. Methods*, vol. 5, no. 1, pp. 273–280, 2013.
- [177] S. Schlie *et al.*, “Three-Dimensional Cell Growth on Structures Fabricated from ORMOCER® by Two-Photon Polymerization Technique,” *J. Biomater. Appl.*, vol. 22, no. 3, pp. 275–287, 2007.
- [178] J. Eckert and H. Niemann, “In Vitro Maturation, Fertilization and Culture to Blastocysts of Bovine Oocytes in Protein-Free Media,” *Theriogenology*, vol. 43, no. 7, pp. 1211–1225, 1995.
- [179] M.-A. Sirard and K. Coenen, “In Vitro Maturation and Embryo Production in Cattle,” in *Nuclear Transfer Protocols. Methods in Molecular Biology*, vol. 348, no. 3, Humana Press, USA, 2006, pp. 35–42.
- [180] “In Vitro Production of Bovine Embryos,” *P. J. Hansen Laboratory, Department of Animal*

- Sciences, University of Florida*, www.animal.ifas.ufl.edu/hansen/ (accessed: Sep 2020).
- [181] T. Takeo and N. Nakagata, "Reduced Glutathione Enhances Fertility of Frozen/Thawed C57BL/6 Mouse Sperm After Exposure to Methyl-Beta-Cyclodextrin1," *Biol. Reprod.*, vol. 85, no. 5, pp. 1066–1072, 2011.
 - [182] "Reproductive Engineering Techniques in Mice," *Center for Animal Resources and Development, Kumamoto University*, card.medic.kumamoto-u.ac.jp/card/english/sigen/manual/onlinemanual.html (accessed: Sep 2020).
 - [183] W. M. S. Russell and R. L. Burch, *The Principles of Humane Experimental Technique*. Methuen, UK, 1959.
 - [184] R. S. Jeyendran, H. H. Van der Ven, M. Perez-Pelaez, B. G. Crabo, and L. J. D. Zaneveld, "Development of an Assay to Assess the Functional Integrity of the Human Sperm Membrane and Its Relationship to Other Semen Characteristics," *J. Reprod. Fertil.*, vol. 70, no. 1, pp. 219–228, 1984.
 - [185] C. B. Smikle and P. J. Turek, "Hypo-Osmotic Swelling Can Accurately Assess the Viability of Nonmotile Sperm," *Mol. Reprod. Dev.*, vol. 47, no. 2, pp. 200–203, 1997.
 - [186] R. F. Casper, J. S. Meriano, K. A. Jarvi, L. Cowan, and M. L. Lucato, "The Hypo-Osmotic Swelling Test for Selection of Viable Sperm for Intracytoplasmic Sperm Injection in Men with Complete Asthenozoospermia," *Fertil. Steril.*, vol. 65, no. 5, pp. 972–976, 2016.
 - [187] J. Schindelin *et al.*, "Fiji: An Open-Source Platform for Biological-Image Analysis," *Nat. Methods*, vol. 9, no. 7, pp. 676–682, 2012.
 - [188] K. E. Peyer, F. Qiu, L. Zhang, and B. J. Nelson, "Movement of Artificial Bacterial Flagella in Heterogeneous Viscous Environments at the Microscale," in *2012 IEEE/RSJ International Conference on Intelligent Robots and Systems*, 2012, no. 13195433, pp. 2553–2558.
 - [189] J. Kestin, M. Sokolov, and W. A. Wakeham, "Viscosity of Liquid Water in the Range -8°C to 150°C," *J. Phys. Chem. Ref. Data*, vol. 7, no. 3, pp. 941–948, 1978.
 - [190] P. J. Vach, S. Klumpp, and D. Faivre, "Steering Magnetic Micropropellers Along Independent Trajectories," *J. Phys. D. Appl. Phys.*, vol. 49, no. 6, pp. 65003(1–7), 2015.
 - [191] V. Magdanz, M. Medina-Sánchez, Y. Chen, M. Guix, and O. G. Schmidt, "How to Improve Spermbot Performance," *Adv. Funct. Mater.*, vol. 25, no. 18, pp. 2763–2770, 2015.
 - [192] N. S. Manam *et al.*, "Study of Corrosion in Biocompatible Metals for Implants: A Review," *J. Alloys Compd.*, vol. 701, pp. 698–715, 2017.
 - [193] Y.-H. Song, M.-K. Kim, E.-J. Park, H.-J. Song, K. J. Anusavice, and Y.-J. Park, "Cytotoxicity of Alloying Elements and Experimental Titanium Alloys by WST-1 and Agar Overlay Tests," *Dent. Mater.*, vol. 30, no. 9, pp. 977–983, 2014.

- [194] E. C. Jensen, "Use of Fluorescent Probes: Their Effect on Cell Biology and Limitations," *Anat. Rec. - Adv. Integr. Anat. Evol. Biol.*, vol. 295, no. 12, pp. 2031–2036, 2012.
- [195] L. Yin, W. Wang, S. Wang, F. Zhang, S. Zhang, and N. Tao, "How Does Fluorescent Labeling Affect the Binding Kinetics of Proteins with Intact Cells?," *Biosens. Bioelectron.*, vol. 66, pp. 412–416, 2015.
- [196] A. Rouen *et al.*, "Potential Selection of Genetically Balanced Spermatozoa Based on the Hypo-Osmotic Swelling Test in Chromosomal Rearrangement Carriers," *Reprod. Biomed. Online*, vol. 35, no. 4, pp. 372–378, 2017.
- [197] J. O. B. Mendes Jr., P. D. Burns, J. F. De La Torre-Sanchez, and G. E. Seidel Jr., "Effect of Heparin on Cleavage Rates and Embryo Production with Four Bovine Sperm Preparation Protocols," *Theriogenology*, vol. 60, no. 2, pp. 331–340, 2003.
- [198] S. Ghosh and A. Ghosh, "Mobile Nanotweezers for Active Colloidal Manipulation," *Sci. Robot.*, vol. 3, no. 14, p. eaaq0076(1-8), 2018.
- [199] S. Fusco *et al.*, "An Integrated Microrobotic Platform for On-Demand, Targeted Therapeutic Interventions," *Adv. Mater.*, vol. 26, no. 6, pp. 952–957, 2014.
- [200] F. Ongaro *et al.*, "Autonomous Planning and Control of Soft Untethered Grippers in Unstructured Environments," *J. Micro-Bio Robot.*, vol. 12, no. 1–4, pp. 45–52, 2017.
- [201] P. J. Vach and D. Faivre, "The Triathlon of Magnetic Actuation: Rolling, Propelling, Swimming with a Single Magnetic Material," *Sci. Rep.*, vol. 5, pp. 9364(1–6), 2015.
- [202] L. Zhu, E. Lauga, and L. Brandt, "Low-Reynolds-Number Swimming in a Capillary Tube," *J. Fluid Mech.*, vol. 726, pp. 285–311, 2013.
- [203] M. A. M. M. Ferraz *et al.*, "Improved Bovine Embryo Production in an Oviduct-on-a-Chip System: Prevention of Poly-Spermic Fertilization and Parthenogenic Activation," *Lab Chip*, vol. 17, no. 5, pp. 905–916, 2017.

List of Figures and Tables

Figure 1	The concept of micromotor-assisted fertilization	8
Figure 2.1	The size of micromotors	12
Figure 2.2	Principles of 2PA and 2PP	22
Figure 2.3	Principal anatomy of the male and female gamete	26
Figure 3.1	Examples of fabricated microfluidic channel platforms	32
Figure 3.2	Programmed micromotor structures	34
Figure 3.3	Two different setups for micromotor actuation with rotating magnetic fields and live observation and recording by optical microscopy	46
Figure 4.1	Helical micromotor design	51
Figure 4.2	Basic helix propulsion experiments	52
Figure 4.3	Helical micromotor performance	54
Figure 4.4	Capture and release of a <i>bovine</i> sperm cell	56
Figure 4.5	Transport of a captured <i>bovine</i> sperm cell	56
Figure 4.6	Propulsion performance of microhelices before and after sperm coupling	57
Figure 4.7	Delivery of an immotile <i>bovine</i> sperm cell to the oocyte	58
Figure 4.8	Sperm assessment	61
Figure 4.9	Sperm viability assay	63
Figure 4.10	Penetrating the cumulus oophorus	64
Figure 5.1	Micromotor designs for oocyte/zygote manipulation	68
Figure 5.2	Orientation of a spiral-type micromotor	70
Figure 5.3	Propulsion performance of micromotors in different environments	71
Figure 5.4	Coupling of spiral-type micromotors with cellular cargo	75
Figure 5.5	Transport of zygotes through microchannels	77
Figure 5.6	Propulsion performance of zygote-carrying micromotors before and after cargo coupling	78
Figure 5.7	Transfer of a cargo-loaded spiral between different environments	80
Figure 5.8	Embryo development and the artificial oviduct	82
Table 1	Metal multilayer coatings of applied micromotors	36
Table 2	Sperm cell medium (SpTALP)	39
Table 3	Transport saline solution	40
Table 4	Slicing solution	40
Table 5	TCMair	40
Table 6	ICM culture medium	41
Table 7	IVF culture medium	42
Table 8	Albumin-pyruvate-gentamicin supplement	42
Table 9	Hypotaurine-heparin-epinephrine supplement	42
Table 10	IVC medium for embryo development	43
Table 11	Co-incubation of sperm in 50 μ l HOS test medium with different materials	44

List of Abbreviations and Terms

2D	two-dimensional
2PA	two-photon absorption
2PP	two-photon polymerization
3D	three-dimensional
ART	assisted reproductive technology
asthenozoospermia	reduced sperm motility
Au	gold
blps	body lengths per second
bovine	of cattle, pertaining to cattle
B	magnetic flux density
BSA	bovine serum albumin
COC	cumulus-oocyte complex
CO ₂	carbon dioxide (gas)
cumulus	cumulus oophorus, cluster of cumulus cells around the oocyte
DI water	deionized water
DLW	direct laser writing
DNA	deoxyribonucleic acid
E.coli	Escherichia coli
eSET	elective single embryo transfer
ET	embryo transfer
f	rotation frequency
FDA	fluorescein diacetate
Fe	iron
Fig.	figure
FITC-PNA	fluorescein isothiocyanate-labeled peanut agglutinin
FVP	frequency-velocity-profile
fps	frames per second
GWL	general writing language
HOS	hypoosmotic swelling
ICSI	intracytoplasmic sperm injection
in situ	on site, i.e. within the sample
in vitro	in the glass, i.e. in the laboratory
in vivo	in the living, i.e. in the organism
IP-Dip	Nanoscribe photoresist IP-Dip for Dip-in laser lithography
IR	infrared
IVC	in vitro culture
IVF	in vitro fertilization
IVM	in vitro maturation
KSOM	EmbryoMax® KSOM mouse embryo medium

LysoTracker blue	LysoTracker® Blue DND-22 blue fluorescent dye
M2	M2 mouse embryo medium
MCM	methyl cellulose-containing (water-based) medium
MDCK cells	Madin-Darby canine kidney cells
MEMS	micro-electro-mechanical systems
MiniMag	Magnebotix magnetic field generator MFG-100-i
MRI	magnetic resonance imaging
murine	of the mouse, pertaining to the mouse
Nanoscribe	Nanoscribe Photonic Professional GT 3D printer
Ni	nickel
oligozoospermia	few spermatozoa in semen
Ormocomp	Micro Resist Technology photoresist Ormocomp®
OVF	oviduct fluid (centrifuged)
Re	the Reynolds number
RMF	rotating magnetic field
rpm	revolutions per minute
RT	room temperature
PBS	phosphate-buffered saline solution
parafilm	Parafilm® M polyolefin film
PEG	poly(ethylene glycol)
PEG-thiol	poly(ethylene glycol) methyl ether thiol
PDMS	polydimethylsiloxane
PI	propidium iodide
PLL-g-PEG	poly(L-lysine)-grafted-poly(ethylene glycol)
pluronic solution	Pluronic® F-127 poloxamer solution
PMMA	poly(methyl methacrylate)
PS	polystyrene
PTFE	polytetrafluorethylene
SEM	scanning electron microscopy
SiO ₂	silicon dioxide
spermbot	sperm-hybrid micromotor, i.e. sperm cell + synthetic component
SpTALP	modified Tyrode's solution, i.e. sperm cell medium
SU-8	MicroChem epoxy-based photoresist SU-8 10
SYBR14	SYBR® 14 green fluorescent cyanine dye
Ta	tantalum
TCMair	buffered tissue culture medium, based on TCM199
Ti	titanium
UV	ultraviolet
voxel	volume element
ZIFT	zygote intrafallopian transfer
zona pellucida	glycoprotein layer around the oocyte (atop of the cell membrane)

Theses

1. Magnetic micromotors with arbitrary shapes can be fabricated by direct laser writing to capture and transport microscopic cargo.
2. Magnetic microhelices can capture, transport, and release individual non-motile sperm cells to counteract asthenozoospermia.
3. The viability of a transported sperm cell can be monitored by implementing hypoosmotic swelling.
4. *Bovine* sperm cells can be delivered by microhelices to adhere to the zona pellucida of a denuded *bovine* oocyte.
5. Magnetic microhelices cannot penetrate the cumulus oophorus of a *bovine* oocyte and thus require biochemical functionalization.
6. The application of only ten micromotor-assisted sperm cells can be sufficient to achieve micromotor-assisted fertilization *in vivo*.
7. Magnetic helices and spirals can capture, transport, and release individual oocytes and zygotes towards non-invasive embryo transfer after IVF.
8. Spiral-type micromotors can capture cargo in a safe and resilient manner with a reversible coupling mechanism that withstands macroscopic operations.
9. A 3D-tiltable rotating magnetic field is sufficient to actuate and control micromotor propulsion and cargo capture, transport and release.
10. Spiral-type micromotors outperform established helical micromotors regarding cargo transport in water-based media and high-viscosity fluid.
11. 3D culture of oviduct epithelial cells can advance *in vitro* experiments towards micromotor-assisted zygote intrafallopian transfer and embryo development.
12. Magnetic micromotors as untethered transporters of male and female gametes can transfer IVF approaches to *in vivo* applications and thus advance and compliment modern assisted reproductive technology.

Selbstständigkeitserklärung

Ich erkläre, dass ich die vorliegende Arbeit selbstständig, ohne unzulässige Hilfe Dritter und nur unter Verwendung der angegebenen Literatur und Hilfsmittel angefertigt habe. Die aus fremden Quellen direkt oder indirekt übernommenen Gedanken sind als solche kenntlich gemacht.

Die Arbeit wurde unter Betreuung von Prof. Dr. Oliver G. Schmidt und Dr. Mariana Medina Sánchez am Institut für Integrative Nanowissenschaften des Leibniz-Instituts für Festkörper- und Werkstoffforschung in Dresden erarbeitet.

Ich erkläre, nicht bereits früher oder gleichzeitig bei anderen Hochschulen oder an dieser Universität ein Promotionsverfahren beantragt zu haben. Die Arbeit wurde bisher weder im Inland noch im Ausland in gleicher oder ähnlicher Form einer anderen Prüfungsbehörde vorgelegt.

Ich erkläre, diese Angaben wahrheitsgemäß gemacht zu haben und erkenne die Promotionsordnung der Fakultät für Naturwissenschaften der Technischen Universität Chemnitz vom 31. Januar 2011 an.

Datum, Unterschrift

Acknowledgments

There are those who know how much they contributed to the accomplishment of this dissertation, and those who are not aware of how much they helped me in this time. Belonging to the former, I would like to express my gratitude to my doctorate supervisor Oliver G. Schmidt, who conceived and guided the entire project and laid the foundation for my professional life as a PhD student, providing valuable advice, guidance, and support throughout the last five years. In the same way, I am much obliged to my supervisor and group leader Mariana Medina-Sánchez, who I want to thank for the time, knowledge, enthusiasm, wits, and fun that she shared with me as a boss, colleague, and friend. Especially in my first year, I benefitted greatly from working closely together with her in the laboratory, yet also in the second half of my project, her ideas and suggestions were an indispensable support, both professionally and personally. Moreover, I also want to thank Benjamin Friedrich for providing his expertise as a reviewer of this thesis. Regarding the presented experimental work, I am much obliged to the following colleagues: Franziska Hebenstreit for help with cell culture and in vitro fertilization, fluorescence measurements, media preparations, and many more works in the laboratory, Haifeng Xu for SEM images and Nanoscribe design inspirations, Friedrich Striggow for SEM images, oviduct fluid preparation and rheology measurements, Mariana Medina-Sánchez for help with various protocols and experimental routines regarding lithography, surface functionalization, microchannel fabrication, and in vitro fertilization, the technicians Sandra Nestler, Martin Bauer, Cornelia Krien, Ronny Engelhard, Carol Schmidt, and Cindy Kupka, for help with metal coatings and further technical support, Dmitriy Karnaushenko and Vladimir Fomin for simulations of micromotor hydrodynamics, the workshop engineers Torsten Seidemann, Hartmut Siegel, and Uwe Biscop for manufacturing and implementing the Helmholtz setup, various sample holders, and sample molds, the student assistants Fabian Mehner and Sharath Tippur Narayana Iyengar for valuable help with various experiments, the former group members Anne K. Meyer and Britta Koch for help with cell culture and in vitro fertilization, and the current group members Raphael Doineau, Raffael Herzer, and Azaam Aziz, as well as all the aforementioned people, for continuous support and fruitful discussions. Valuable discussions were also enjoyed with Christian Niclaas Saggau, Robert Keil, Veronika Magdanz, Maria Guix, Nicolas Perez Rodriguez, and insights on the biology of reproduction from Jennifer Schön of the Leibniz Institute for Farm Animal Biology, Katarina Jewgenow of the Leibniz Institute for Zoo and Wildlife Research, Dunja Baston-Büst of the Düsseldorf University Hospital, and Ronald Naumann of the Max Planck Institute of Molecular

Cell Biology and Genetics are much appreciated. On top of this, I am grateful that many of the mentioned co-workers and colleagues also enriched my life in Dresden during these five year on a personal level, for example Franziska, Friedrich, Raffael, Christian, and Haifeng, to name just a few. Then, there is the important group of people who (thankfully!) never bothered much with (my) science and as such constitutes an indispensable part of my life that also helped me to accomplish this doctorate, for which I cannot thank them enough. These are, of course, my parents, my brothers, my sister and her family, and my close friends Stefan, Julia, Matthias, Johannes, Florian, Doreen, and Anna. Without these people, especially without my family, I would have lost a much bigger part of my mind for sure. Thank you.

List of Publications

- **Lukas Schwarz**, Dmitriy D. Karnaushenko, Franziska Hebenstreit, Ronald Naumann, Oliver G. Schmidt, and Mariana Medina-Sánchez*, "A Rotating Spiral Micromotor for Noninvasive Zygote Transfer," *Advanced Science*, vol. 7, no. 18, pp. 2000843(1–14), 2020.
- **Lukas Schwarz**, Mariana Medina-Sánchez*, and Oliver G. Schmidt, "Sperm-Hybrid Micromotors: On-Board Assistance for Nature's Bustling Swimmers," *Reproduction*, vol. 159, no. 2, pp. R83–R96, 2019.
- **Lukas Schwarz**, Mariana Medina-Sánchez*, and Oliver G. Schmidt, "Magnetic Micromotors for Resilient and Reversible Cargo Transport in and Between Microfluidic Environments," *2019 International Conference on Manipulation, Automation and Robotics at Small Scales (MARSS)*, pp. 169–173, 2019.
- Haifeng Xu, Mariana Medina-Sánchez*, Veronika Magdanz, **Lukas Schwarz**, Franziska Hebenstreit, and Oliver G. Schmidt, "Sperm-Hybrid Micromotor for Targeted Drug Delivery," *ACS Nano*, vol. 12, no. 1, pp. 327–337, 2018.
- **Lukas Schwarz**, Mariana Medina-Sánchez*, and Oliver G. Schmidt, "Hybrid BioMicromotors," *Applied Physics Reviews*, vol. 4, no. 3, pp. 031301(1–23), 2017.
- Mariana Medina-Sánchez*, Veronika Magdanz, **Lukas Schwarz**, Haifeng Xu, and Oliver G. Schmidt, "Spermibots: Concepts and Applications," *Biomimetic and Biohybrid Systems. Living Machines 2017. Lecture Notes in Computer Science*, pp. 579–588, 2017.
- Veronika Magdanz*, Mariana Medina-Sánchez*, **Lukas Schwarz**, Haifeng Xu, Jens Elgeti, and Oliver G. Schmidt, "Spermatozoa as Functional Components of Robotic Microswimmers," *Advanced Materials*, vol. 29, no. 24, pp. 1606301(1–18), 2017.
- Mariana Medina-Sánchez*, Maria Guix*, Stefan Harazim, **Lukas Schwarz**, and Oliver G. Schmidt, "Rapid 3D Printing of Complex Polymeric Tubular Catalytic Micromotors," *2016 International Conference on Manipulation, Automation and Robotics at Small Scales (MARSS)*, pp. 171–176, 2016.
- **Lukas Schwarz***, Mariana Medina-Sánchez, and Oliver G. Schmidt, "Easily Scalable High Speed Magnetic Micropropellers", *2016 International Conference on Manipulation, Automation and Robotics at Small Scales (MARSS)*, pp. 205–208, 2016.
- Mariana Medina-Sánchez*, **Lukas Schwarz***, Anne K. Meyer, Franziska Hebenstreit, and Oliver G. Schmidt*, "Cellular Cargo Delivery: Toward Assisted Fertilization by Sperm-Carrying Micromotors," *Nano Letters*, vol. 16, no. 1, pp. 555–561, 2016.

Curriculum Vitae

Personal Information

Surname	Schwarz
Given name	Lukas
Nationality	Deutsch
Date of birth	8 th of June 1988
Place of birth	Regensburg

Work Experience

May 2019 – Jul 2020	Private tutor for mathematics and physics at Studentenring®
May 2014 – Jul 2020	Research associate at the Leibniz Institute for Solid State and Materials Research (Dresden)
Feb – Apr 2012	Temporary employee for selling at Kaufland (Erlangen)
Sep – Dec 2011	Student associate at the Institute of Glass and Ceramics (Friedrich-Alexander University Erlangen-Nürnberg)
Aug/Sep 2010	Internship at Nabaltec (Schwandorf)
Feb/Mar 2010	Internship at emz-Hanauer (Nabburg)
Aug 2007 – May 2008	Alternative civilian service at the Dechant Wiser reformatory for children in need (Regenstauf)

Education

Oct 2011 – Jan 2014	Master of Science (Nanotechnology) at the Friedrich-Alexander University Erlangen-Nürnberg
May – Aug 2013	Research period at the Environment-Benign Materials Laboratory (Nagoya Institute of Technology, Japan)
Oct 2008 – Dec 2011	Bachelor of Science (Nanotechnology) at the Friedrich-Alexander University Erlangen-Nürnberg
Sep 1998 – Jun 2007	Allgemeine Hochschulreife (high-school diploma) at the Regental-Gymnasium Nittenau
Sep 1994 – Aug 1998	Primary education at the Volksschule Nittenau